Citation: Baran, O. (2025). In-nozzle flow and near-nozzle atomisation characterisation in optical injector nozzles. (Unpublished Doctoral thesis, City St George's, University of London)

In-nozzle flow and near-nozzle atomisation characterisation in optical injector nozzles

Onur Baran

Department of Engineering

City St George's, University of London

The dissertation is submitted for the degree of

Doctor of Philosophy

School of Science & Technology June 2025

Declaration

I hereby declare that the content of this dissertation is original and has not been submitted in whole or in part for consideration for any other degree or qualification in this, or any other university. This dissertation is my own work, except where specific reference is made to a joint effort in the text and acknowledged accordingly.

I grant powers of discretion to the University Librarian to allow the thesis to be copied in whole or in part without further reference to me. This permission covers only single copies made for study purposes, subject to normal conditions of acknowledgment.

Onur Baran

June 2025

Acknowledgements

First and foremost, I would like to express my sincere gratitude to my primary supervisor, Dr Ioannis Karathanassis, for his unwavering guidance, continuous encouragement, and for providing the infrastructure that made this research possible.

I am also deeply thankful to my second supervisor, Professor Manolis Gavaises, for his invaluable insights and for helping to shape this research in a way that has made it accessible and relevant to a wider audience.

I am grateful to the researchers at the Combustion Research Facility, Sandia National Laboratories, for their collaboration and for providing access to their experimental facilities, which have been essential to the progress of this work.

I would also like to express my appreciation to the fellows of the EDEM Marie Skłodowska-Curie Innovative Training Network for their collaboration, stimulating discussions, and friendship, all of which have greatly enriched this journey.

I am profoundly grateful to my parents, Beyhan and Orhan Baran, for their unconditional love, encouragement, and support, which have been instrumental in enabling me to pursue my academic aspirations.

Finally, I would like to express my heartfelt appreciation to my wife, Melike Aslı Baran, for her endless support, patience, and understanding throughout this journey. Her belief in me has been a constant source of strength.

Abstract

The growing demand for efficient and environmentally sustainable internal combustion engines has highlighted the vital role of fuel injectors in achieving cleaner combustion. This thesis offers a detailed analysis of in-nozzle flow, near-nozzle spray dynamics, combustion behaviour, and soot emissions across a diverse range of fuels under realistic conditions. Advanced imaging techniques, including high-speed schlieren imaging and diffuse backlight illumination (DBI), were used to visualise in-nozzle and near-nozzle flow dynamics. Combustion parameters and soot emissions were quantified using OH^* chemiluminescence and DBI extinction imaging, providing insights on phenomena such as cavitation, spray formation, and flame lift-off length, and revealing the influence of fuel properties on injection and combustion processes.

Engine Combustion Network (ECN) single-hole injectors Spray C and Spray D, along with ECN multi-hole injector Spray M, were tested under realistic conditions. Findings show that Quaternary Ammonium Salt (QAS) additives suppress geometric cavitation while enhancing longitudinal vortices in diesel fuels, thereby also increasing spray cone angles. The effect of viscoelasticity was pronounced in tapered nozzles, where vortical cavitation dominated over geometric cavitation, significantly shaping spray morphology.

Experiments with conventional diesel, Jet-A, and Sustainable Aviation Fuels (SAFs), such as Bicyclohexyl (BCH) and C-4 using Spray C and Spray D nozzles elucidated cavitation and spray characteristics under variable injection-pulse durations. BCH exhibited pronounced vortical cavitation in Spray D, leading to wider spray cone angles and improved air-fuel mixing. Combustion experiments showed QAS-treated fossil-derived diesel fuels had extended ignition delays, reduced lift-off lengths, and significant soot reduction. However, these benefits were less pronounced in bio-derived fuels due to complex interactions between molecular structure, additives, and viscoelastic micelle formation.

This research underscores the effects of injector geometry, fuel and additive properties, as well as injection timing on cavitation, spray dynamics, and combustion. It highlights the potential of viscoelastic additives to optimise spray formation and suppress emissions in fossil-derived fuels while offering crucial insights into the unique behaviour of SAFs, especially BCH, in advanced injection systems. The findings contribute to the broader development of sustainable, efficient fuel injection strategies for cleaner combustion and reduced environmental impact.

Present Contributions

The contributions of this thesis to the scientific community are the following:

- Real-size single-hole and multi-hole transparent nozzles were experimentally investigated under realistic operating conditions, providing valuable insights into injector flow behaviour. Dual-sided visualisation techniques combining high-speed diffuse backlight imaging and Schlieren imaging were employed, offering a comprehensive perspective on in-nozzle and near-nozzle flow dynamics.

- For the first time in real-size nozzles, the effects of quaternary ammonium salt (QAS) additised fuels on cavitation behaviour and spray dynamics were thoroughly examined and elucidated. The influence of varying injection pulse durations on cavitation and spray dynamics was systematically analysed and characterised using conventional diesel, jet fuel and sustainable aviation fuels (SAFs).

- Utilising diffuse back-illumination extinction imaging and OH^* chemiluminescence, the combustion characteristics and soot formation in diesel and biodiesel blends with QAS additives were evaluated. The presence of additives altered the spray topology and combustion characteristics, resulting in a measurable decrease in soot production during injection for fossil diesel fuels. However, this reduction was not observed in non-fossil non-Newtonian samples, which exhibited slightly increased emissions compared to untreated counterparts. These findings indicate that while QAS additives effectively reduce soot emissions in fossil diesel fuels, they may not exert the same impact on biodiesel blends.

Table of Contents

List of Figures

List of Tables

Nomenclature

Acronyms / Abbreviations

B10	10% biodiesel blend
BCH	Bicyclohexyl
CAD	Computer-Aided Design
CD	Discharge Coefficient
CN	Cavitation Number
CFD	Computational Fluid Dynamics
DBI	Diffuse Back-light Illumination
DBI-EI	Diffuse Back-light Illumination Extinction Imaging
ECN	Engine Combustion Network
HVO	Hydrotreated Vegetable Oil
ICE	Internal Combustion Engine
LED	Light-Emitting Diode
LEM	Light-Extinction Method
LII	Laser-Induced Incandescence
NJFCP	National Jet Fuels Combustion Program
QAS	Quaternary Ammonium Salt
PAH	Polycyclic Aromatic Hydrocarbon.
Re	Reynolds Number
RME	Rapeseed Methyl Ester biodiesel
ROI	Region of Interest
SAF	Sustainable Aviation Fuel
SCR	Selective Catalytic Reduction
VCO	Valve Covered Orifice
XPCI	X-ray Phase Contrast Imaging
ε	Eccentricity

1. Introduction

1.1. Background and Motivation

Today, the demand for transportation is on the increase [1], and more than 99% of goods and people transportation is provided by internal combustion engines (ICEs) [2]. On the other hand, conventional ICEs release greenhouse gases, leading to global warming. The severity of global warming and its impact are reaching alarming levels, necessitating immediate action [3]. Vehicle electrification aims to address these concerns, but entirely replacing ICEs is not feasible. In the foreseeable future, heavy-duty vehicles, as well as the marine and aerospace industries, will continue to rely on ICEs due to the limitations of electric battery power density. Furthermore, developing countries are expected to see increased demand for diesel engines in transportation [4]. Consequently, improving the efficiency of ICEs and minimising soot and particulate matter emissions is crucial.

Cleaner combustion technologies are essential to meet these challenges. Recently developed dual-fuel ICEs offer promising solutions for reducing emissions from heavy-duty vehicles and marine vessels. Internal combustion engines convert the chemical energy of fuels into mechanical energy. Fossil fuels are commonly used in ICEs and are stored in liquid form because of their high energy density per unit volume and ease of transportation. For efficient combustion, the fuel must be in a gaseous state, which requires effective atomisation and mixing with the oxidiser. Fuel injectors play a critical role by converting bulk liquid into fine droplets that vaporise within the combustion chamber. The quality of fuel atomisation and mixing directly impacts combustion performance and emissions; non-uniform mixing can lead to low combustion efficiency, instabilities, and increased soot formation in fuel-rich zones.

To comply with increasingly stringent regulations on particulate matter and nitrogen oxide emissions, the ICE industry and researchers are focusing on enhancing atomisation quality to improve combustion efficiency. Methods to achieve better atomisation include increasing injection pressure [5],[6], modifying fuel properties with additives, increasing operating temperatures, and optimising injector geometry. For the diesel-engine industry, the demand for improved combustion and atomisation led to the development of systems that operate at extreme pressure conditions. With the latest developments in diesel engine technology, modern fuel injectors are capable of operating at 3000 bar [7]. Increasing fuel injection pressure leads to a significant improvement in PM emissions and engine efficiency [8], prompting investigations into pressures up to 5000 bar [9]. However, increased injection pressures make the flow more susceptible to cavitation, which can cause issues such as noise and erosion in automotive, aerospace, and naval applications [10].

Methods for suppressing emissions comprise the reduction of injectors orifice diameter, implementation of low-temperature combustion [11], and use of alternative fuels [12],[13], or fuel additives [14]. Low-temperature combustion can decrease both nitrogen oxide and particulate matter emissions but faces challenges in commercial applications due to difficulties in controlling ignition timing and managing combustion rates [15]. While increasing injection pressure and reducing orifice size can lower soot emissions [16],[17],[18], these modifications exacerbate cavitation risks and increase the demand on engine energy resources, as higher injection pressures require more powerful fuel pumps, resulting in increased mechanical work and parasitic losses [19],[20].

Alternative fuels emerge as a promising solution for soot reduction, given that fuel properties significantly influence emissions. Biodiesel fuels, for instance, have demonstrated reduced soot emissions compared to conventional diesel [21],[22]. Despite ongoing efforts, current soot emission levels remain problematic. Gaining a thorough understanding of the mechanisms behind soot formation is essential for developing effective reduction strategies. Soot measurements are crucial in elucidating the formation process; however, investigating this process is challenging due to complex chemical reactions and fluctuations in temperature and soot concentration within flames. Moreover, there is a notable gap in research concerning soot levels produced by alternative fuels under realistic operating conditions. The influence of salt-based additives, incorporated mainly as detergents for fuel-delivery equipment, on combustion characteristics and soot formation has not been extensively studied. This lack of information hinders the development of effective emission mitigation strategies and underscores the need for further research to understand better the relationship between fuel types, additives, and soot formation in real-world scenarios.

1.2. Cavitation in Diesel Nozzles

Cavitation within diesel nozzles was first identified nearly a century ago and has since been the subject of extensive investigation through both experimental and numerical methods to elucidate its effects and underlying mechanisms. Despite significant advancements in the study of cavitation, a fully accurate and comprehensive model has yet to be developed. The phenomenon occurs due to a sudden change in the cross-sectional area at the nozzle inlet, causing flow contraction within the nozzle. This contraction leads to an increase in flow velocity and a corresponding decrease in static pressure. When the static pressure falls below the fluid saturated vapour pressure, a local phase transition from liquid to vapour ensues, resulting in cavitation. Cavitation has been shown to significantly influence in-nozzle flow dynamics, discharge coefficients, and spray characteristics [23],[24]. Additionally, it can contribute to the erosion of injector walls [10],[25]. Therefore, a thorough understanding of cavitation is essential for the design of high-performance and durable nozzles.

Experimental research focuses on either in-nozzle flow visualisation or near-nozzle spray atomisation. Initial studies employed transparent, enlarged nozzles to facilitate measurements and enhance cavitation-visualisation resolution [26],[27]. As material, manufacturing, and visualisation technologies advanced in subsequent years, researchers began utilising real-size injector nozzles. However, visualising cavitation is challenging, especially for modern diesel injectors, since they are operating at pressures higher than 2500 bar, and the injector-hole dimensions are of the order of micrometres. Under these working conditions, flow within the injector reaches supersonic speeds, making the temporal scale less than microseconds. Considering the velocity of the flow, dimensions of the nozzle and difficulties due to multi-phase flow, visualisation of cavitation requires state-of-the-art techniques as discussed in Section 2.3.

High-speed imaging techniques have been frequently utilised to examine the morphological features of vapour cavities that form in high-pressure diesel injectors and establish connections between these cavities and the atomisation and behaviour of the fuel spray produced by the devices [28],[29],[30]. Visualising transparent enlarged nozzle replicas has enabled the identification of different cavitation regimes. Indicative research has revealed two primary cavitation regimes within injector nozzles: sheet/cloud cavitation and vortex or string cavitation [27],[31]. Sheet/cloud cavitation occurs near solid boundaries due to local flow separation, while vortex cavitation is more likely to form in the nozzle core. The various cavitation regimes, which result from flow acceleration, separation, and coherent vortical motion [32], have been explained and linked to spray morphology [33] and erosion patterns [34].

The increased use of multi-hole injectors in diesel engines is owed to their capacity to disperse fuel spray evenly in every direction, which enhances air mixing and expands the spray surface area as a result of the merging of individual jets. Consequently, studies have also investigated cavitation within such multi-hole injectors [32],[35]. Also, tapered hole nozzles have been shown to alter the pressure distribution in the hole entry significantly, and their design is effective in preventing geometric cavitation [36],[37],[38]; however, even though geometric cavitation is prevented with the tapered hole design, string cavitation solely depends on nozzle geometry [36]. It is formed either from pre-existing geometric cavitation or from the ambient air through the nozzle hole [32]. Along with geometrical effects, studies also examined the impact of fuel characteristics on in-nozzle flow. They revealed that fuel properties play a substantial role in determining in-nozzle flow, as cavitation occurs due to variations in fuel vapour pressure [39],[40]. Moreover, the mass flow rate at the nozzle exit is influenced by disparities in both density and viscosity. Also, an increase or decrease in fuel temperature can affect the cavitating flow in nozzles due to the corresponding changes in the physical properties of the fuel. For example, an increase in temperature raises the fuel saturated pressure, making cavitation more likely to occur [41],[42].

In addition to experimental investigations, numerical studies of cavitation in diesel injector nozzles have been crucial for comprehending the phenomenon and improving nozzle performance. Researchers have utilised a range of Computational Fluid Dynamics (CFD) methods to simulate and examine cavitation in diesel nozzles. Nonetheless, modelling diesel fuel presents several challenges. One of the primary difficulties in simulating diesel nozzle flow is specifying fuel properties. The ideal fluid assumption significantly diverges from actual conditions when dealing with fluids subjected to high-pressure and high-temperature environments. Therefore, describing the fuel properties under these extreme working conditions is essential. Different Equations of State (EoS) are being used to determine fuel properties under a high pressure/temperature range. Although cubic EoSs are generally used for fuel-injection analysis, their predictive capability is limited due to the extreme temperature and density ranges realised under operating conditions [43]. Consequently, researchers are actively developing and refining new models to address these limitations [44]. For this reason, experimental research plays a crucial role in generating data to inform and validate these emerging models.

1.3. Alternative Fuels and Fuel Additives

Expanding the utilisation of renewable fuels represents a viable strategy for mitigating pollutant emissions from internal combustion engines, thereby contributing to environmental sustainability. Biodiesel, derived from a diverse array of sources, including animal fats, waste oils, and vegetable oils such as sunflower, palm, peanut, coconut, soybean, and rapeseed, emerges as a prominent renewable alternative to conventional diesel fuel. It offers several advantages over standard diesel fuel. One of its principal benefits is the higher flash point, which enhances safety during handling and storage. Additionally, biodiesel is biodegradable, reducing environmental hazards in the event of spills, and its utilisation leads to reduced exhaust emissions, thereby contributing to improved air quality [45]. Moreover, the chemical and physical properties of biodiesel closely resemble those of base diesel, allowing it to be used in existing diesel engines without the need for modifications [46]. However, despite these environmental advantages, biodiesel fuels introduce challenges related to fuel quality, which can adversely affect engine performance. One significant drawback is that the raw materials used to produce biodiesel can be expensive, and biodiesel production from vegetable oils can cause deforestation and potential food shortages [47]. Biodiesel is also prone to degradation and may not have good storage stability. Additionally, it has a lower energy density compared to fossil fuels and may not perform as well in cold temperatures. Biodiesel may also produce higher levels of NO_x emissions [48],[49].

Beyond these concerns, fuel quality remains a critical factor affecting engine performance. Poor-quality fuel can lead to the formation of deposits within the injector nozzle, resulting in injector fouling and a notable decline in engine performance over time. Modern diesel engines, which utilise smaller nozzle holes, are more susceptible to fouling. Injector-fouling issues are even more prevalent in biodiesel blends due to considerable variations in fuel quality. As a result, fuel additives have been developed to prevent deposit formation, and their application has been steadily increasing. Introducing fuel additives can alter the properties of diesel fuel, including viscosity, surface tension, and volatility. These additives are frequently used to modify fuel characteristics to achieve optimal qualities such as enhanced ignition, reduced harmful emissions, and deposit prevention. Changes in fuel properties and rheology can significantly affect the cavitation process within the injector nozzle. Therefore, understanding the impact of fuel additives on diesel nozzle cavitation is essential for improving fuel injection performance and combustion efficiency.

Modern diesel fuels are carefully formulated with a complex mixture of additives designed to enhance engine performance, ensure fuel system durability, and comply with increasingly stringent environmental and emission standards. Among the most widely used are detergents and dispersants, which inhibit the formation of harmful deposits on injectors and intake valves, thereby preserving optimal spray patterns and combustion efficiency. Cetane improvers, such as alkyl nitrates, are employed to elevate the cetane number, reducing ignition delay and facilitating smoother engine operation, particularly under cold-start conditions [50]. The reduced lubricity of ultra-low sulphur diesel is counteracted by lubricity enhancers, which minimise wear on critical components such as high-pressure pumps and injectors. Corrosion inhibitors and metal deactivators safeguard metallic fuel system parts from degradation, while antioxidants prolong storage stability by preventing oxidative breakdown. In colder climates, cold flow improvers modify wax crystal formation to maintain fuel flow at low temperatures. Additional additives, including biocides to mitigate microbial contamination and antifoam agents to prevent excessive foaming during handling, ensure reliable fuel performance across diverse operating conditions [51],[52]. Table 1.1 provides an overview of common diesel fuel additives, their specific functions, and representative compounds used in modern formulations.

Research interest in the additive investigated in this work was initiated by the observation that certain deposit-control additives containing Quaternary Ammonium Salts (QAS) could improve the volumetric efficiency of diesel fuel injectors by approximately 5%, as reported in [53]. Subsequent investigations [54],[55] have revealed that the distinguishing feature of this additive, compared to conventional deposit control additives, is the formation of elongated micelles, which can induce viscoelastic properties within the fuel composition. The research performed on the QAS-based additive is presented in more detail in Section 4.2.

Table 1.1: Common Diesel Fuel Additives, Their Functions, and Representative Compounds [51],[52],[56],[57]

Additive Type	Chemical Function	Examples
Cetane Improvers	Raise cetane number; improve ignition	Alkyl nitrates
Lubricity Enhancers	Reduce wear in low-sulphur fuel	FAMEs, esters, amides
Detergents	Clean injectors and intake valves	Polyether amines, PIB amines
Dispersants	Keep particles suspended; prevent sludge	Succinimides, phenates
Corrosion Inhibitors	Protect metal parts from corrosion	Amines, carboxylic acids
Antioxidants	Prevent oxidation; improve stability	BHT,phenolic antioxidants
Cold Flow Improvers	Enhance low-temp flow properties	Polyalkyl methacrylates
Antifoaming Agents	Reduce foam during handling	Silicone compounds, polyethers
Deposit Control Additives	Prevent injector deposits	QAS

Although biodiesel presents a promising renewable alternative for reducing emissions in internal combustion engines, particularly in ground transportation, decarbonising the aviation sector poses additional and significant challenges. The aviation industry is a major contributor to global greenhouse gas emissions, accounting for approximately 2% worldwide, primarily through carbon-dioxide outputs [58]. Projections suggest that aviation could represent up to 5% of the planet's total greenhouse gas emissions by 2050 [59]. In recent years, stringent environmental regulations have underscored the imperative need for a sustainable transition within the transportation sector, emphasising the adoption of cleaner energy alternatives. This transition is particularly critical in aviation due to strict safety protocols and weight limitations that complicate the adoption of alternative energy sources [60]. While innovative technologies such as electric or hydrogen-powered aircraft hold promise, they are not yet viable for long-distance flights in the immediate or medium-term future [61],[62]. Consequently, the industry continues to rely on liquid fuels but is increasingly turning to carbon-neutral options known as Sustainable Aviation Fuels (SAFs) to mitigate environmental impact [63]. Significant research efforts are being channelled towards exploring renewable resources for producing these fuels [64],[65].

Previous research on fuel cavitation and spray dynamics has predominantly focused on diesel fuel and its alternatives. However, a significant research gap exists in the study of cavitation and spray dynamics specific to aviation fuels. Addressing this gap, the present research explores a diverse range of fuels, including diesel, dodecane, Jet-A, C-4 fuel (a blend of iso-paraffins, dodecane, and hexadecane), and an innovative bio-derived cycloalkane fuel, BCH. By investigating these diverse fuels, this research aims to bridge the knowledge gap in cavitation and spray dynamics specific to aviation fuels, potentially leading to more efficient and effective fuel alternatives for the aviation industry.

Dodecane, widely used as a primary surrogate for diesel fuel, provides a sufficiently accurate approximation and is also utilised as a surrogate for jet fuel [66],[67], especially Jet-A, due to its significant presence by weight [68]. Another high-density hydrocarbon compound present in Jet-A is BCH [69]. BCH can be sustainably produced from renewable biomass through advanced biorefinery methods, such as catalytic pyrolysis and hydrodeoxygenation, which enable the conversion of lignocellulosic biomass into BCH [70],[71]. BCH is particularly promising as an alternative to conventional jet fuels owing to its high energy density and superior heat capacity [72]. Jet-A, one of the fuels investigated, is a widely utilised type of jet fuel comprising a complex blend of hydrocarbons [73]. A Jet-A variant, JP-8, is enhanced with additives for anti-icing and lubrication purposes [69] and is employed in both diesel and aero-prop engines. Notably, both Jet-A and another fuel, C-4, are included in the National Jet Fuels

Combustion Programme (NJFCP), an initiative led by a consortium of U.S. federal agencies with international collaboration. The primary objective of the NJFCP is the development of universal methodologies for testing and modelling fuel combustion processes, aiming to elucidate the intricate interactions between fuel chemistry and physical properties during combustion. This endeavour facilitates the expedited validation of novel alternative jet fuels [74]. C-4 is a test fuel created as part of this programme, characterised by typical boiling characteristics and a low cetane number (28). A recent study [75] indicates that C-4 and BCH fuels produce significantly less soot than Jet-A, owing to enhanced diffusive mixing under high-pressure conditions. Experiments simulating cruise and take-off scenarios in a constant-volume combustion vessel utilised high-speed microscopy and machine-learning algorithms to analyse the evaporation behaviours of injected spray droplets. The transition from classical to diffusive evaporation during take-off resulted in reduced soot formation and diminished soot mass compared to Jet-A, underscoring the potential advantage of utilising sustainable aviation fuels in reducing particulate matter emissions.

Despite significant advancements in combustion efficiency and emission reduction, mitigating cavitation effects remains a challenge, often leading to injector damage and a reduced component lifespan. Accordingly, this study benchmarks cavitation and spray dynamics of diesel, dodecane, Jet-A, C-4 and BCH under identical high-pressure injections, furnishing data to refine fuel systems and combustion models for cleaner, longer-lasting engines.

1.4. Objectives

Fuel injectors have been fundamental to internal combustion engines for decades, yet evolving operating conditions have made the injection process increasingly complex. The dual requirement of enhancing engine efficiency and reducing harmful emissions, such as soot and particulate matter, are driven by rising energy demands and stricter environmental regulations. Despite advancements in electrification, internal combustion engines remain indispensable for heavy-duty transportation and aviation due to the current limitations of battery technology. While enhancing fuel atomisation through higher injection pressures and optimised injector designs can improve combustion efficiency, it also increases the risk of cavitation formation, which can damage injectors and compromise performance.

Fuel additives have long been utilised to enhance fuel performance, reduce injector fouling, and mitigate wear within fuel injection systems. Among these, Quaternary ammonium salt additives have shown particular promise for improving injector cleanliness and fuel flow by altering fuel rheology. However, their impact on flow phenomena within the injector, including cavitation and vortex formation, has yet to be fully understood under realistic operating conditions.

Alternative fuels, such as biodiesel, offer significant environmental advantages; however, their widespread adoption presents challenges such as inconsistent quality, limited storage stability, and the potential for increased nitrogen oxide emissions. Sustainable aviation fuels such as BCH and C-4 also show potential for reducing soot emissions. Nonetheless, their behaviour under diesel-relevant injection conditions, particularly in terms of cavitation and spray dynamics, requires further investigation. Although a variety of models exist for simulating spray formation and soot production, many rely on simplified assumptions that limit their predictive accuracy under real engine conditions. Most do not account for the complex interaction between viscoelastic fuel behaviour, in-nozzle cavitation and turbulence. These limitations hinder the accurate prediction of combustion and emission trends. Experimental research is therefore essential to investigate injector flow and resultant soot emissions, providing critical data to refine computational models. Internal nozzle flow directly affects spray dynamics and atomisation, which are crucial for achieving efficient combustion, improved engine performance, and reduced emissions. A detailed understanding of the relationship between cavitation and spray behaviour is thus critical for improving injector performance.

This research addresses these knowledge gaps through a comprehensive experimental investigation that visualises cavitation and spray dynamics within real-size transparent nozzles under engine-relevant conditions, for a wide range of conventional and renewable fuels, as well as their QAS-additised counterparts. The study seeks to elucidate the relationships between in-nozzle cavitation, spray dynamics, and the influence of fuel properties and QAS-based additives on both cavitation and spray behaviour. Additionally, it investigates the effects of alternative fuels and QAS additives on soot formation, providing critical insights into the mechanisms underlying soot generation. This work aims to develop effective strategies to reduce emissions in practical applications. Ultimately, this research contributes to a deeper understanding of the complex interactions between fuel types, additives, cavitation, spray dynamics, combustion characteristics, and soot formation. It aspires to advance cleaner and more efficient combustion technologies, as well as durable fuel injection systems for the transportation and aviation sectors.

To achieve these objectives, the study employs advanced diagnostic techniques. Real-size transparent nozzles, standardised by the Engine Combustion Network, are used to visualise nozzle flow using high-speed schlieren imaging and diffuse backlight illumination. Combustion characteristics and soot formation are examined under realistic ambient pressures and temperatures using OH^* chemiluminescence and the DBI extinction imaging. Taken together, these techniques trace the coupled evolution of cavitation and spray dynamics across diesel, biodiesel, their QAS-additised counterparts and a range of SAF fuels, while simultaneously capturing soot formation; by integrating these observations within a single experimental framework the study clarifies the links between fuel properties, in-nozzle flow, near-nozzle spray and soot formation, thereby guiding injector design and fuel-formulation strategies aimed at cleaner, more efficient combustion.

1.5. Thesis Outline

This thesis employs high-speed schlieren and diffuse back-illumination imaging to visualise cavitation inside ECN Spray C, D and M transparent nozzles and the accompanying near-nozzle spray geometry, and quantifies how quaternary ammonium salt additives modify fuel rheology, cavitation and spray dynamics. It also measures ignition delay, flame lift-off length and time-resolved soot mass using synchronised OH* chemiluminescence and DBI extinction under engine-relevant pressures and temperatures, and explores how a range of injection pulse durations reshapes cavitation and spray dispersion in fossil diesel, Jet-A and the sustainable aviation fuels bicyclohexyl and C-4. Collectively, these tasks clarify the links between internal-nozzle flow, spray dynamics and soot formation, guiding the design of cleaner and more efficient combustion systems. Structured into six chapters, the thesis provides a comprehensive understanding of these topics.

Chapter 1 introduces the background and motivation for the research. It discusses the complexities introduced by recent changes in fuel injector operating conditions and highlights the limitations of current models in accurately predicting spray behaviour and soot emissions. The chapter explores the phenomenon of cavitation in diesel nozzles, examines alternative fuels and fuel additives, and outlines the primary objectives of the study.

In Chapter 2, a thorough review of existing literature is presented. This chapter covers cavitation in nozzle flow and near-nozzle spray, examining previous experimental. It delves into alternative fuels and fuel additives, discussing their potential impact on engine performance and emissions. The chapter also reviews soot formation mechanisms and measurement techniques, concluding with an overview of cavitation visualisation and spray measurement methods.

Chapter 3 details the experimental setup and methodologies employed in the research. It describes the pressure chamber and fuel injection system used to simulate realistic engine conditions and outlines the in-nozzle and near-spray visualisation setups, including the use of real-size transparent nozzles standardised by the Engine Combustion Network (ECN). Advanced imaging techniques such as high-speed Schlieren imaging and Diffuse Backlight Illumination (DBI) are discussed. The chapter also explains the image processing methods and combustion measurement techniques, including OH^* chemiluminescence and soot quantification using the DBI extinction method.

The findings of the research are presented in Chapter 4, divided into three main sections corresponding to the phases of the study. The first section investigates the effects of QAS additives on cavitation and spray dynamics using single-hole injectors (ECN Spray C and Spray D) and a multi-hole injector (ECN Spray M). The results show how QAS additives suppress geometric cavitation while enhancing longitudinal vortices, leading to changes in spray cone angles. The effects of viscoelasticity on turbulence-induced instabilities and the implications for particulate emissions are also discussed in detail.

The second section extends the investigation to Sustainable Aviation Fuels (SAFs), comparing diesel, dodecane, conventional Jet-A fuel, and SAFs such as C-4 and bicyclohexyl. Employing ECN Spray C and Spray D nozzles, the study examines cavitation and spray dynamics under varying injection pulse durations. Distinct behaviours, such as the pronounced vortical cavitation observed in BCH due to its viscosity, are analysed, highlighting the role of injector geometry and injection timing in determining cavitation intensity and spray morphology.

The final section explores the impact of fuel composition and QAS additives on combustion characteristics and soot emissions. A range of diesel fuels is investigated, including fossil-derived diesel, Rapeseed Methyl Ester (RME) biodiesel, a 90% reference/10% biodiesel blend (B10), and Hydrotreated Vegetable Oil (HVO). Using high-speed DBI extinction imaging and OH^* chemiluminescence imaging, the study evaluates ignition delay, flame lift-off length, and soot mass under high-pressure and high-temperature conditions that simulate real-world engine environments. The findings offer valuable insights into how QAS additives affect combustion dynamics and reduce soot emissions.

Chapter 5 summarises the key findings of the research, highlighting the contributions made to the understanding of cavitation, spray dynamics, and soot formation. It discusses the implications of the results for future fuel design and injection technologies, emphasising the potential for reducing emissions and improving engine performance in both automotive and aviation sectors.

Through these chapters, the thesis delivers a comprehensive exploration of how fuel composition and additives influence cavitation phenomena, spray dynamics, and combustion. By employing advanced imaging techniques and examining a diverse range of fuels, including conventional diesel, biodiesel, and sustainable aviation fuels, the research provides significant insights into fuel behaviour under high-pressure injection conditions. The findings are expected to inform future advancements in fuel design and injection technologies, ultimately contributing to efforts to reduce emissions and enhance engine performance across various sectors.

2. Literature Review

2.1. Introduction

Cavitation is a complex and critical phenomenon occurring within diesel injector nozzles, substantially influencing nozzle flow characteristics and the subsequent near-nozzle spray dynamics. It plays a pivotal role in engine performance and emissions, affecting both the durability of injector components due to erosion and the efficiency of combustion processes through its impact on spray formation and atomisation. Over the years, a considerable body of research has focused on understanding the mechanisms of cavitation inception and development within injector nozzles, utilising experimental studies, CFD simulations, and theoretical analyses.

The geometry of injector nozzles, along with needle motion and shape, are key factors affecting cavitation behaviour and the resulting spray characteristics. Variations in these parameters can alter cavitation patterns, which in turn influence spray cone angles and atomisation processes. A deeper understanding of these influences is essential for optimising combustion efficiency and reducing pollutant emissions. In parallel, there is an increasing emphasis on the use of alternative fuels and fuel additives to enhance engine performance and mitigate environmental impacts. Biodiesel, as a renewable fuel, offers significant environmental benefits but presents challenges such as increased injector deposits and altered cavitation behaviour due to its physical properties. Furthermore, the single fuel policy mandates the use of aviation fuels like JP-8 across military equipment, prompting research into the use of aviation fuels in diesel injector systems [76],[77]. Sustainable aviation fuels, including Jet-A and alternative fuels such as C-4 and BCH, have been investigated for their cavitation and spray characteristics, highlighting gaps in current knowledge and the need for further research in this area.

An emerging area of interest relates to the influence of fuel viscoelasticity on cavitation and spray formation. Viscoelasticity, which describes the ability of the fluid to exhibit both viscous and elastic characteristics under deformation, has been shown to affect the dynamics of liquid breakup and nozzle flow. Recent experimental and numerical studies have demonstrated that viscoelastic fuel additives can suppress undesirable cavitation regimes and influence spray morphology by modifying turbulence characteristics within the injector nozzle [55],[78]. In particular, Naseri [55] applied a CFD approach to quantify the effect of detergent-based viscoelastic additives on vortical and cloud cavitation, showing potential benefits in mitigating erosion-prone vapour structures while enhancing spray cone angles. Further molecular-dynamics based studies at atomistic scales and mesoscale have established that polymeric and nanostructured additives impart viscoelastic behaviour to fuel-like fluids, altering rheological properties such as shear-thinning and relaxation times, which could directly influence cavitation development in high-pressure injection systems [79],[80]. Despite these promising findings, the complex interplay between viscoelasticity, turbulence, and cavitation in realistic diesel injector geometries remains insufficiently understood, highlighting the need for further targeted research in this domain.

Soot emissions from diesel combustion pose significant health and environmental risks. Cavitation strongly influences spray atomisation and air–fuel mixing, indirectly affecting soot formation. Improved atomisation enhances mixing, promoting more complete combustion and reducing soot production. Therefore, understanding cavitation is essential not only for characterising internal nozzle flow but also for evaluating emissions. Advanced diagnostic techniques, such as diffuse back-illumination extinction imaging, have been used to quantify soot distribution in diesel sprays, offering insight into the interaction between nozzle dynamics and combustion. These investigations link internal flow to combustion, emphasising the need to control cavitation for cleaner, more efficient engine operation.

Advancements in visualisation techniques, including DBI, schlieren imaging, and X-ray imaging, have significantly contributed to the understanding of cavitation phenomena within diesel injector nozzles. Similarly, the characterisation of spray properties is crucial for improving combustion efficiency, necessitating the use of sophisticated measurement techniques to capture the complex dynamics of fuel injection and atomisation processes.

This literature review aims to provide a comprehensive overview of the current knowledge on cavitation in nozzle flow and near-nozzle spray, focusing on both conventional and alternative fuels. It examines the effects of fuel additives on cavitation phenomena and explores how these additives can be leveraged to improve combustion characteristics. By examining the latest research, experimental findings, and computational approaches, this review identifies the factors influencing cavitation and its consequences on fuel injection processes, while also highlighting potential areas for further investigation and improvement.

2.2. Soot Formation and Measurement

Incomplete combustion of hydrocarbon fuels leads to soot formation in internal combustion engines. The formed soot has detrimental effects on both health [81], and the environment [82].

Despite considerable research efforts aimed at understanding soot formation and oxidation, the intricate nature of the underlying chemical processes continues to hinder a comprehensive understanding of these phenomena. Even with persistent attempts to reduce emissions, current soot-emission rates are still considered unacceptable under Euro VII regulations [83]. To effectively reduce these emissions, it is crucial to have a comprehensive understanding of the mechanism responsible for soot formation. Soot measurement is a vital tool to elucidate the formation mechanism. Particularly, quantitative soot measurement is needed to investigate soot formation and to validate soot models for CFD simulations for the development of strategies to reduce pollutant emissions. However, the process remains challenging to investigate due to the complex nature of chemical reactions and the variations in temperature and soot fraction in flames.

Various methods have been demonstrated to reduce soot emissions. Higher injection pressure and smaller nozzle diameter have been proven to be effective in reducing soot formation [84],[85]. However, other factors such as manufacturing precision, cavitation and the cost associated with increasing the operating pressure limit this option at a certain level. Another viable option for reducing soot emissions is to increase biodiesel use. Biodiesel and its mixes have been shown to be an alternative to standard diesel for reducing soot [22],[86]. The type of fuel used in combustion plays a significant role in soot emissions generation, and relevant effects have been studied extensively. Surrogate fuels, which replicate essential properties and combustion characteristics of the actual blends, allow researchers to investigate soot formation mechanisms under controlled conditions. This approach contributes to developing and validating numerical models, thereby improving our practical understanding of soot formation. Consequently, a considerable percentage of research investigations focusing on soot formation utilise surrogate fuels to reduce uncertainties, given the complexity of real-world fuels.

In their comprehensive review, Mohankumar and Senthilkumar [87] provide a foundational analysis of the physical and chemical processes involved in soot generation, including pyrolysis, nucleation, surface growth, coalescence, and oxidation. Their work underscores the importance of temperature, pressure, and oxygen concentration in soot formation and highlights the significant role of fuel structure and composition. They confirm that high carbon-to-hydrogen ratios and high aromatic content encourage soot formation, whereas oxygenated fuels such as biodiesel suppress it by enhancing oxidation inside the cylinder. The general principles governing soot nucleation, surface growth, and oxidation have been well-established in the foundational review by Mansurov [88], who examined both the phenomenology and kinetics of soot formation in hydrocarbon combustion systems. His work outlining key mechanisms including Polycyclic Aromatic Hydrocarbons (PAH) condensation, acetylene reactions, and soot aggregation under a wide range of flame and engine conditions.

Omidvarborna et al. [89] provided an extensive review of soot formation mechanisms and modelling strategies for both diesel and biodiesel fuels. They highlighted that acetylene and PAHs are key precursors in diesel soot formation, while biodiesel combustion typically results in reduced PAH formation due to its oxygenated nature. The authors categorised soot models into empirical, semi-empirical, detailed, and phenomenological approaches, emphasising that phenomenological models, although simplified, are especially promising for capturing key trends under varying combustion conditions. Their work also stressed that in biodiesel modelling, oxidation reactions involving oxygen radicals must be explicitly considered, and surrogate molecules such as methyl butanoate and methyl decanoate are often used to emulate biodiesel behaviour in computational studies.

Payri et al. [90] aimed to enhance the understanding of combustion processes in direct injection diesel engines by examining a two-component diesel surrogate, composed of dodecane and m-xylene, in a constant volume spray combustion vessel under realistic working conditions. Using a single-hole ECN injector, Spray A, the researchers conducted experiments and numerical simulations to assess ignition delay and lift-off length across various ambient temperatures, densities, and fuel injection pressures. The study demonstrated the surrogate fuel response to these parameters and evaluated the performance of a reduced chemical kinetic mechanism and interactive flamelet turbulent combustion model. Results indicated that while the simulations captured experimental trends well for different conditions, there remains room for improvement, particularly at lower ambient temperatures and densities. Wang et al. [91] performed a numerical study with a soot model to understand soot formation in a diesel engine fuelled with diesel and different biodiesel blends. The results of the simulations indicated that biodiesel produces less soot than diesel fuel. This reduction in soot is due to the oxygen content of the fuel, which reduces soot formation and enhances soot oxidation. Furthermore, the results showed that a lower proportion of unsaturated FAME in biodiesel fuels led to mitigated soot production. It is commonly acknowledged that higher oxygen composition in the fuel has a positive effect on limiting the formation of soot precursors in areas with rich fuel, resulting in decreased soot production [85].

Fuel additives have been extensively studied as a potential solution to mitigate soot formation. Musculus et al. [92] investigated the potential of fuel additives to reduce in-cylinder soot formation in diesel engines. The study identified several additives, including ethanol, ethylene glycol dimethyl ether, and a nitro-compound mixture, that could alter combustion chemistry to reduce soot formation. The study measured in-cylinder soot and diffusion flame lift-off in a direct-injection diesel engine using various blends of commercial diesel fuel with different combinations of additives. The results showed that only the ethanol-containing fuels had the potential to reduce in-cylinder soot, with a reduction of up to 15% in jet soot and more than 30% in wall soot. The other additives affected in-cylinder soot, but changes could be attributed solely to differences in ignition delay. The study concluded that non-ethanol additives have little potential for reducing in-cylinder soot formation, or their concentrations were too small to have a significant effect.

Mueller and colleagues [93] investigated the characteristics of soot formation and its precursors in direct-injection diesel engines using experimental and numerical approaches. The study introduced the oxygen ratio parameter to assess reactant-mixture stoichiometry for oxygenated fuels accurately. The findings demonstrated that some oxygenates are more effective at reducing diesel soot than others, and the research delved into how the structure of oxygenates and in-cylinder processes impact soot formation. The study revealed that tri-propylene glycol methyl ether is more effective at decreasing soot than di-butyl maleate. Fuel oxygenation can be more efficient than improving oxygen entrainment. Combining fuel oxygenation with enhanced oxygen entrainment could lead to soot-free combustion. However, the research also points out challenges from multiple-jet and jet-wall interactions in engines. These interactions can result in regions that are susceptible to soot formation even when aiming for soot-free conditions.

The pioneering research by Siebers and Higgins [94] examined how ambient gas temperature, density, injection pressure, and orifice diameter impact the flame lift-off length in diesel sprays. They found that an increase in ambient gas temperature or density leads to a decrease in lift-off length, while an increase in injection pressure or orifice diameter results in a longer lift-off length. The study also discovered a strong connection between soot formation and fuel-air mixing before the lift-off length, with soot incandescence reducing as air-fuel premixing intensifies. Pickett et al. [95] explored the impact of ignition processes on diesel lift-off stabilisation using OH^* chemiluminescence imaging. Their findings revealed that fuel ignition quality plays a role in lift-off, with fuels exhibiting shorter ignition delays resulting in reduced lift-off lengths.

In addition to experimental investigations, numerical studies play an essential role in understanding soot formation and oxidation in internal combustion engines. CFD simulations incorporating detailed or reduced chemical kinetics enable controlled investigation of in-cylinder processes and their sensitivity to fuel composition, pressure, temperature, and flow. Validated models also support emission prediction and the development of cleaner combustion strategies. Recent CFD research has increasingly employed surrogate fuels and advanced soot sub-models to study soot evolution in both light-duty and marine diesel engines.

Hong et al. [96] developed a comprehensive soot model integrating soot nucleation, surface growth, agglomeration, oxidation, and transport, calibrated against high-pressure shock tube data and diesel engine experiments. Their simulations, using n-heptane as a surrogate fuel, accurately predicted trends in soot mass for pressures ranging from 20 to 80 MPa and temperatures between 1550–2050 K, showing good agreement with experimental measurements across different injection timings and exhaust gas recirculation levels.

Pang et al. [97] extended soot modelling to marine diesel engine conditions, using a revised multi-step soot model and a newly developed n-heptane mechanism. Their simulations captured the influence of ambient pressure on soot volume fractions and highlighted the impact of soot radiation on in-cylinder heat transfer and NO formation. Notably, soot radiation increased total heat loss to walls by 30%, while only marginally affecting net soot mass production, suggesting that radiation must be accounted for in thermal models even when soot mass predictions remain relatively insensitive.

Cheng et al. [98] proposed an improved detailed soot model based on PAH chemistry, capturing particle nucleation, growth, oxidation, and PAH deposition. The model used a reduced chemical mechanism for a n-heptane/toluene surrogate and was validated against experimental data from optical and single-cylinder diesel engines. It predicted not only soot mass concentration but also particle number and size distribution, revealing that soot particle sizes ranged from 5–40 nm at the start of combustion and evolved to 5–20 nm during oxidation-dominated phases. Taken together, these findings highlight the importance of integrating detailed chemical kinetics with transport processes and radiative heat-transfer effects within CFD calculations.

To effectively reduce emissions, it is crucial to have a comprehensive understanding of the mechanisms responsible for soot formation. However, the complex nature of the chemical reactions involved has made it challenging to fully comprehend the soot formation process. Variations in temperature and soot fractions in flames add further complexity, making the investigation even more difficult. As such, appropriate measurement techniques are essential for elucidating the soot formation mechanisms. Over the years, both invasive and non-invasive techniques have been employed to study soot formation. Invasive techniques affect the combustion process since they require direct contact with the flame. With advancements in optical systems, non-invasive optical methods are now commonly utilised as they do not interfere with combustion. Today, methods such as the Light-Extinction Method (LEM), two-colour pyrometry, and laser-induced incandescence are commonly used for soot measurements [99]. Despite being straightforward and relatively inexpensive, these techniques can be limited by beam steering effects, which can compromise imaging fidelity. This issue is particularly problematic under high-pressure, high-temperature conditions typical of real-world combustion applications, where it becomes difficult to distinguish between light loss caused by refractive index gradients and attenuation due to absorption and scattering [100].

Line-of-sight extinction measurements quantify the amount of light absorbed or scattered by particles along a given path. Although these measurements are often straightforward and cost-effective, they can be influenced by refractive index gradients, making it difficult to distinguish whether light loss arises from absorption and scattering or from refractive index variations. To address these challenges, Diffuse Back-illumination Extinction Imaging (DBI-EI) has been developed as a light extinction technique that quantifies soot according to Beer's Law. In DBI-EI, a diffuser and lens are used to create a quasi-Lambertian light distribution, helping to mitigate beam-steering effects. This technique provides instantaneous two-dimensional soot distribution data, offering valuable insights into soot formation. DBI-EI is capable of measuring higher optical thickness values than planar laser-induced incandescence and is more accurate than the two-colour method. Consequently, DBI-EI was employed to overcome the limitations of traditional methods for soot measurement. Details of the measurement techniques can be found in the Methodology section.

2.3. Cavitation Visualisation

Advancements in visualisation techniques, such as shadowgraphy, schlieren imaging, and X-ray imaging, have significantly improved the understanding of cavitation phenomena within diesel injector nozzles. Blessing et al. [38] employed high-speed diffuse light imaging and numerical analysis to investigate the impact of nozzle configuration on internal flow and spray propagation in fuel injection nozzles. It was demonstrated that a more uniform flow with diminished cavitation could be achieved by rounding the inlet edges and utilising a positively conical spray hole form. These modifications prevented spray formation from being influenced by cavitation bubble collapse, reducing the spray cone angle. Additionally, the study highlighted differences in internal nozzle flow due to various needle control mechanisms, with highly transient flow phenomena resulting from fast needle response times, leading to the formation of vortical structures and string cavitation.

Balz et al. [101] visualised the in-nozzle flow of transparent single-hole marine-diesel injectors under realistic operating conditions using back-lit shadowgraphy: a 640 nm laser beam was first collimated and then diffused to create a spatially uniform background, so cavitation structures cast sharp shadows onto the high-speed camera. The study demonstrated that the nozzle bore location and geometric features significantly influence the formation of cavitation. Badock et al. [102] investigated cavitation in actual-size diesel injection nozzles and the breakup dynamics at the spray hole exit using laser light sheet and shadowgraph methods. Experiments were carried out with a diesel-like test oil in a high-pressure chamber. They observed thin cavitation films that did not interfere with the internal nozzle flow, and no bubble coalescence was detected even at elevated injection pressures. The study concluded that, under these conditions, the nozzle flow maintained a coherent liquid core at the exit.

Complementary optical diagnostics have been paired to deepen insight into cavitation behaviour. Karathanassis et al. [103]; synchronised DBI with micro-schlieren imaging resolves attached cavity sheets and the attendant vortical field in optical single-hole injectors operating at 700–900 bar. Tekawade et al. [104] employed time-resolved synchrotron X-ray phase-contrast tomography, coupled with high-speed radiography, to obtain three-dimensional maps of vapour–liquid interfaces inside production-steel nozzles at frame rates approaching 2 kHz; meanwhile, Guénot et al. [105] permits concurrent quantification of liquid-mass and scalar concentration in the emerging spray. Together, these integrated set-ups capture cavity sheets, density gradients and liquid-mass distribution simultaneously, forging a clearer link between highly transient in-nozzle two-phase flow and the ensuing spray asymmetry.

In recent years, X-ray technology has gained popularity for studying cavitation in injectors, offering significant advantages over traditional visualisation methods. X-ray measurements are unaffected by optical density, do not require visual access, and provide both quantitative and qualitative data [106], enabling researchers to study unmodified real injectors. Karathanassis et al. [54] pioneered the use of synchrotron X-rays to detect vortical cavitation in carbon-fibre composite material enlarged nozzles. X-ray micro-computed tomography has proven effective in quantifying cavitation volume fraction within nozzles [107]. Mitroglou et al. [108] employed time-averaged X-ray micro-computed tomography alongside high-speed visualisation to examine cavitation in an enlarged single-hole nozzle. Karathanassis et al. [78] utilised X-ray imaging to quantify cavitation in transient flow injectors, combining X-ray absorption and phase-contrast imaging to accurately study dynamic cavitation features and measure vapour content. This approach leveraged the strengths of both techniques, with absorption imaging providing vapour quantity data and phase-contrast imaging offering information on cavitation structure morphology.

2.4. Spray Measurements

Storing fuel in liquid form provides advantages in terms of volumetric efficiency and safety; however, to achieve efficient combustion, the fuel must be converted into a gaseous state. Fuel injectors play a crucial role in this process by atomising the bulk liquid fuel into fine droplets, thereby promoting thorough mixing of fuel and air within the combustion chamber. This mixing process is essential for efficient combustion, as uneven mixing can lead to increased fuel consumption and elevated emission rates. Given the critical importance of atomisation in combustion efficiency, understanding this phenomenon is crucial. Atomisation, the transformation of bulk liquid into a spray of fine particles, is a complex phenomenon predominantly influenced by fuel properties, injector geometry, and ambient conditions. This complexity is further heightened in diesel injectors due to the temporal scales of milliseconds in injection durations and spatial scales on the order of 10^{-4} metres in injector dimensions. Moreover, multi-phase flow phenomena such as cavitation add additional challenges to the investigation of spray characteristics.

The spray topology is influenced by internal flow, so spray characterisation should be simultaneous with internal flow visualisation. Also, it has been established in the literature that cavitation enhances atomisation [109]. Measuring spray properties for modern diesel operating conditions is a challenging task, demanding the application of state-of-the-art techniques. Moreover, spray characterisation cannot be accomplished with a single technique alone; a combination of measurement techniques is required to obtain comprehensive properties of the spray. Visualisation techniques such as Schlieren, Mie-scattering, and diffuse backlight illumination can provide macroscopic properties of the spray. Furthermore, the high injection pressure through small nozzles causes liquid velocity to reach hundreds of metres per second, necessitating high-speed visualisation. Additionally, transient flow features cause perturbations in the spray and fluctuations in the spray cone angle. The spray cone angle controls the spatial distribution of the spray and significantly influences combustion efficiency. Hence, extensive research has been conducted on the experimental characterisation of spray cone angles [110], [111],[112].

Various optical techniques have been used to evaluate the spray cone angle of high-pressure diesel sprays, including Schlieren, shadowgraphy, diffuse backlight illumination, Mie scattering, and X-ray imaging techniques [113],[114],[115]. Shadowgraphy is a commonly used technique for spray cone angle measurement due to its simplicity and low cost. It relies on the differences in refractive index between the liquid and gas phases, which cause light rays to bend and generate shadows on a screen or detector. However, this technique suffers from low sensitivity and cannot distinguish between liquid and vapour regions. Douwel et al. [116] used high-speed shadowgraphy to quantify the spray cone angle of diesel fuel injection through a realistic heavy-duty multi-hole common rail injector at engine-like conditions. Similarly, Tang et al. [117] employed high-speed shadowgraphy to examine the spray cone angle and spray penetration under diverse ambient conditions for diesel fuels over a broad scope of diesel-engine operating situations, encompassing transient and quasi-steady-state processes. They assessed the spray cone angle and penetration using a single-hole heavy-duty injector in an optical constant volume chamber. Observing three stages in the spray cone angle, they utilised these insights to establish correlations for transient processes in spray CFD simulations. The resulting model displayed strong alignment with experimental data, enhancing the predictive accuracy in CFD studies.

Safiullah et al. [118] characterised diesel single-hole sprays with the classical diffuse back-light illumination set-up: a white LED, passed through a ground-glass diffuser, produced a spatially uniform background that a high-speed video camera recorded at 20 000 fps using a 5 ms exposure. Experiments conducted in a nitrogen-charged constant-volume vessel quantified cone angles and examined the influence of nozzle diameter and injection pressure on spray development. Although the DBI arrangement delivers sharply defined silhouettes for cone-angle measurement, its millisecond-scale exposure and fully diffused illumination obscure the early stages of primary break-up and limit temporal resolution. The study demonstrated that smaller nozzles produced wider cone angles, thereby enhancing atomisation. The experimental results indicated that smaller nozzle sizes led to larger spray angles and improved atomisation.

Riess et al. [119] employed schlieren imaging and Raman spectroscopy to examine air entrainment and mixture distribution in sprays under practical diesel engine operating conditions. They aimed to assess the effects of injection pressure and various fuels on mixture formation. Spray cone angles were determined from schlieren images, while Raman spectroscopy was used to explore the local mixture distribution for different fuels. The findings revealed that the specific physical properties of the fuels did not significantly influence the local mass ratios of fuel sprays.

Diesel sprays are optically dense; their optical depth can be greater than 10 [120]. Optical depth, a measure of the transparency of a medium, depends on droplet size and density and provides an approximation of the average number of scattering events occurring during the passage of light. Optical depth varies significantly based on injection pressure, fuel types, and working conditions. These challenging conditions have prompted researchers to explore new visualisation techniques. Ballistic imaging, an improved schlieren technique, was developed to overcome the challenges of obscuration caused by multiple light scattering events. It enables the visualisation of objects in a measurement volume by reducing the impact of scattered light on their visibility and is particularly useful for sprays with an optical depth larger than 5 [121]. During the past decade researchers have also embraced X-ray diagnostics to interrogate spray regions that remain opaque to visible light. Synchrotron and high-flux laboratory sources enable X-ray radiography, phase-contrast imaging and tomography to penetrate metal injector walls as well as centimetre-thick liquid columns, thereby sidestepping the multiple-scattering limitation of optical methods. Karathanassis et al. [54] used X-ray phase-contrast imaging to capture the transition between string and cloud cavitation inside an axisymmetric orifice and showed that viscoelastic fuel additives can suppress turbulence as well as vapour formation. More recently, Tekawade et al. [104] reconstructed time-resolved, three-dimensional tomograms of two-phase flow inside a 200 µm steel diesel nozzle, directly linking micron-scale inlet irregularities to transient vapour-layer development at engine-relevant injection pressures. Bauer et al. [122] employed ultrafast X-ray computed tomography (up to 1000 slices s^{-1}) to reconstruct three-dimensional void-fraction fields in a strongly cavitating 20 mm channel, revealing ring cavitation, elongated vapour pockets and rapid explosion events where growing vapour cores force bubbly liquid radially outward. Bothell et al. [115] employed high-speed white-beam X-ray imaging at up to 100 kHz to resolve primary break-up in an air-blast atomiser, revealing a wide range of transient liquid structures and entrained air bubbles in the dense near-field region, phenomena that remain invisible to conventional back-lit imaging.

Collectively, these studies establish X-ray radiography, phase-contrast imaging and tomography as mature, complementary tools for characterising both internal-nozzle cavitation and dense external sprays.

3. Methodology

3.1. Introduction

To visualise and quantify flow within and near the nozzle, real-size transparent injector tips, fabricated from acrylic material, were designed to replace the original metal injector tips. These acrylic tips were securely clamped to the metal injector bodies and used for both single-hole and multi-hole nozzles. The injector geometries selected for this research were sourced from the Engine Combustion Network (ECN), an international consortium of research institutions and industry partners dedicated to advancing the understanding of spray combustion in direct-injection internal combustion engines. The ECN conducts experiments with standardised injectors across multiple facilities, enabling robust comparative analysis of the resulting data. In this study, the ECN single-hole injectors Spray C and Spray D, as well as the multi-hole injector Spray M, were utilised.

The fuels investigated included a non-Newtonian diesel fuel sample treated with QAS additives, exhibiting viscoelastic effects, along with biodiesel (FAME); both were compared against conventional diesel fuel for the first time. It should be noted that QAS agents, even at parts-per-million concentrations, do not alter the bulk thermodynamic or transport properties of the fuel mixture, yet modify its rheological behaviour. The study also included fossil diesel and Jet-A, two sustainable aviation fuel candidates-BCH and C-4-and a fuel surrogate, dodecane, under varying injection pulse durations. Furthermore, seven types of diesel fuel were examined: a conventional fossil base diesel, an RME biodiesel, a B10 base/biodiesel blend, hydrotreated vegetable oil (HVO) renewable fuel, and three counterparts for fossil diesel, RME biodiesel, and HVO treated with a QAS-based viscoelasticity-inducing agent. All fuels treated with the QAS-based viscoelasticity additive were dosed at 1000 mg/kg, a concentration representative of commercial aftermarket fuel additive applications. It should be emphasised that the bulk properties of all examined fuels remain characteristic of commercial formulations, with the viscoelasticity agent exerting no discernible effect on these properties due to its minute concentration. A summary of the physicochemical properties of all fuels under investigation is provided in Table 3.1.

Table 3.1: Fuel Properties at ambient temperature (20°C) [123],[124],[125],[126].

Fuel Properties	Diesel	Dodecane	Jet-A	C-4	HVO	B10	FAME	RME	BCH
Density ρ [kg/m^3]	835	751	801	757	780	843	884	880	864
Kin. Visc. ν [mm^2/s]	2.80	1.44	1.41	1.53	3.90	2.92	3.50	3.55	4.34
Init. Boiling Pt. [°C]	155	214	130	161	180	158	330	348	227
Fin. Boiling Pt. [°C]	363	218	300	239.6	320	350	357	358	228
Surf.Tens. σ [mN/m]	28.7	25.3	24.7	22.3	25.9	29.8	32.2	31.5	32.7
P_{sat} [Pa]	237	184	900	758	380	260	400	420	14.4

Notably, dodecane and BCH are single-component fuels, so they possess consistent boiling points. In contrast, diesel, Jet-A, and C-4 are multi-component fuels, resulting in broader boiling ranges. Among these, diesel exhibits the widest boiling point range, indicative of its complex hydrocarbon mixture. Jet-A and C-4 also display significant boiling ranges. Additionally, BCH stands out with its relatively high boiling point and higher density and viscosity compared to the other fuels. Variability in cavitating flow dynamics is anticipated between mono-component fuels, such as dodecane, and complex, multi-component fuels, like diesel and Jet-A. This variability is attributed to each constituent's unique surface tension and vapour pressure characteristics, significantly impacting their cavitation behaviour [127]. Investigations into fuel blends have elucidated that the extent of cavitation does not correlate with blend ratio, underscoring the importance of factors beyond the fundamental properties of the fuels in the initiation of cavitation [128].

High-speed diffuse backlight illumination and schlieren imaging techniques were used to visualise in-nozzle flow and near-nozzle spray dynamics. Soot measurements and combustion characteristic analyses were conducted to assess the effects of QAS-based additives on combustion efficiency and emissions. Key combustion parameters, including lift-off length, liquid length, and ignition delay, were evaluated. Advanced diagnostic methods, such as OH* chemiluminescence and DBI extinction imaging, were employed to quantify soot and comprehensively analyse combustion behaviour. These methodologies provided essential insights into the physical and chemical processes influenced by QAS additives, supporting the optimisation of combustion performance and the reduction of emissions.

3.2. Pressure Chamber and Fuel Injection System

The experiments were conducted inside a sealed cubical vessel, as shown in Figure 3.5, which was equipped with fused-silica windows on all four sides for simultaneous visual observation using various optical techniques. The pressure inside the vessel was regulated using nitrogen flow delivered through four ports at the top of the vessel. After injection, the fuel-gas mixture was expelled through the exhaust at the bottom of the vessel. The pressure during fuel injection and ambient pressure was measured using pressure transducers connected to the fuel and exhaust lines. The fuel was pressurised to the desired injection pressure using a syringe pump.

Spray C and Spray D are equipped with nozzles of different sizes and shapes. The hole in the nozzle of Spray D is round and has a converging profile and is intended to be the non-cavitating version of Spray C. In contrast to Spray D, which was hydro-grinded, Spray C has a sharp inlet corner and a cylindrical hole profile. Hydro-erosion, the process of passing an abrasive slurry through the nozzle, is employed to minimise surface roughness and increase the radius at sharp corners. The specific geometries of Spray C and Spray D are detailed in

Table 3.2. A schematic representation of their nozzle geometries is shown in Figure 3.1, while microscope images illustrating the side view and injector hole outlet view of Spray D are presented in Figure 3.2. The isometric and sectional views of Spray D and Spray M are presented in Figure 3.3 and Figure 3.4 respectively.

Key parameters used in cavitation research, such as the Reynolds number (Re) and the cavitation number (CN), help to characterise the onset and behaviour of cavitation and are defined by equations 3.1 and 3.2, respectively. In addition, the discharge coefficient, which expresses the ratio of actual to theoretical mass flow rate through the nozzle, is provided in equation 3.3. Another crucial parameter, the K-factor, is defined in equation 3.4. It quantifies the conicity of a nozzle, with positive values indicating converging nozzles and negative values denoting diverging nozzles. These parameters are essential for understanding the flow and cavitation phenomena.

$$Re = \frac{\rho U d}{\mu} \tag{3.1}$$

$$CN = \frac{P_{inj} - P_{back}}{P_{inj} - P_{sat}} \tag{3.2}$$

$$c_d = \frac{\dot{m}}{A\sqrt{2\rho \Delta P}} \tag{3.3}$$

$$k\,factor = \frac{D_{inlet} - D_{outlet}}{10} \tag{3.4}$$

Table 3.2: ECN Spray C and Spray D properties [129],[130].

	Spray C	**Spray D**
Common rail injector	Bosch 3-22	Bosch 3-22
Injector nominal nozzle outlet diameter	0.200	0.186 mm
Nozzle K Factor	K=0	K=1.5
Nozzle Shaping	5% Hydro-eroded	Seeking Cd=0.86
Flow with 10Mpa ΔP	200 cc/min	228 cc/min

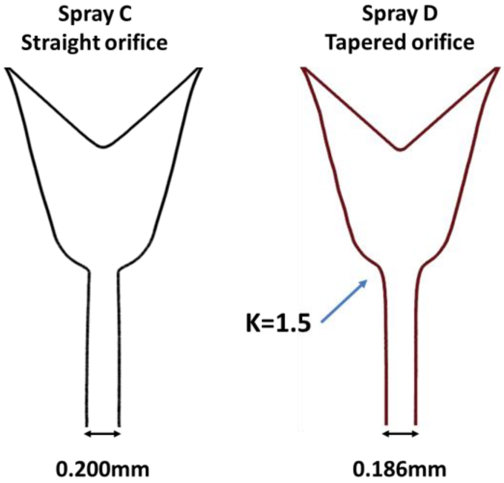

Figure 3.1: Schematic representation of Spray C and Spray D nozzle geometries. Spray C features a straight orifice with a diameter of 0.200 mm, while Spray D has a tapered orifice with a diameter of 0.186 mm and a convergence ratio of K=1.5.

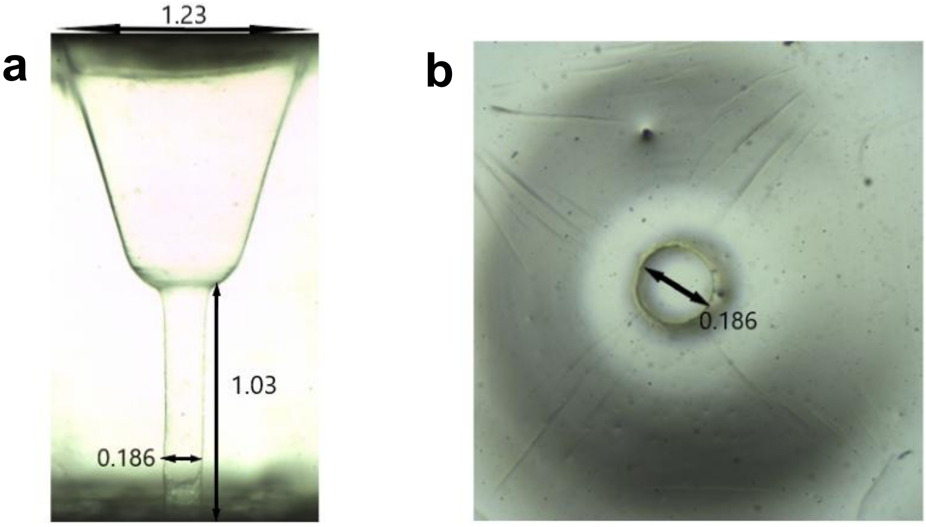

Figure 3.2: Side view (a) and outlet view (b) of Spray D nozzle made from acrylic, showing key dimensions in millimetres (mm).

Although acrylic nozzles can withstand pressures up to 1000 bar, repeating experiments wears out the nozzles and impairs the nozzle transparency, causing problems in the visualisation of nozzle flow. Considering the number of fuels and experiment repetitions needed for lower measurement uncertainty, the injection pressure of Spray D was limited to 900 bar. However, the maximum injection pressure for the Spray C injector was solely determined by visualisation constraints, as the injector hole became entirely opaque during the injection event at pressures exceeding 700 bar. Similar to Spray D, the maximum injection pressure of Spray M was determined considering the rigidity of the acrylic piece. Specifically referring to the Spray M layout, the pressure had to be limited to a lower value, as the complex geometry machined out of the acrylic part rendered the piece less rigid than Spray D. The basic characteristics of the mixing of diesel spray, such as spray angle and liquid penetration length, can vary considerably from one injector to another, or even from one hole to another within the same injector. Therefore, to minimise the effect of these variations on the results, experiments were repeated four times for each case.

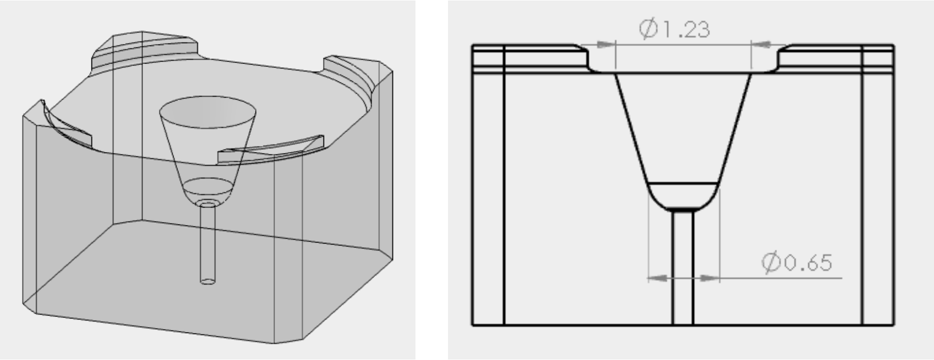

Figure 3.3: Isometric and sectional views of Spray D, showing key geometric features and dimensions in millimetres.

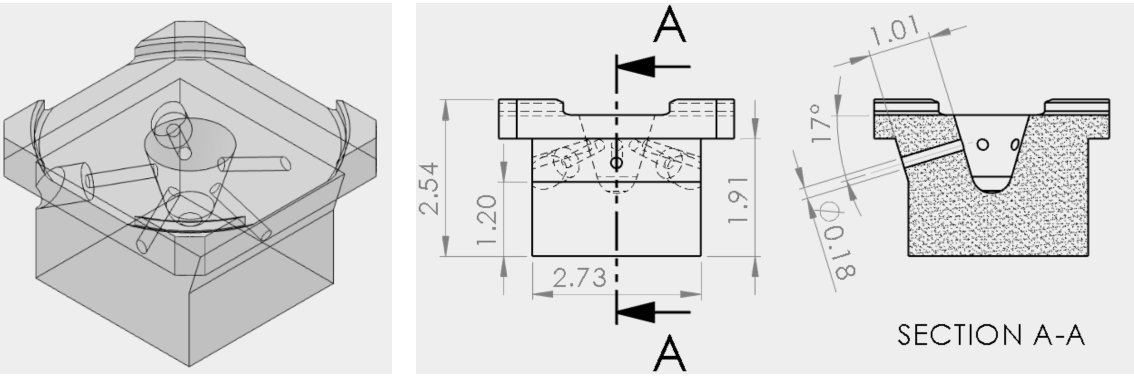

Figure 3.4: Isometric and sectional views of Spray M, showing key geometric features and dimensions in millimetres.

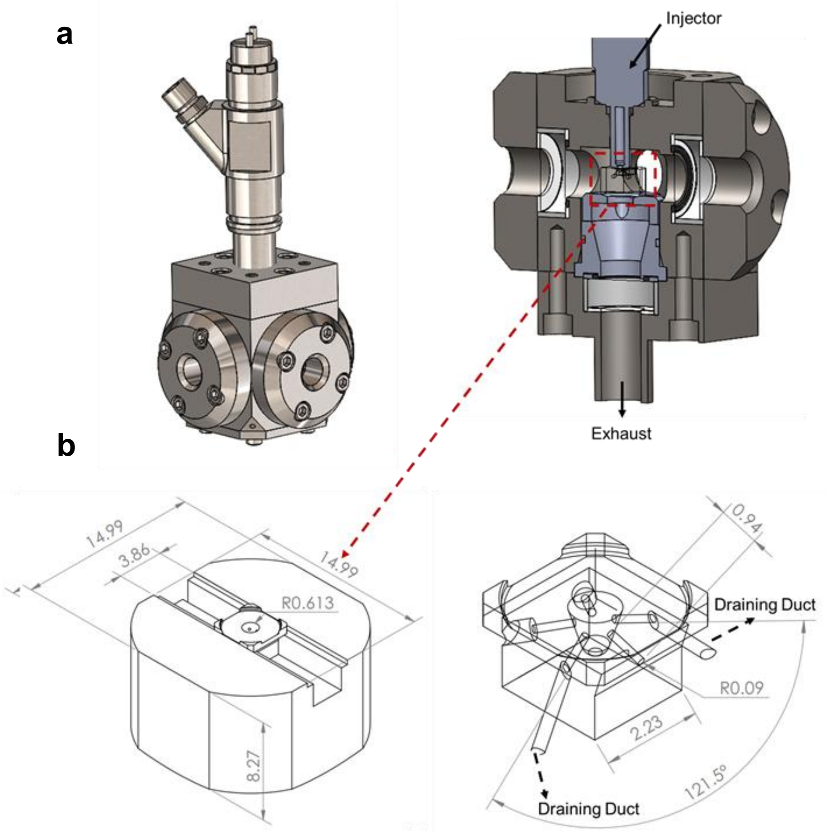

Figure 3.5: (a) Overall and section views of the spray chamber employed in the experiments. (b) CAD assembly of the Spray-M test piece with the dedicated acrylic pedestal. All dimensions are in mm.

3.3. In-Nozzle and Near-Spray Visualisation Setup

Visualising the in-nozzle flow of diesel injectors and the near-nozzle spray presents significant challenges due to the short time scales and turbulent multiphase flow involved. High-speed diffuse back-illumination imaging offers a viable solution for these issues, as it can provide detailed insights into the spray formation and fuel distribution process. High ambient and temperature conditions inside the combustion chamber can cause significant refractive index gradients, leading to false attenuation or beam steering effects. DBI addresses this issue by using a diffuser and a lens to create a quasi-Lambertian light distribution, which helps mitigate beam steering effects. This method ensures that imaging the in-nozzle flow and near-nozzle spray is more accurate and reliable, ultimately contributing to a better understanding of diesel injector performance and behaviour. The optical configuration, shown in Figure 3.6, enabled the simultaneous use of diffuse backlight illumination (DBI) and schlieren imaging in orthogonal alignment. Two pulsating LEDs supplied the light: blue (455±22 nm) for DBI and red (620±22 nm) for schlieren. The schlieren setup captured longitudinal vortices inside the injector hole as streak-like refractive index variations. Moreover, raw schlieren images were used to determine the spray-cone angle, providing better contrast at the spray edges than DBI images. Two separate CMOS cameras, the Photron SA-X2 and Phantom v2512, recorded high-speed images at 100,000 fps in tandem. Both cameras were equipped with long-distance microscopes (Infinity K2 with CF-2 objective for DBI and Mitutoyo 10x objective for schlieren) and triggered simultaneously by the injector driver. The active window dimensions were 640×176 pixels for the DBI system and 768×272 pixels for the schlieren system, with corresponding spatial resolutions of 3.90 µm/pixel and 3.24 µm/pixel, respectively. Although the in-nozzle visualisation shows the extent of cavitation inside the nozzle, it does not provide quantitative information about the cavitation. However, quantitative comparison is possible using image post-processing techniques as explained in section 3.4.

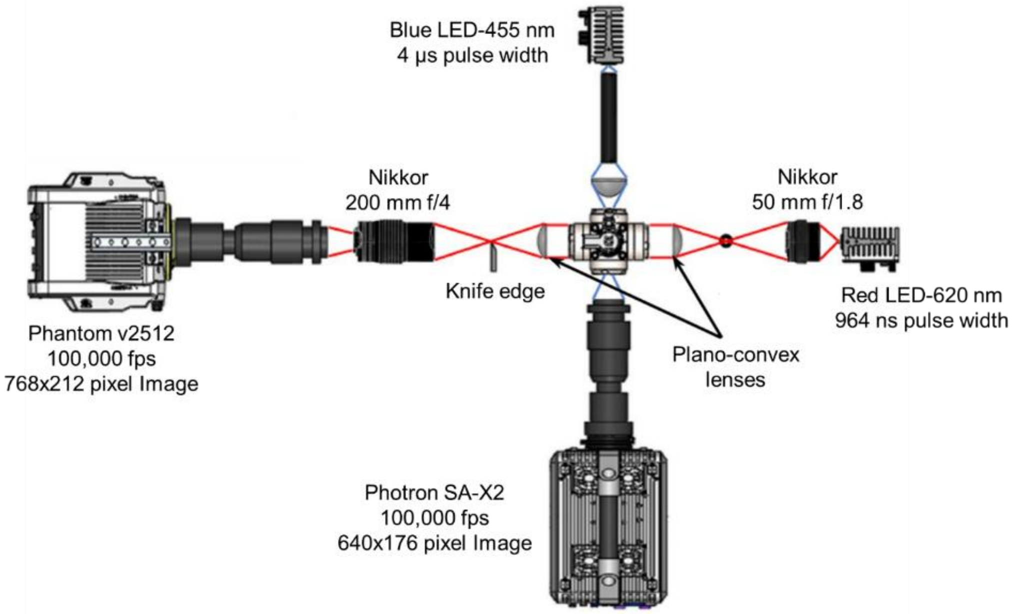

Figure 3.6: Schematic of the optical layout for the DBI (red LED) and schlieren (blue LED) imaging systems (reproduced from [103].)

Indicative sequences of raw DBI images obtained from the single-orifice Spray C and Spray D injectors during the experimental campaign are presented in Figure 3.7, whilst Figure 3.8 shows the corresponding raw Schlieren images for both configurations. The sequences in Figure 3.7a, referring to the straight Spray C injector, reveal that the entire injector hole is largely occupied by vapour, rendering it almost completely opaque. In contrast, the tapered design of Spray D, illustrated in Figure 3.7b, results in milder cavitation, with the majority of the nozzle occupied by pure liquid.

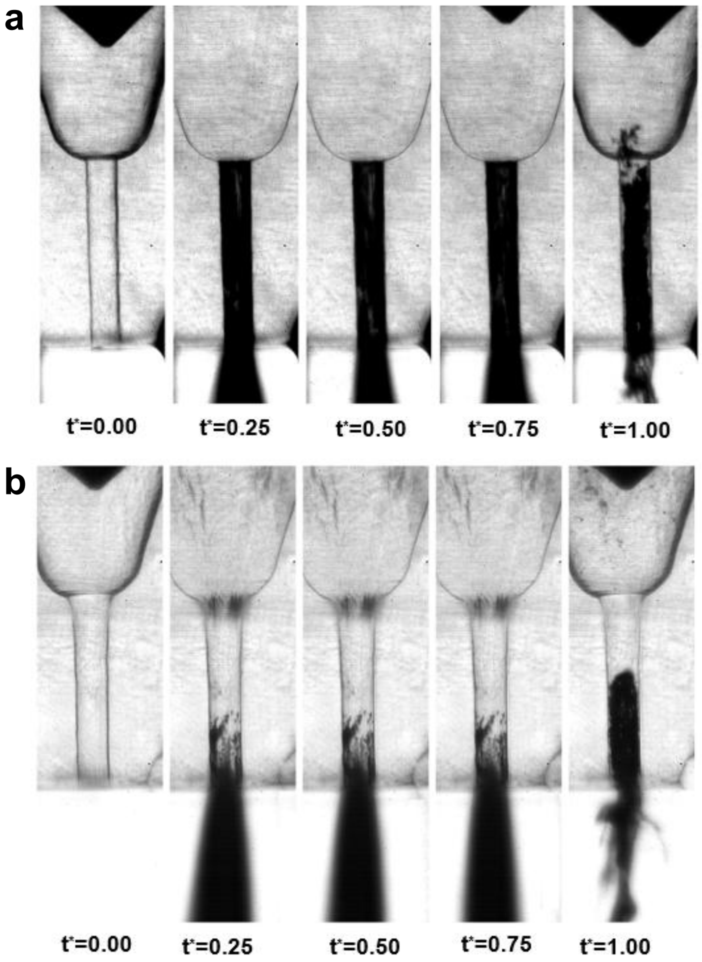

Figure 3.7: An indicative sequence of raw images covering the entire injection event for the cases of the single-hole injectors: (a) Spray C for injection and ambient pressures of 700 and 5 bar and (b) Spray D for 900 and 5 bar, respectively. The hydraulic injection duration is different for the two layouts, despite the identical electric pulse, owing to the different injection pressures and is therefore presented in a non-dimensional form.

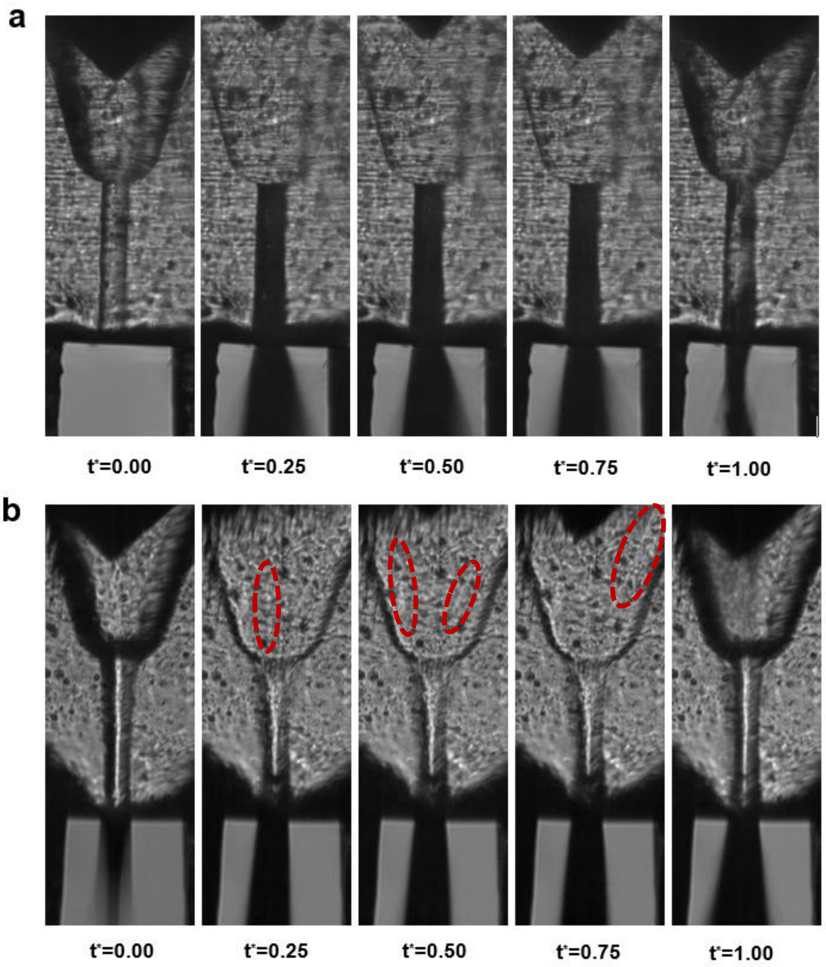

Figure 3.8: An indicative sequence of raw Schlieren images, with schlieren structures annotated, covering the entire injection event for the cases of the single-hole injectors: (a) Spray C for injection and ambient pressures of 700 and 5 bar and (b) Spray D for 900 and 5 bar, respectively. The hydraulic injection duration is different for the two layouts, despite the identical electric pulse, owing to the different injection pressures and is therefore presented in a non-dimensional form.

3.4. Image Processing

The images were recorded at a rate of 100,000 frames per second using the experimental setup illustrated in Figure 3.6. Images were processed using advanced techniques to extract quantitative data on cavitation and spray behaviour, enabling a detailed investigation of their temporal evolution. Two specialised algorithms were developed: one for quantifying the spray cone angle and another for measuring cavitation within the nozzle. High-resolution imaging facilitated the precise detection of fluctuations in both spray dynamics and cavitation phenomena.

The cavitation image analysis process, as depicted in Figure 3.9, comprised several critical steps. First, the region of interest (ROI) was extracted by cropping the raw images to focus specifically on the nozzle's cross-sectional area. A background subtraction process was then employed, where an image of stagnant liquid was subtracted to isolate cavitation features by removing irrelevant elements. Following this, a denoising algorithm was applied to minimise noise, thereby ensuring that only significant cavitation features were retained. Subsequently, the images were masked and binarised using adaptive thresholding based on Otsu’s algorithm. Developed by Otsu [131], this method automatically determines an optimal global threshold by minimising intra-class variance. This approach effectively separates foreground (cavitation regions) from background, enhancing the clarity and precision of the detected cavitation features. From these binarised images, the vapour-projected area was measured for each frame and converted into the corresponding physical area by applying a pixel-to-millimetre conversion derived from a reference scale image. By implementing this comprehensive image processing methodology, accurate quantification of the cavitating area within the nozzle's cross-sectional plane was achieved. A comprehensive description of the algorithm used for this classification is provided in the Appendix for reference.

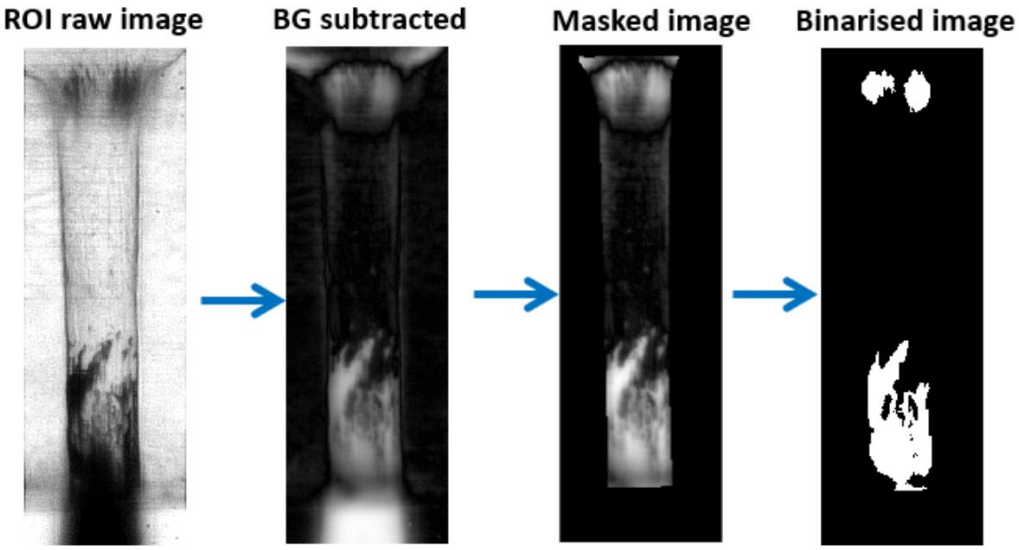

Figure 3.9: Post-processing steps for quantifying projected cavitation area.

Similarly, in the analysis of fuel spray images, the region of interest was cropped and binarised at an appropriate threshold to facilitate the calculation of the spray cone angle, as illustrated in Figure 3.10. Edge detection on the binarised image was performed using the Canny edge detection algorithm [132], which included smoothing the image with a Gaussian filter to minimise noise, calculating intensity gradients to determine edge strength and direction, applying non-maximum suppression to retain only the most prominent edges, and employing double thresholding with hysteresis to distinguish true edges from noise. To reduce the impact of rogue droplets on the measurement, additional denoising was applied to the detected edges. The centroids of the two edges of the spray were then identified, and the spray cone angle was calculated based on their positional data. The developed code for near-nozzle spray measured the spray cone angle throughout the entire injection process, enabling the detection of fluctuations in spray dynamics due to the high temporal and spatial resolution of the recorded images. The detailed implementation of this classification algorithm is provided in Appendix for reference.

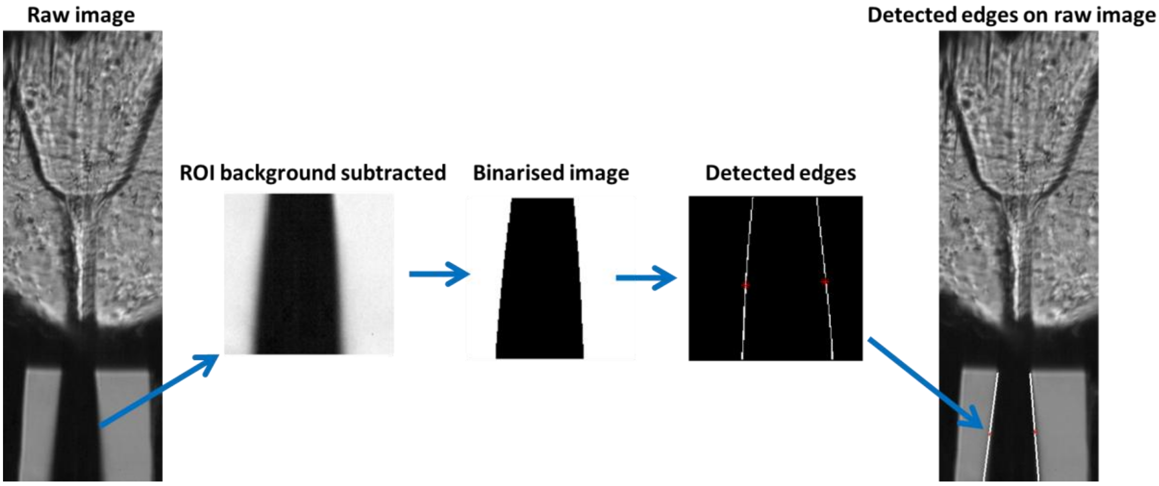

Figure 3.10: Post-processing steps for calculating spray angle.

A more advanced approach is used to differentiate vortical cavitation from geometric cavitation in the Spray M injector, a bespoke algorithm was developed to track the eccentricity and spatial positioning of vaporous structures captured in each frame. This algorithm builds upon the binarisation technique previously applied in single-orifice configurations. Vortical cavitation was identified by applying specific thresholds to both the eccentricity and location of the binarised structures within the nozzle. Eccentricity, a key parameter in this analysis, quantifies how much a shape deviates from a perfect circle by comparing the object to the ellipse that best fits it. Mathematically, it is defined as the ratio of the distance between the foci of the ellipse to the length of its major axis, ranging from 0 (a perfect circle) to values approaching 1 (a highly elongated shape). This is expressed in Equation 3.5:

$$\varepsilon = \sqrt{1 - \frac{\mathrm{b}^2}{a^2}} \tag{3.5}$$

where a and b are the lengths of the major and minor axes of the ellipse fitted to the object.

Vapour structures exhibiting high eccentricity and low circularity are typically associated with vortex (string) cavitation, characterised by, elongated flow patterns [32]. These elongated vapour structures are not bound by the nozzle geometry. On the contrary, geometric cavitation tends to produce more irregular and localised structures that are often asymmetric. These originate at sharp corners where the pressure drops below the vapour pressure. To effectively classify the two cavitation types, vortical cavitation was specifically identified by establishing thresholds for both eccentricity and spatial distribution of the binarised structures within the nozzle. The detailed implementation of this classification algorithm is provided in Appendix for reference. By correlating these parameters, the algorithm ensures a robust differentiation between the two cavitation types, even in regions with complex flow dynamics. For example, the cavities depicted in Figure 3.11a are classified as vortical cavitation, as their eccentricity values surpass the designated threshold. The efficacy of these identification criteria becomes particularly evident in the entrance region of the nozzle, as shown in Figure 3.11b. Despite both detected structures exhibit comparable eccentricity values, the cavity circled in blue is classified as geometric cavitation, while the one circled in red is identified as vortical cavitation, due to their respective locations within the orifice. This methodology enhances the accuracy of cavitation classification and also provides deeper insights into the underlying fluid dynamics governing cavitation behaviour within multi-hole injector nozzles. By integrating eccentricity and spatial positioning into the analysis, the algorithm provides a multi-dimensional perspective on cavitation structures, enabling precise differentiation between geometric and vortical phenomena.

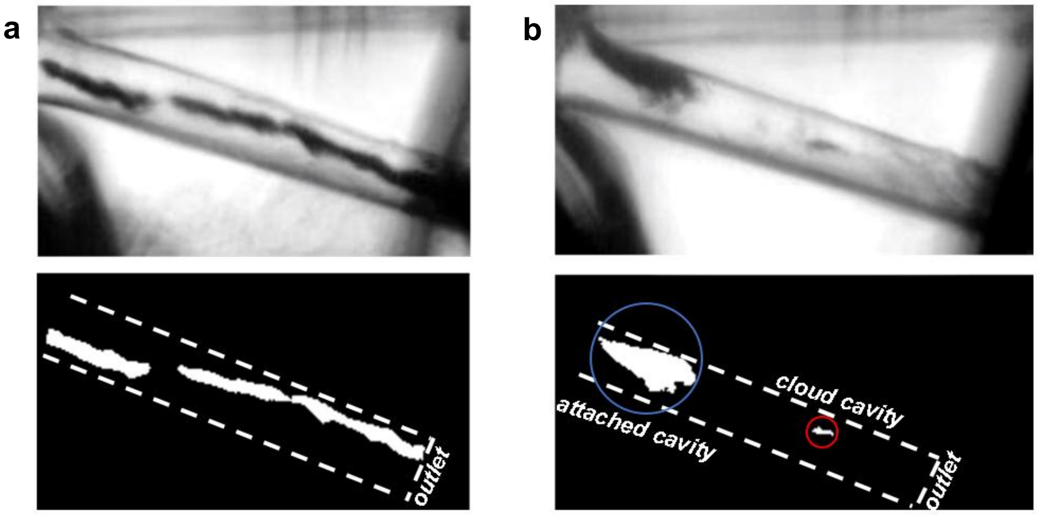

Figure 3.11: Detection of cloud and vortical cavitation in the Spray-M injector: **(a)** Case of well-established elongated cavity identified by the eccentricity criterion, **(b)** case of both attached and vortical cavities identified through a combination of eccentricity and location criteria.

3.5. Combustion Measurements

The assessment of diesel combustion characteristics involves examining several key parameters, including liquid length, ignition delay, and flame lift-off length. The liquid length refers to the distance from the injector to the point where the fuel stays in its liquid form. Flame lift-off length is the distance from the point of fuel injection to the location where the flame becomes stable. Ignition delay is the time between the introduction of a fuel-air mixture into the combustion chamber and the start of the combustion.

Quantifying the liquid length is subject to uncertainties associated with the diagnostic approach employed. Pickett et al. [133] conducted a study exploring various optical diagnostics commonly used to measure the liquid length of diesel fuel sprays, including Schlieren imaging, laser extinction, and diffuse backlight illumination. They observed that each method has its strengths and limitations, and their effectiveness can depend on the experimental conditions and needs. Nevertheless, the researchers found that a method involving a small laser beam with a large collection optic was particularly noteworthy due to its ability to minimise beam-steering effects. Beam steering occurs when refractive index gradients, caused by variations in density, temperature, and composition, distort the light paths and create false intensity variations. DBI-EI employs a customised engineered diffuser that provides a spatially uniform and quasi-Lambertian light source, ensuring that any refracted light ray is replaced by another of equal radiance. This characteristic significantly suppresses errors introduced by beam steering. Unlike Mie scattering, which is highly sensitive to particle size and scattering angle, DBI-EI relies on self-calibrating extinction measurements that are more resilient to refractive index variations. Additionally, by controlling the angular distribution of illumination, DBI-EI effectively compensates for distortions, ensuring improved accuracy in determining liquid penetration lengths. Consequently, this method has demonstrated a tenfold reduction in beam-steering-induced attenuation compared to previous high-speed optical setups, making it a preferred standard for high-pressure, high-temperature spray diagnostics [134].

For the combustion measurements, diffuse backlight illumination extinction imaging and OH^* chemiluminescence techniques were employed to measure several key combustion parameters, including ignition delay, liquid length, flame lift-off length, and soot production. Experiments were conducted using a high constant-volume pre-burn chamber at the Combustion Research Facility of Sandia National Laboratories.

The experimental apparatus employs a pre-burn, constant-volume combustion approach. First, the cylindrical chamber is filled to a predetermined density with a lean premixed charge of acetylene (C_2H_2), oxygen (O_2), carbon dioxide (CO_2), water vapour (H_2O), and nitrogen (N_2). Spark ignition of this pre-burn mixture causes a rapid rise in temperature and pressure, establishing the required high-pressure/high-temperature ambience. Over the ensuing ~1 s cool-down period, governed by heat transfer to the 188 °C electrically heated walls, pressure and temperature decrease slowly; when the target conditions are reached, fuel is injected and auto-ignites, initiating the main combustion event. The full sequence of events is illustrated in Figure 3.12, which shows the initial pressure rise, the cool-down phase, and the point of fuel ignition.

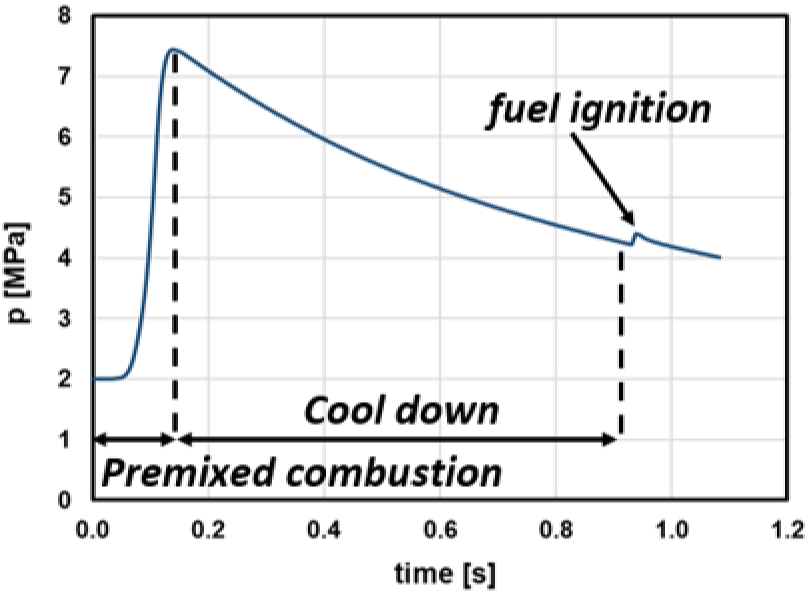

Figure 3.12: Pressure trace showing the initial combustion, cooling phase, and subsequent ignition during the experimental sequence.

A common rail system was employed to inject fuel using an ECN Spray D injector at a pressure of 1500 bar. The experimental conditions were selected to represent the typical operating conditions of modern diesel engines, with a chamber oxygen concentration set at 15% and ambient temperature ranging from 800K to 1200K. Each case was conducted four times using various fuels. Specifically, the fuels investigated were base diesel, diesel with additives, a blend of 10% biodiesel and 90% diesel (B10), B10 with additives, hydrotreated vegetable oil (HVO), HVO with additives, and rapeseed methyl ester (RME) biodiesel. High-speed raw images obtained with DBI-EI and OH* chemiluminescence images showing the temporal evolution of combustion and emissions production were presented for the case of 1200K ambient and 15% oxygen concentrations in Figure 3.14. The results of the experiments are presented and discussed in section 4.4.

The optical arrangement used for combustion measurements, enabling simultaneous implementation of two optical techniques, is depicted in Figure 3.1. Illumination is provided by a high-intensity green LED (519 nm, 34 nm FWHM), with the light beam passing through a Fresnel-type field lens and an engineered diffuser, to create a large (100 mm diameter) background of diffuse light for the DBI-EI imaging. A high-speed CMOS camera placed opposite of the illumination source and fitted with a band-pass filter collects LED irradiation at a frame rate of 100,000 Hz, twice that of the LED illumination, in a skip-pulse arrangement to provide flame luminosity corrections. A dichroic beam splitter is employed to reflect ultraviolet wavelengths below 350 nm, such that the excited state of the OH radicals could be captured by an intensified high-speed CMOS camera. The camera was equipped with a 45 mm f/1.8 UV lens and a series of filters aiming at capturing OH*-chemiluminescence emitting near 308 nm (10 nm FWHM). The intensified camera system was operated at a rate of 50,000 frames per second. The digital spatial resolutions are 5.92 μm/pixel and 7.33 μm/pixel for the DBI-EI and OH*-chemiluminescence methods, respectively.

Table 3.3: Operating parameters and range of experimental conditions examined in the present investigation.

Parameter	Details
Injection Pressure	150 MPa
Injector	ECN Spray D
Injection duration	1.6 ms
Oxygen concentration ratio	15 %
Ambient density	22.8 kg/m^3
Ambient temperature	800-1200 K

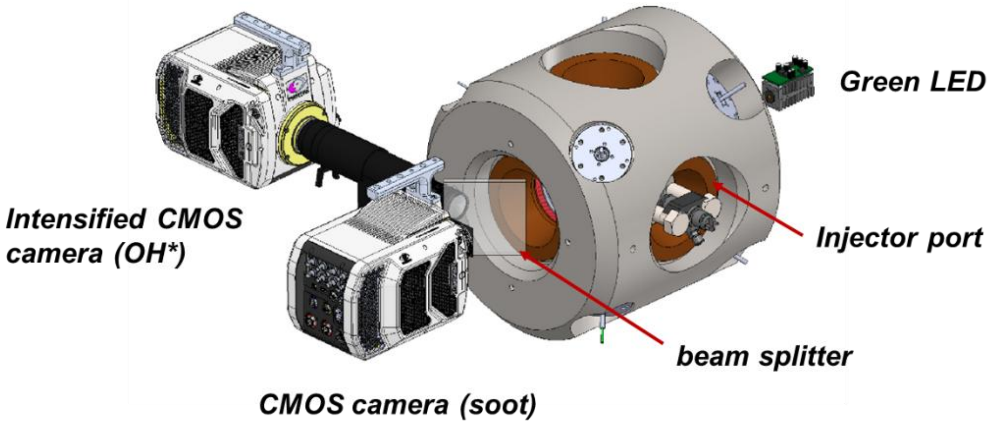

Figure 3.13: Schematic of the constant volume chamber and the optical system (adapted from [75]). The chamber has a cubical shape with round ports 105 mm in diameter allowing optical access through the vessel. The fuel injector is clamped onto the frontal side port using a metallic insert.

Figure 3.14 presents representative raw images from both DBI-EI and OH*, illustrating the temporal evolution of a combustion event. The diffuse-light images in Figure 3.14a depict the liquid extent of the fuel injected by the single-hole Spray D injector, the emerging cloud of soot particles, and the flame natural luminosity from 1.0 ms after the start of injection onwards. Figure 3.14b shows the evolution of the OH^* signal simultaneously captured by the intensified camera, indicating regions of high-temperature combustion. It is important to note that the OH^* images clearly exhibit significant interference from soot incandescence, which, nevertheless, does not affect the measurement of flame lift-off length and ignition delay. Soot luminosity also emits broadband radiation with substantial emission at 310 nm, but OH chemiluminescence dominates in the lift-off length region where soot has not yet formed.

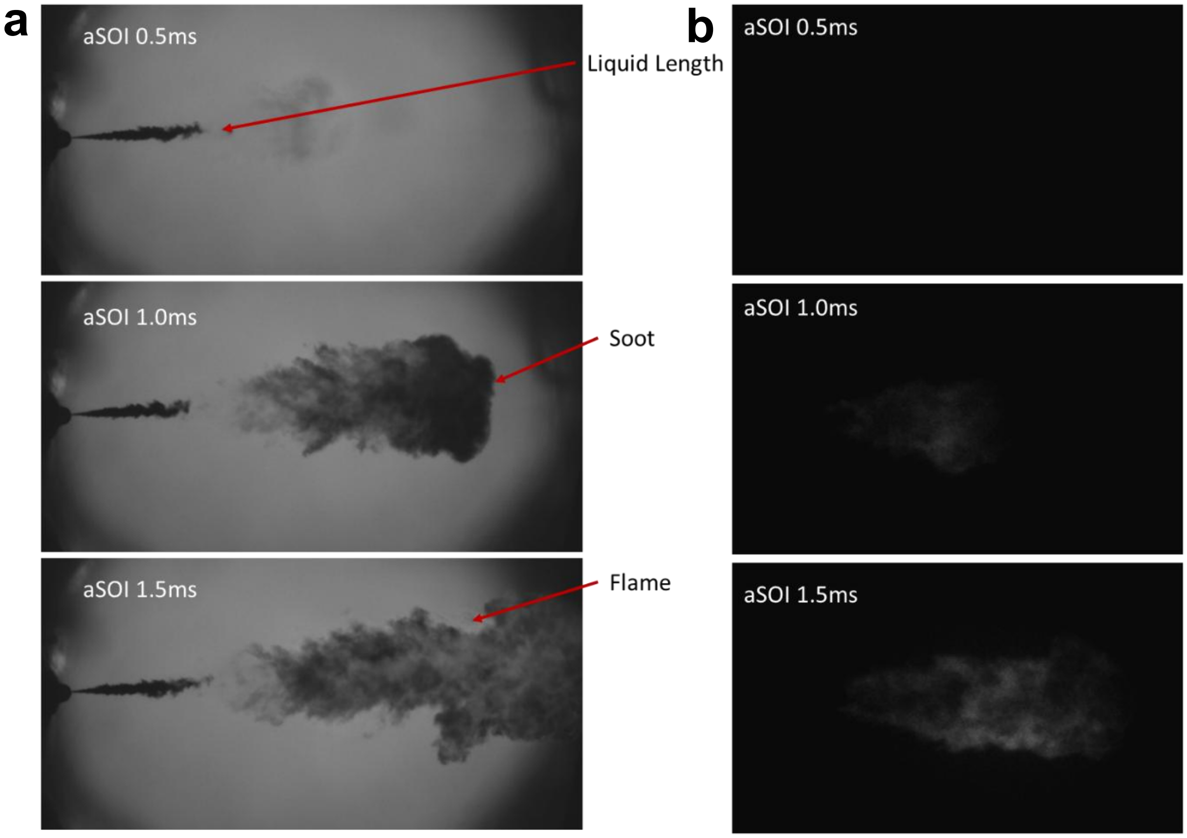

Figure 3.14: Time sequence of high-speed raw (a) DBI-EI and (b) OH* chemiluminescence images indicating the temporal evolution of combustion and emissions production (T=1200 K, ρ=22.8 kg/m3 and 15% O2). Contrast of OH* images has been enhanced to enhance clarity.

3.6. Soot Quantification

Soot quantification through DBI-EI follows Beer-Lambert's law, which relates optical thickness to the attenuation of light as it passes through a soot cloud. The method employs a diffuser and lens to achieve a quasi-Lambertian light distribution, reducing the impact of beam steering and improving measurement accuracy. The optical thickness (KL) is determined by comparing the initial light intensity with the intensity recorded after transmission through the soot cloud as presented in equation 3.6, where I_{in} and I represent the intensity of the light beam prior and past its interaction with the soot cloud.

$$\frac{I}{I_{in}} = e^{-KL} \tag{3.6}$$

High-speed imaging is carried out using an LED pulsating in sync with alternating camera frames, enabling frame-pair subtraction. In this approach, each LED-on frame, containing transmitted light, background, and broadband soot emission, is subtracted by the subsequent LED-off frame, which includes only background and soot emission.

A structured image processing workflow underpins accurate soot quantification. An overview of the complete procedure is provided in Appendix Figure A.4, which visualises the methodology defined as follows. The process begins with background correction to minimise illumination inconsistencies and suppress noise. Prior to fuel injection, frames are averaged to generate reference background images: one for the LED-on condition (I_0), capturing spatial profile of light intensity and the one for the LED-off condition ($BG2$), representing ambient noise, The LED-off reference ($BG2$) is captured between LED pulses during the same general time period as I_0, allowing it to capture dynamic background contributions such as ambient emission, or broadband soot luminosity. Additionally, an average of frames recorded before any LED pulses is used as a static background image (BG). This image excludes LED illumination, soot, or liquid, containing only ambient light and camera noise. Used together, I_0, $BG2$, and BG form a pixel-wise correction factor (CF) that compensates for spatial non-uniformities in illumination and background inconsistencies. This CF, acting as a spatially varying flat-field correction, is then applied to each raw, frame of interest, LCF frame to mitigate these effects. This CF is used in updating the local dark frame as presented in equation 3.7.

$$CF = \frac{(BG - BG2)}{(I_0 - BG2)} \tag{3.7}$$

The correction factor is applied to LCF, to update the local dark frame (D), yielding a corrected dark frame (D_{cr}) as described by:

$$D_{cr} = D + (LCF - D) \cdot CF \tag{3.8}$$

In addition to background corrections, specialised masks are created to exclude non-physical regions affected by beam-steering artefacts, liquid fuel scatter, and areas extending beyond the predefined region of interest. These masks are determined using intensity thresholds and liquid length measurements. Specifically, an intensity mask removes low-intensity background noise, and a spatial mask confines the analysis to within the maximum liquid penetration length. By combining these two masks, only valid pixels remain, enabling the median filter to act solely on meaningful regions. This targeted approach suppresses noise without compromising essential image features, providing cleaner results for subsequent processing. Then, the background-corrected transmission image (T) is then computed as:

$$T = \frac{I}{I_{in}} = \frac{LCF - D_{cr}}{I_0 - BG} = e^{-KL} \tag{3.9}$$

From the transmission image, the optical thickness, *KL* is obtained using the background corrected 2D extinction images from Beer-Lambert's law, where *K* is the dimensional extinction coefficient and *L* is the optical path length through the soot cloud. Subsequently, the soot volume fraction, (f_v) can be calculated as follows:

$$f_v = \frac{K\lambda}{k_e} \tag{3.10}$$

$$f_v L = KL\frac{\lambda}{k_e} \tag{3.11}$$

where λ is the wavelength of irradiation and k_e is the non-dimensional extinction coefficient. Skeen et al. [135] conducted a comprehensive study to establish the non-dimensional extinction coefficient for soot particles across diverse combustion environments. Their research centred on analysing soot properties within high-pressure diesel sprays and steady laminar ethylene flames. Utilising high-speed extinction imaging at wavelengths of 406 nm, 520 nm, 623 nm, and 850 nm, they explored the variations in the optical properties of soot with respect to these wavelengths. The findings indicated that the extinction coefficient values for soot are significantly influenced by the wavelength of the incident light and the specific combustion conditions. For instance, in their high-pressure dodecane spray experiments, a k_e ratio of 1.5 was observed between 623 nm and 850 nm. The k_e values reported are of the order of 2.19-8.9 for wavelengths in the range 406-850 nm. A value of 7.8 has been used in the present investigation, chosen to correspond with the characteristics of soot generated under our specific experimental conditions and the wavelength of the incident light employed in our measurements. The soot mass can be estimated utilising the optical thickness values at each pixel of the image, with the assumption that the soot density remains constant at 1.8 g/cm^3 [135]:

$$m_{soot} = \iint \rho_{soot} \cdot f_v L \cdot dA = \iint \rho_{soot} \cdot \lambda/k_e \cdot KL \cdot dA \tag{3.12}$$

where *dA* is the infinitesimal projected area onto the camera detector. Consequently, in the context of the two-dimensional image obtained, the soot mass encompassed in each projected pixel area is:

$$m_{sootpixel} = \rho_{soot} \cdot \lambda/k_e \cdot KL \cdot \Delta A_{pixel} \tag{3.13}$$

The soot mass in each frame of the combustion event was quantified by integrating the pixel intensities across the entire image. After finding the soot mass corresponding to a pixel, the corresponding soot mass to the two-dimensional area was calculated using the pixel-to-mm scale.

In accordance with ECN guidelines [136], the farthest extent of the fuel liquid phase, commonly referred to as the liquid length, was also determined using diffused back-illumination images. During the quasi-steady injection period, the liquid length was evaluated for each frame and then averaged over that period to obtain representative values.

Accurate characterisation of the liquid length is vital for understanding fuel–air interaction, making it a key parameter in combustion analysis. Nevertheless, inconsistencies in experimental setups, calibration procedures, and post-processing can result in notable discrepancies in measured liquid length data [133],[137]. To address these challenges, members of the ECN have collectively adopted the DBI technique as a standard, chiefly because its self-calibrating capability helps maintain consistency across different facilities [138]. By avoiding threshold-dependent methods, DBI minimises variability and thus supports reliable comparisons of liquid length. Following the ECN guidelines described in [136], the approach used here involves examining image intensity along the spray axis to pinpoint the precise boundary of the liquid phase. The resulting liquid length values, computed for each frame during the quasi-steady injection period, were then averaged to reduce frame-to-frame variability, and the corresponding time-averaged liquid length results are presented.

In a parallel approach, the ignition delay (ID), defined as the interval between the onset of injection and high-temperature ignition, was determined using OH^* chemiluminescence measurements. High-speed imaging data were processed frame by frame to detect significant intensity changes. Background subtraction, performed by averaging the first fifteen frames, isolated the flame's chemiluminescence from ambient noise. Each frame was normalised against the background, and aggregate intensity was computed as the sum of pixel brightness values. By comparing the aggregate intensity of consecutive frames, the algorithm identified sudden increases indicative of ignition. A predefined threshold was applied to these intensity differences to filter out minor fluctuations and pinpoint the ignition event. The ignition delay was calculated as the time difference between the onset of injection and the ignition frame, with corrections applied for hydraulic delay to ensure accuracy. This ID calculation also accounts for the hydraulic delay, ensuring accuracy.

The fuel-air mixes up to the lift-off; consequently, the lift-off significantly influences the soot formation processes [94],[139]. Therefore, the lift-off length is calculated using the ECN guidelines [138],[140]. In this method, a levelling of value, set at 50% of the peak intensity in the lift-off region, is independently applied both above and below the liquid jet, as depicted in Figure 3.15, and the final lift-off length is obtained by averaging these two measurements. Determining the lift-off length relies on advanced image processing of high-speed chemiluminescence data. The process begins with the pre-processing of raw image frames to eliminate noise and normalise intensity values. This includes background subtraction, where a reference image capturing the ambient background signal is subtracted from all frames, ensuring that only the flame's chemiluminescence is retained. The injector tip is designated as the spatial origin, calibrated using a predefined scale in pixels per millimetre.

To locate the lift-off length, a pixel intensity threshold is applied to the chemiluminescence data. In line with ECN standards, this threshold is set at 50% of the peak intensity observed in the flame’s lift-off region. The algorithm scans axially from the injector tip to find the farthest upstream location where the chemiluminescence intensity surpasses this threshold. This process is performed separately for the regions above and below the liquid jet, ensuring that both sides of the flame are considered. Once the axial positions of the lift-off points above and below the liquid jet are determined, the final lift-off length is calculated as the average of these two measurements. This method ensures robust and consistent results, accounting for potential asymmetries in the flame structure.

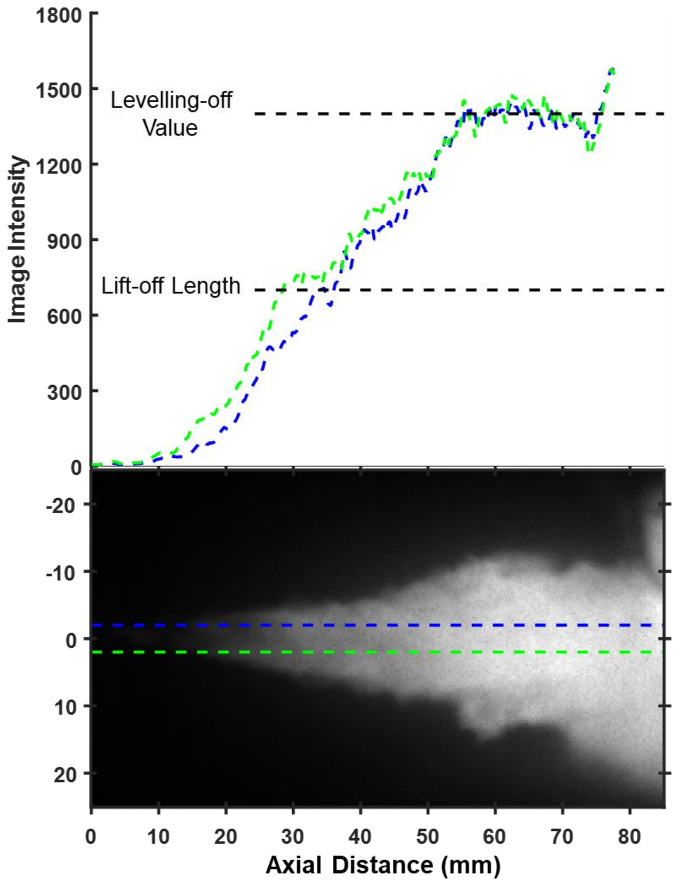

Figure 3.15: Finding lift-off length using 50% of the levelling-off value and averaging the upper and lower parts, the example for 1200K ambient for base diesel.

3.7. Experimental Uncertainty and Repeatability

To ensure the reliability of the measurements, all experiments were conducted under well-controlled, standardised boundary conditions in accordance with ECN recommendations. The injector, chamber, and optical arrangements were kept unaltered throughout the campaign to ensure repeatability and minimise systematic variations. Each test case was repeated four times to establish statistical repeatability, and the presented results correspond to the ensemble averages of these repetitions. The shaded error bands shown in the figures depicting the projected cavitation area and spray cone angle, represent the standard error of the mean calculated from these repeated injections. For each quantity, the standard deviation (σ) of the measured parameter across the four runs was divided by the square root of the total number of repetitions (n = 4) to obtain the standard error $\left(\frac{\sigma}{\sqrt{n}}\right)$. Plotting the mean measurement alongside this standard error interval produces the shaded region around the mean, thereby illustrating the variability among repeated injections. This approach provides a reliable measure of experimental repeatability and quantifies the statistical uncertainty associated with time-resolved quantities for cavitation area and spray cone angle.

For parameters derived from image analysis, uncertainty arises primarily from spatial resolution, image thresholding and temporal resolution. The in-nozzle and near-nozzle imaging resolution (3.24 to 3.90 μm per pixel) implies that features within the projected nozzle area where cavitation develops (field of view ≈ 0.2 mm × 1.03 mm, roughly 62 px × 318 px at 3.24 μm per pixel) carry a boundary-location ambiguity of order 0.3 to 0.5 px; for projected cavitation area this corresponds to a conservative geometric uncertainty of about 2 to 3% via perimeter-based pixel perturbation, whereas for spray cone angle, which is computed from pixel-geometry ratios, the pixel-to-mm calibration cancels and the scale factor does not directly contribute to angle uncertainty. Threshold sensitivity was assessed by varying the segmentation level within a narrow, objective range around the nominal value. The resulting changes in area and angle remained within to the standard error of the mean throughout the injection, as the high contrast of the raw images and the post-processing steps made the results less sensitive to threshold choice. It's worth noting that the present results are two-dimensional projections rather than volumetric reconstructions, potential overlap of cavitation structures along the line of sight remains a source of uncertainty in the projected area.

For combustion imaging, DBI-EI was used to suppress beam-steering bias and background emission [134], and a self-calibrating extinction acquisition with frame-pair subtraction provided a consistent baseline across fuels and runs. With spatial resolutions of 5.92 and 7.33 μm per pixel for the liquid-length and lift-off measurements, respectively, and lengths of ~20–30 mm, the resulting spatial-resolution uncertainty is ~0.01% (relative). The temporal resolution, governed by the high-speed camera frame rate (100,000 fps) and exposure time (10 μs), contributes an absolute timing uncertainty of ±5 μs from frame quantisation and intra-frame averaging, which for an ignition delay of 300 μs corresponds to ±1.67%. Calibration of optical magnification and light-intensity uniformity was verified prior to each measurement, and all combustion experiments were repeated four times to ensure statistical reliability. Because all experimental setups and procedures were fully standardised, any remaining systematic uncertainty is consistent across fuels; consequently, the results are presented on a comparative basis and the conclusions rest on relative differences rather than absolute values.

4. Results and Discussion

4.1. Introduction

This chapter presents the results and discusses the effects of fuel additives and compositions on in-nozzle flow, cavitation behaviour, spray dynamics, and combustion characteristics. The results are organised into three sections.

The first section investigates the impact of QAS-based additives in diesel fuel. High-speed imaging techniques, including diffuse back illumination (DBI) and schlieren imaging, were utilised to examine the cavitation and spray characteristics of diesel, biodiesel, and QAS-enhanced diesel. The results demonstrate how the addition of QAS impacts cavitation suppression, vortex formation, and spray dynamics.

The second section extends the analysis to sustainable aviation fuels and conventional jet fuels, focusing on their cavitation and spray dynamics using ECN Spray C and Spray D nozzles. This section explores how different fuels and varying injection pulse durations influence cavitation and spray dynamics. The findings emphasise the importance of nozzle geometry and fuel properties in optimising spray stability and mitigating cavitation.

The third section investigates the impact of QAS-based additives, on soot emissions and combustion characteristics in conventional and biodiesel fuels. High-speed diffuse backlight illumination extinction imaging and OH^* chemiluminescence were employed to assess combustion characteristics such as ignition delay, flame lift-off length, and soot emissions. The findings clarify the effect of QAS-based additives on soot emission behaviour across different fuel blends.

4.2. Assessing Fuel Additive Effects

High-speed diffuse backlight and schlieren imaging were employed to quantify the influence of additives inducing viscoelasticity in diesel fuel on in-nozzle cavitation evolution and expelled spray morphology. This imaging was applied to two single-hole true-scale transparent injectors with straight and tapered orifice layouts (ECN Spray C and Spray D), as well as a five-hole configuration (Spray M). Specifically, we compared, for the first time, the in-nozzle cavitating flow and its effect on near-nozzle spray formation of a non-Newtonian diesel fuel sample treated with a QAS-based additive exhibiting viscoelastic effects, and biodiesel (FAME), against conventional diesel fuel. The operating conditions included injection pressures of 500–900 bar and ambient pressures of 1–20 bar, as outlined in Table 4.1.

Following preliminary testing, the injection pressures for the Spray D and Spray M layouts were limited to 900 and 500 bar, respectively, to permit at least four injection events per fuel and ambient condition without rupturing the acrylic component. The lower pressure limit for the Spray M layout was necessary due to its complex geometry, which reduced rigidity compared to Spray D. In contrast, the injection pressure for the Spray C injector was constrained by visualisation limitations; at pressures exceeding 700 bar, the injector hole became completely opaque during injection.

Table 4.1. Matrix of conducted test cases. The Reynolds number was calculated using the orifice diameter d_o, as a characteristic length scale.

Injector layout	**Spray C**	**Spray D**	**Spray M**
Injection pressure [10^5 Pa]	700	900	500
Ambient gas		N_2	
Ambient temperature [K]		293	
Ambient pressure [10^5 Pa]	1-5-20	5-20	1-5-20
Ambient density [kg/m^3]		1.15-5.76-23.09	
Re$\left(=\frac{u\cdot d_0}{v_f}\right)$	15370 (700/5bar)	17460 (900/5bar)	12800(500/5bar)
CN$\left(=\frac{p_{inj}-p_{back}}{p_{back}-p_{sat}}\right)$	143-34 (5-20bar)	185-44 (5-20bar)	102-24 (5-20bar)

4.2.1. Spray C Results

In this section, the results for the Spray C injector nozzle are presented, focusing on the analysis of high-speed images captured during the injection event. Based on these images, the probability of vapour presence and the corresponding standard deviation were calculated. Owing to the straight layout of the injector-hole design, Spray C experiences significant cavitation, leading to the nozzle being almost entirely filled with vapour throughout the injection process, as shown in Figure 4.1a. This observation is supported by the high mean probability values obtained. However, this does not necessarily imply that the entire orifice volume is occupied by vapour; rather, an external layer surrounding the wall periphery may be present, obstructing light penetration further into the nozzle. High local standard deviation values suggest the existence of transient cavities in the core region of the injector. The presence of these transient vapour structures is more evident in the images related to the additised sample. In these images, a narrow area with low mean probability values can be observed, while the corresponding standard deviation reaches its maximum values. The raw images for the additised sample, as presented in Figure 4.1, provide a visual representation of the evolution of transient cavities within the nozzle.

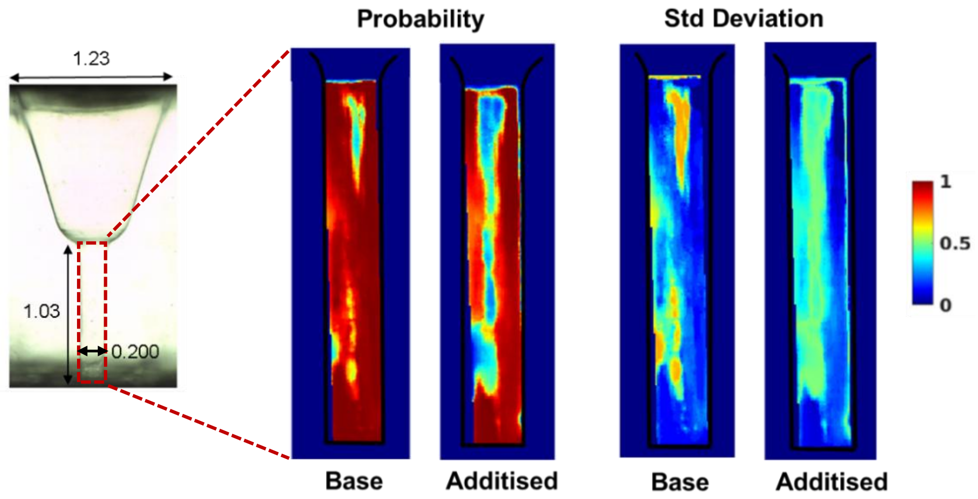

Figure 4.1: Vapour presence probability and respective standard deviation within the straight Spray C injector. Contour plots correspond to base fuel and ambient pressure of 5 bar. The black line indicates the outline of the injector-hole straight part. Cavitation does not appear in the sac region for the Spray C injector. All dimensions in the schematic are in mm.

Based on the binarised images, the vapour projected area has been measured for each frame and its distribution with time for the entire injection event is plotted in Figure 4.2. The three panels of Figure 4.2 correspond to increasing values of back pressure and, thus, decreasing CN values. Similar trends can be observed in all graphs, with the base sample exhibiting the highest projected area values and the biodiesel samples the lowest ones, respectively. The underlying cause should be sought in the difference in thermophysical properties, namely viscosity and saturation pressure, subsequently modifying the Reynolds number and CN. It is interesting to notice that the additised sample consistently exhibits lower cavitation projected-area values than the reference diesel, although their thermodynamic and transport properties are identical for the specific concentration of polymeric additive. The discrepancy, in this case, must be attributed to fuel rheology. As discussed in previous studies, the polymeric additives form flexible micelles once diluted in the base fuel. These micelles interact with vortices at different length scales, i.e., coherent vortical motion and turbulence, eventually influencing the cavitation formation processes, yet in a manner dependent on the cavitation regime. Experiments in injector replicas utilising XPCI have shown that viscoelastic fuels exhibit smaller amounts of attached cavitation compared to Newtonian diesel samples. This conclusion seems to be confirmed in real injector devices as well.

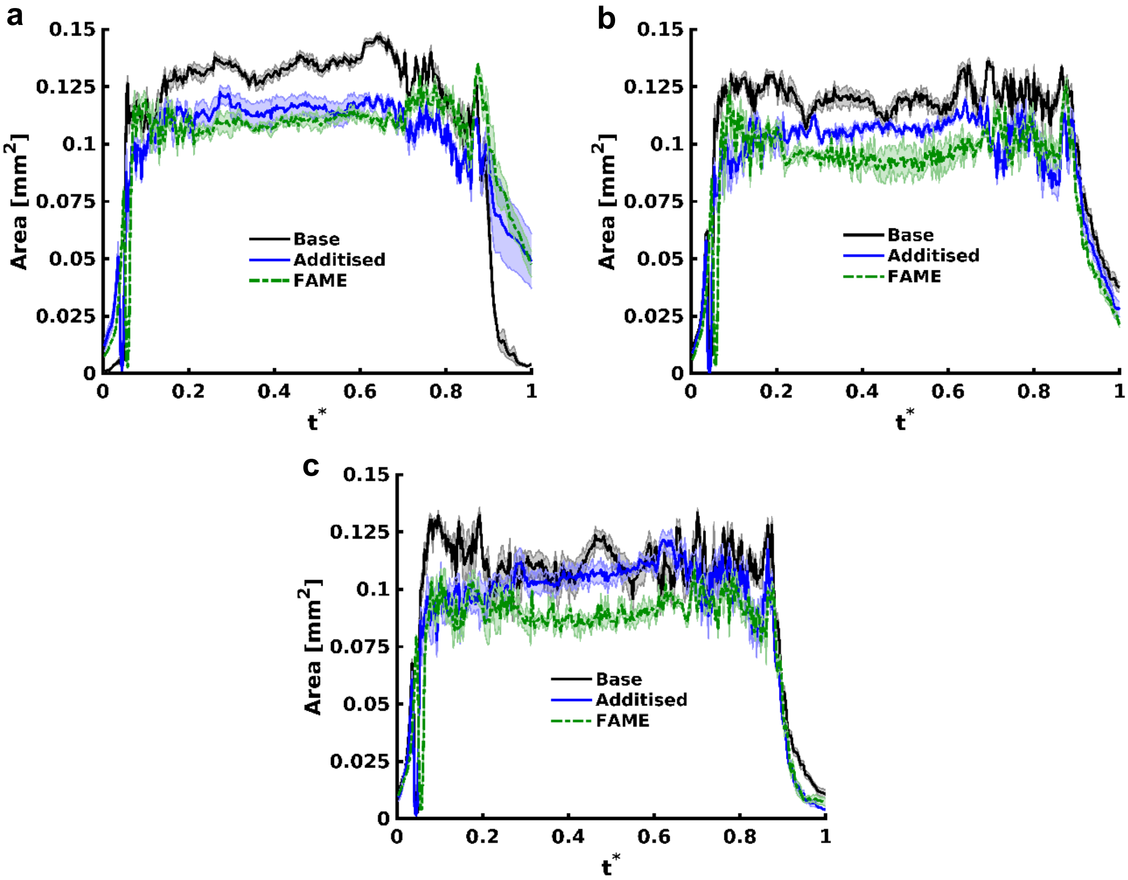

Figure 4.2: Distribution of the projected cavitation area with time in the Spray C injector for ambient pressures of (a) 1 bar, (b) 5 bar and (c) 20 bar. The duration of the injection event in absolute values is 311 ms. The shade of the same colour encompassing each graph line corresponds to standard statistical error.

Figure 4.4 depicts the distribution of spray cone angle with time for Spray C in a comparative manner for the three fuel samples examined. In general, increasing back-pressure leads to higher cone angles, owing to aerodynamic effects, i.e., drag forces, which become prevalent for 20 bar ambient pressure. On average, the biodiesel sample exhibits the lowest cone-angle values compared to the other two samples, which is expected due to its increased viscosity. It is interesting to notice that the additised sample exhibits considerably higher peak values than the base diesel in all examined cases. The micro-schlieren technique implemented has demonstrated that the increased cone angle is associated with the presence of longitudinal vortices within the injector hole, which gives rise to elongated cavities as well. Moreover, it is known that a prevalent effect of viscoelasticity on wall-bounded flows is turbulence suppression. Turbulence, or in other words, small-scale eddies, leads to the decay of large-scale vortices due to viscous damping. Hence, reduced turbulence favours the prevalence of elongated vortices, a postulation in agreement with the experimental results for the additised sample.

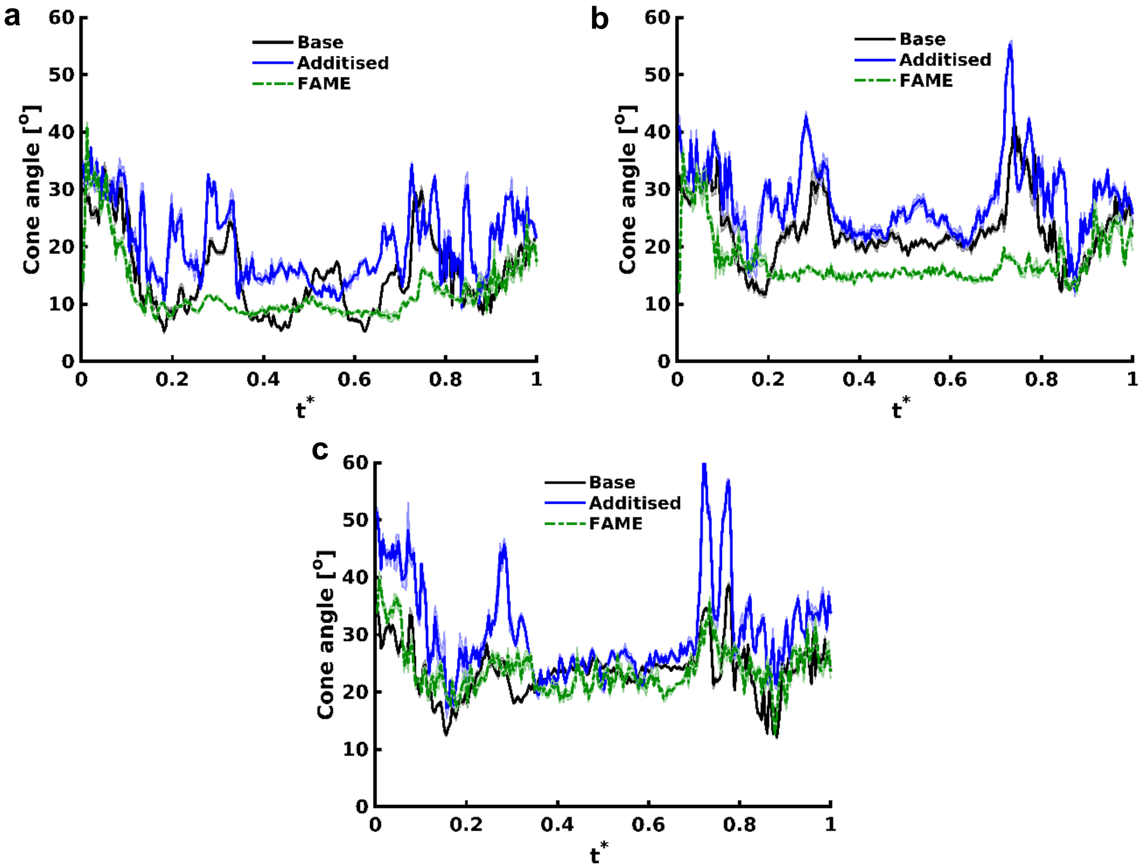

Figure 4.3: Distribution of the spray cone angle with time for the Spray C injector and ambient pressures of (a) 1 bar, (b) 5 bar and (c) 20 bar.

4.2.2. Spray D Results

This section presents and discusses the results for the Spray D injector nozzle, similar to the analysis performed for the Spray C injector nozzle. The focus remains on the post-processing of high-speed images captured throughout the injection event. The probability of vapour presence and the associated standard deviation were calculated using these images. The tapered layout of the injector-hole design in Spray D led to reduced cavitation compared to Spray C. This difference can be observed in Figure 4.4, which illustrates the experimental results for the Spray D injector nozzle. Due to the tapered geometry, the fluid flow experiences a smoother transition, which mitigates the formation of cavitation within the nozzle. Static attached cavities can be seen in the entrance region, whereas transient cavities emerge towards the orifice outlet, as confirmed by the relatively high standard deviation values, stemming mainly from machining imperfections [103]. The major part of the injector hole is occupied by pure liquid, while cavitation is completely absent from the sac region as well.

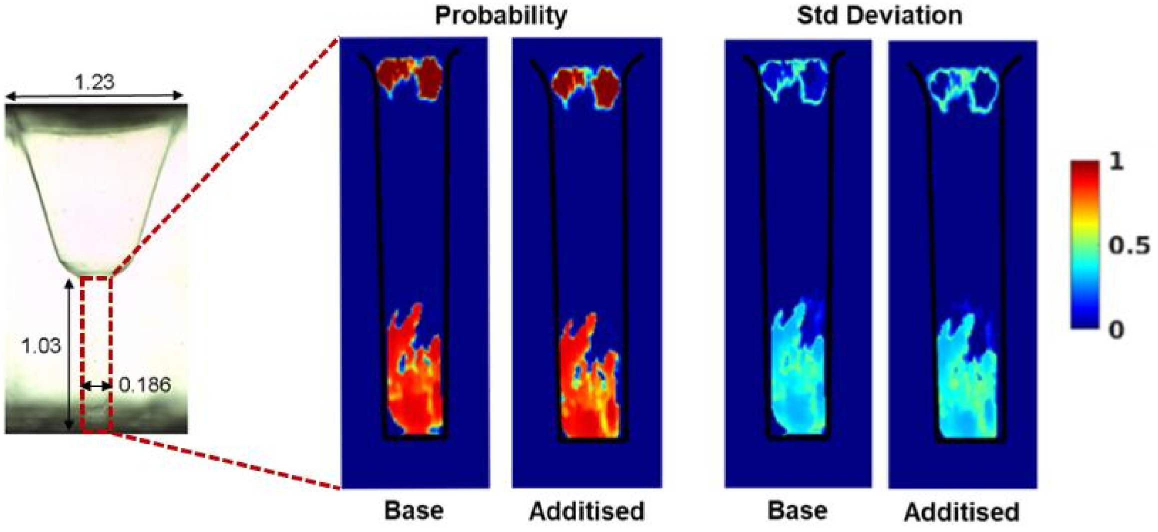

Figure 4.4: Vapour presence probability and respective standardisation within the tapered Spray D injector. Contour plots correspond to base fuel and ambient pressure of 5 bar. The black line indicates the outline of the injector-hole straight part. Cavitation does not appear in the sac region for the Spray D injector.

In a similar manner to Figure 4.2, Figure 4.5 presents the same distribution, yet for the Spray D tip and ambient conditions of 5 and 20 bar. The injection pressure is maintained at 900 bar. Once again, regardless of the ambient pressure, the biodiesel sample exhibits the lowest projected-area values. Besides, it is interesting to notice that the additised sample shows a non-consistent trend compared to the reference fuel. For the 5 bar ambient pressure case (Figure 4.5a), the two fuels have nearly identical distributions, yet with the viscoelastic fuel exhibits slightly lower projected area values. The trend is reversed for a 20 bar ambient (Figure 4.5b, where CN actually decreases). A plausible underlying cause is discussed in relevance to Figure 4.5, although the relevant differences are admittedly on the verge of experimental uncertainty.

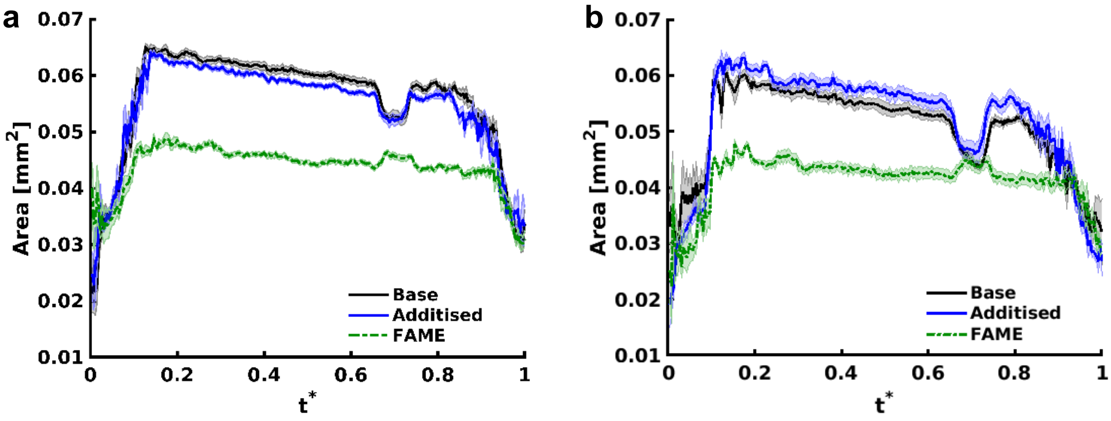

Figure 4.5: Distribution of the projected cavitation area with time for the Spray D injector and ambient pressures of (a) 5 bar, (b) 20 bar. The duration of the injection event in absolute values is 267 ms.

Figure 4.6a depicts the averaged presence probability of refractive index gradients corresponding to vortical structures within the nozzle throughout the duration of the injection event, as well as the respective standard deviation. Schlieren imaging was made possible in the mildly cavitating Spray D injector, where optical access to the nozzle could be attained. The probability contours plots illustrate the highly transient nature of the longitudinal vortices, as the maximum probability is of the order of 10%. The standard-deviation plot indicates that structures forming in the sac region and in the vicinity of the needle tip, are subsequently entrained in the injector hole. Figure 4.5b quantifies the temporally averaged projected area of vortical structures for different ambient conditions and fuel samples. The biodiesel fuel exhibits the lowest values due to enhanced viscous damping of the structures. Besides, the additised sample obtains a comparable averaged value to the base diesel for 5 bar ambient pressure case, yet it retains this value, despite the increase of the ambient pressure, unlike the reference counterpart. This behaviour is indicative of the enhancement of longitudinal vortices under the presence of viscoelastic additives, with subsequent after-effects in vortical cavitation, as shown in Figure 4.6b, and is in agreement with past studies [54],[141]. Raw schlieren image illustrating the vortical cavities are presented in Figure 4.6c, where the vortical structures are highlighted with red circles.

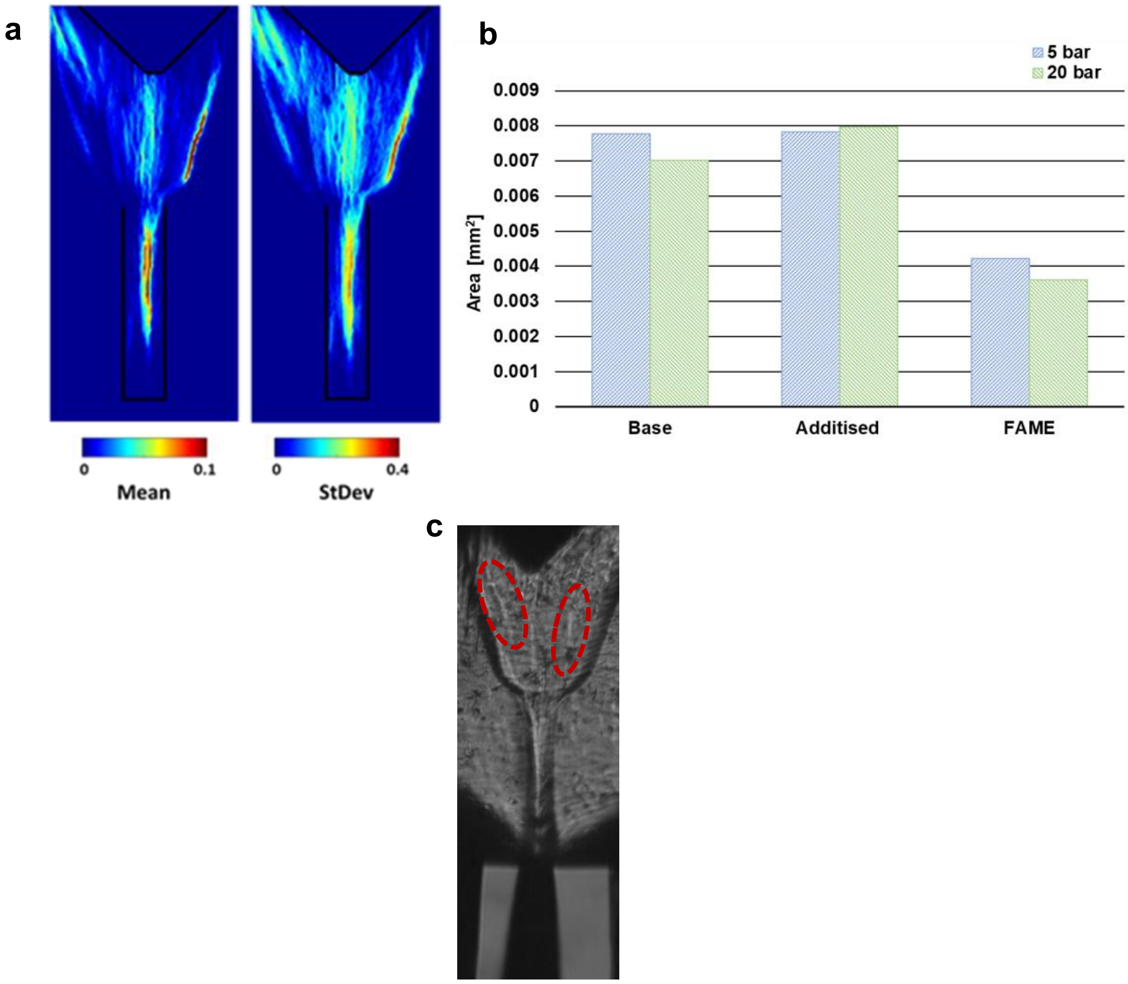

Figure 4.6: (a) Contour plots of vortical-structures mean presence probability and standard deviation in the Spray D injector (base fuel, 900/5 bar); **(b)** Temporally averaged projected area of vortical structures for different ambient conditions. **(c)** Raw schlieren image illustrating the vortical cavities.

The distribution of spray cone angle with time for Spray D is shown in Figure 4.7. As can be seen, no appreciable differences can be detected between the base and additised samples due to the less-perturbed flow prevailing within the injector nozzle. The biodiesel sample follows a behaviour similar to the Spray C nozzle, with lower values than the two other samples (Figure 4.7a) for the 5 bar ambient and relatively comparable values, denoting the primary influence of drag forces for ambient pressure of 20 bar.

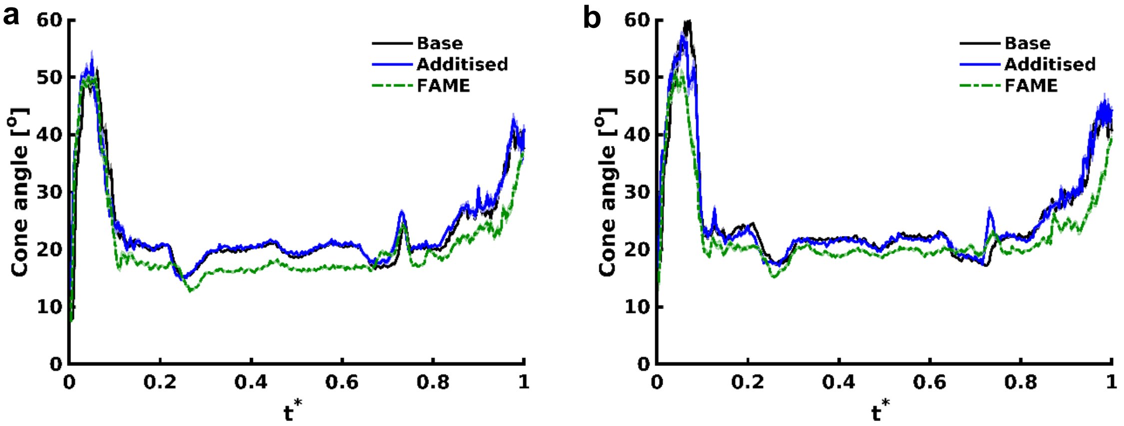

Figure 4.7: Distribution of the spray cone angle with time in the Spray D injector for ambient pressures of **(a)** 5 bar, **(b)** 20 bar.

4.2.3. Spray M Results

Spray M experiments were carried out at ambient pressures of 5 bar and 20 bar with an injection pressure of 500 bar. An indicative sequence of raw images is presented in Figure 4.8, capturing the intermittent formation of cloud and vortical cavities within the nozzle. Their automated classification, based on the combined eccentricity-and-location algorithm, is presented in Figure 3.11, following the approach outlined in the Methodology (section 3.4), providing a clear distinction between geometric and vortical cavitation structures. Similar to single-hole nozzles, vapour presence probability and standard deviation within the Spray M injector were obtained by averaging the post-processed images throughout the injection event. Indicative contour plots for the visualised nozzle hole and base fuel are presented in Figure 4.9. Maximum probability is of the order of 5% (Figure 4.9a), which is illustrative of the highly transient cavitation evolution in the specific layout, as also demonstrated by the high-standard deviation values prevailing throughout the orifice length (Figure 4.9b). It can also be discerned from the plots of Figure 4.9 that the high vapour-probability regions are located in the orifice core and have an elongated shape characteristic of cavities manifesting due to the presence of longitudinal vortices.

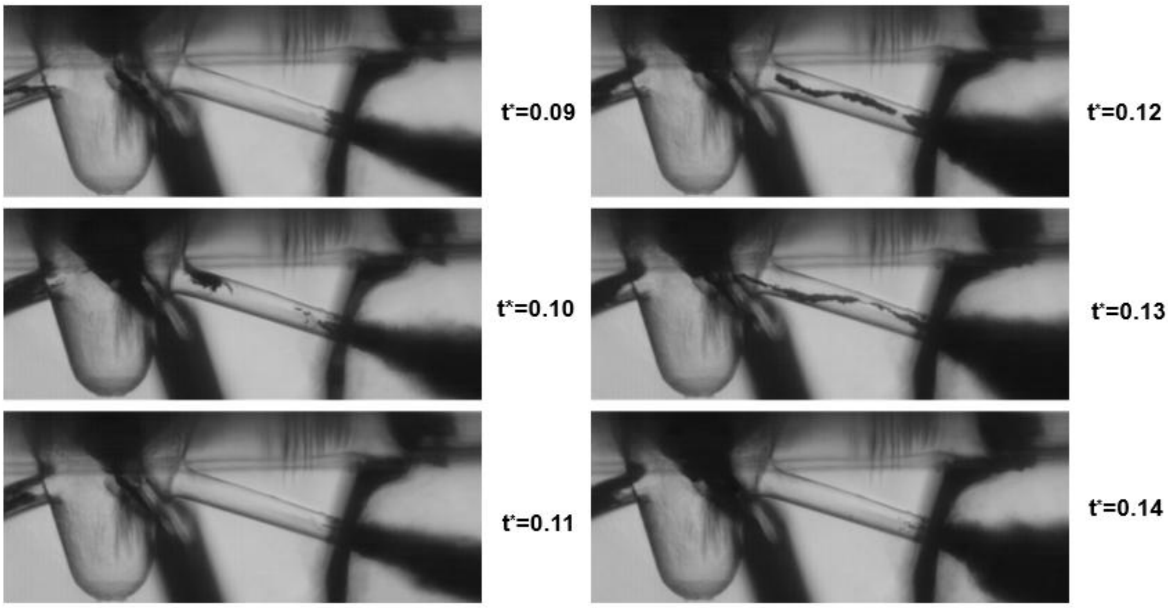

Figure 4.8: An indicative sequence of raw images for the Spray M injector. Cavitation is manifested primarily in the form of transient structures; hence the images were selected in such a manner to capture the formation of cloud and vortical cavities.

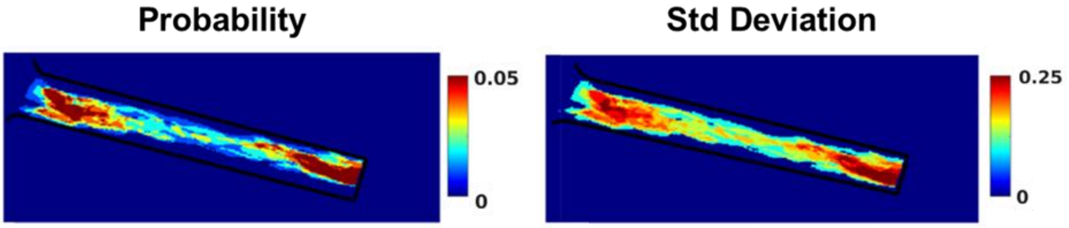

Figure 4.9: Vapour presence probability and respective standard deviation within the multi-hole Spray M injector. Contour plots correspond to base fuel and ambient pressure of 5 bar. The black line corresponds to the outline of the 'active' injector-hole for visualisation.

Figure 4.10 illustrates the distribution of spray cone angle over time for Spray M. The anticipated trend of increasing time-averaged cone angle with ambient pressure is confirmed once again; for example, the base sample shows an increase from 43.8° to 52.5°. Additionally, the biodiesel sample displays an average cone angle smaller than those of the base and additised samples, measuring 34° and approximately 45° at 5 and 20 bar pressures, respectively. The influence of vortical cavitation is highlighted by the fluctuating cone angle even between $t^* = 0.2$ and 0.8, during which the needle valve has reached its maximum position and remains stationary. Distinct peaks appear in the distributions for both 5 bar (Figure 4.10a, between $t^*=0.2$ and 0.4) and 20 bar ambient pressures (Figure 4.10b, between $t^*=0.2$ and 0.6), which are linked to the manifestation of coherent vortical cavities within the injector hole that persist all the way to the outlet, as also observed in [103]. Overall, the additised sample exhibits the highest average cone-angle values, equal to 47.5° and approximately 55.5° for the low- and high-pressure environments, respectively, a trend that may also indicate enhanced vortex coherence near the injector outlet.

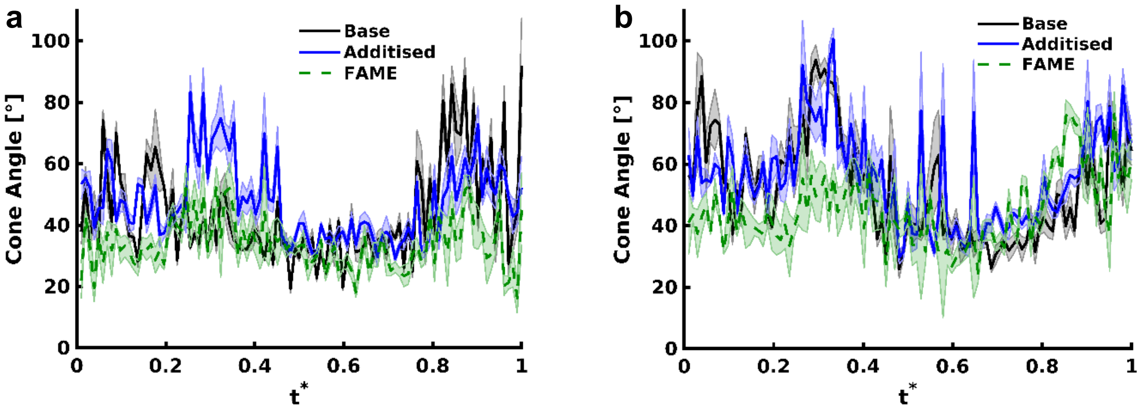

Figure 4.10: Distribution of the spray cone angle with time in the Spray M injector for ambient pressures of **(a)** 5 bar and **(b)** 20 bar.

Figure 4.11 presents the total cavitation projected area within the Spray M nozzle for the two ambient pressures examined. The bar charts in Figure 4.11 were generated by integrating the projected area of vapour structures detected throughout the injection event. As expected, the projected area decreases with increasing ambient pressure; the biodiesel sample shows smaller values. These observations are connected to the non-dimensional numbers characterising the flow conditions; for example, increased ambient pressure decreases CN, while higher viscosity reduces the Reynolds number, both of which result in reduced cavitation. It is also important to note that the additised sample exhibits a smaller extent of in-nozzle cavitation compared to base diesel at both ambient pressures.

To explain this trend, firstly, it should be clarified that in previous work by the authors' group, conducted on enlarged diesel-injector replicas, it was found that longitudinal cavities gained coherence due to viscoelasticity [142],[143],[144]. The proposed mechanism suggested that the reduction in the overall turbulence level, a well-established effect of viscoelastic additives, also reduces viscous damping. However, in the current experiments, string-like vortices do not exhibit stable behaviour and have lifetimes of only a few μs, also due to flow instabilities induced by the transient needle motion. In other words, the main findings of the current study should be compared to those regarding petrol injection in realistic optical devices with transient needle motion, as reported in [145], where the manifestation of transient vortical cavities is also suppressed in additised gasoline samples.

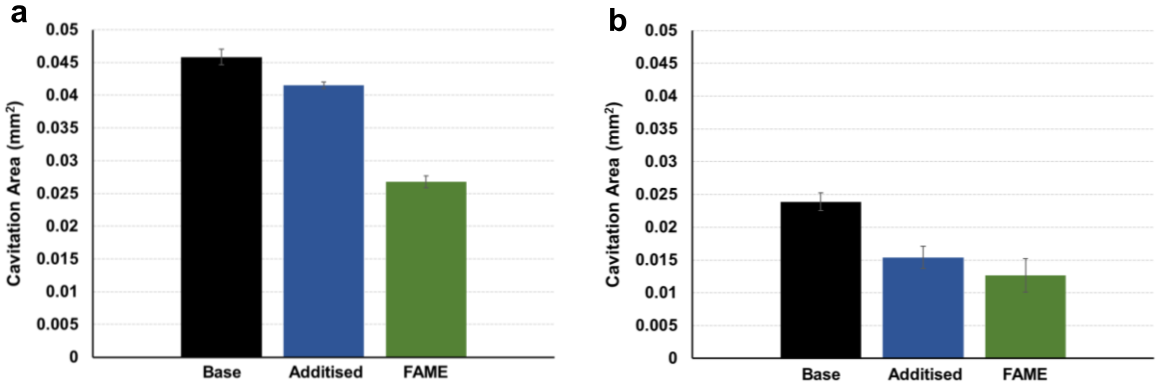

Figure 4.11: Total cavitation projected area in the visualised injector hole of Spray M for ambient pressures of **(a)** 5 and **(b)** 20 bar. Area has been integrated over the entire injection duration.

Figure 4.12 illustrates the number of individual elongated structures detected throughout the injection process for the examined fuels, based on the established post-processing criteria. The observed trends seem to support the previously established conclusions. For both ambient pressures, fewer string cavities emerge in the injector hole for the additised sample, with the difference compared to the base fuel being more substantial at the 20 bar ambient pressure (Figure 4.12b), where CN is also reduced. In other words, reduced flow turbulence as an effect of additive action leads to less extensive vortex roll-up and thus less cavitation formation. It is interesting to note that the decreasing trend in the absolute number of strings correlates with that of the overall projected cavitation area in Figure 4.11, providing additional evidence that vortical cavitation is the prevailing regime in the Spray M layout. The smallest numbers of string cavities during injection are observed for the biodiesel sample. This is once again an expected result due to its thermophysical properties, which nevertheless serve as further evidence for the validity of the post-processing method.

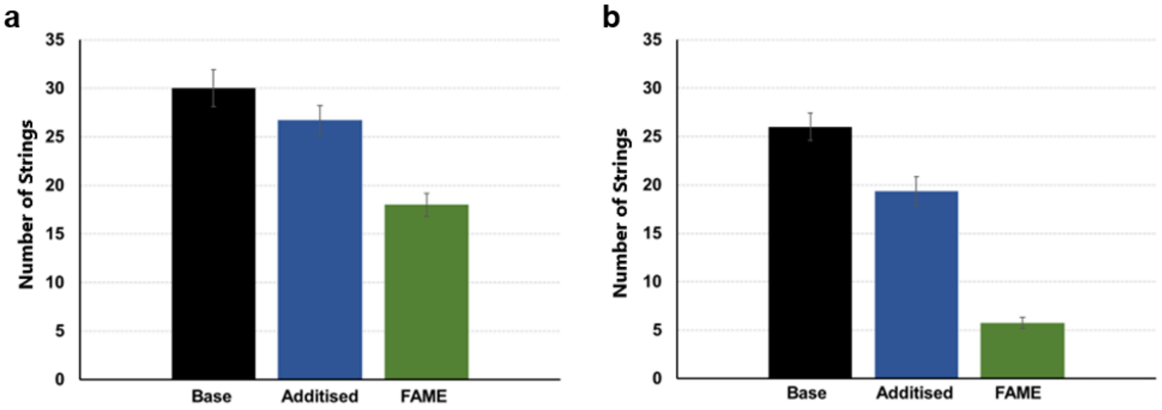

Figure 4.12: Number of discrete vortical cavities detected over the injection event in the Spray-M injector hole at **(a)** 5 and **(b)** 20 bar ambient pressures.

4.2.4. Conclusions

Diffuse-backlight illumination and micro-schlieren high-speed imaging were used to reveal secondary-flow and cavitation patterns within the internal flow path of single-hole and multi-hole transparent diesel injectors, as well as the near-nozzle spray dynamics. The focus was on viscoelastic effects induced by QAS additives diluted in base diesel, compared to visualisations obtained with Newtonian standard diesel and biodiesel fuels (FAME). The comparative assessment demonstrated that the sample treated with viscoelastic additives exhibited a reduced extent of geometrical, wall-attached cavitation compared to the base diesel in the heavily cavitating straight-orifice design, despite identical physical properties.

Consistent with previous findings from enlarged nozzle replicas, it was shown that viscoelasticity tends to suppress flow instabilities, i.e., turbulence, within the injector hole. Well-established, steady vortices, as observed in single-hole injectors, were enhanced by this effect. In contrast, the occurrence of highly transient vortices and, consequently, cavities in the multi-hole Spray M injector were hindered. Regarding spray topology, the additised sample consistently exhibited larger cone angles than base diesel under well-established cavitation conditions, likely due to the enhancement of vortical cavitation, as shown in the schlieren visualisation. The biodiesel sample displayed the smallest in-nozzle cavitation extent and the smallest spray divergence across all injector configurations, owing to its higher viscosity and saturation pressure compared to the other two samples.

The key takeaway is that fuel treatment with additives designed to induce a weakly viscoelastic nature can enhance both injector performance and reliability by promoting in-nozzle vortical motion. This is closely linked to improved spray atomisation and the suppression of near-wall bubble formation, thereby preventing collapse that could lead to material erosion.

4.2.5. Critical Review

This section provides a critical reflection on the contribution of this study in relation to existing and emerging literature on in-nozzle flow and spray characterisation using additised and renewable diesel fuels. While previous studies have investigated diesel fuel using model or enlarged injector geometries, the influence of viscoelastic fuel behaviour in real-size nozzles remains largely unexplored. This work addresses that gap by evaluating three fuel types: a commercial base diesel, a QAS-treated diesel, and FAME biodiesel. The QAS additive induces viscoelasticity through the formation of flexible micelles that interact with vortical structures across different flow scales, ultimately affecting cavitation topology.

Earlier experimental studies have shown that QAS-treated fuels can increase injector discharge coefficients and alter internal flow behaviour [54]. Advanced diagnostics such as high-flux X-ray phase contrast imaging and supporting numerical models have confirmed that these additives tend to suppress attached cavitation while promoting longitudinal vortices, due to reduced turbulence and enhanced flow coherence [78],[146]. However, such studies were typically limited to single-orifice replica injectors. The present study builds on this foundation by employing ECN-standard, real-size transparent nozzles (Spray C, Spray D, and the multi-hole Spray M) and high-speed imaging to simultaneously examine in-nozzle cavitation and near-nozzle spray development. Results demonstrate that QAS-treated diesel reduces the extent of attached cavitation and enhances longitudinal vortices, leading to increased spray cone angles. These findings not only validate previous conclusions on turbulence suppression [78] but also introduce new insights into the link between rheological modification and spray morphology in practical injector configurations.

Overall, this part of the research provides original experimental evidence on how QAS-induced viscoelasticity influences in-nozzle cavitation and spray development in real-size diesel injectors. By using standardised geometries and realistic conditions, it fills a key gap in the literature. The findings highlight the potential of QAS additives to improve spray behaviour and flow stability, offering a practical strategy for enhancing combustion efficiency and injector durability, particularly for renewable fuels with less favourable rheological properties and in applications where electrification remains unfeasible.

4.3. Assessing Cavitation topology and Spray Formation of SAFs

SAF behaviour was evaluated employing the Spray C and D single-hole injectors already described. The fuel was subjected to pressure generated by a high-capacity syringe pump, with the injection pressure set to 500 bar for Spray C and 700 bar for Spray D. The injection pressure for Spray D was limited to 700 bar after initial tests to avoid damaging the acrylic components. This approach allowed for the evaluation of at least four distinct injection events per fuel type across three different pulse durations. In contrast, the injection pressure for the Spray C injector was limited by visualisation constraints since for the injection pressures above 500 bar, the injector hole was rendered completely opaque throughout the injection process for some of the investigated fuels.

The injector needle-lift profile was controlled using signals with durations of 0.65, 0.95, and 1.25 milliseconds, provided by an electronic driver, with the same injector needle profile imposed for each duration. Spray D injection at 700 bar, resulting in injection durations of 1.175, 1.8, and 2.5 milliseconds, respectively, as shown in Table 4.2. Due to the influence of injection pressure on duration, Spray C injections at 500 bar resulted in injection durations of 1.125 and 2 milliseconds for imposed signal durations of 0.95 and 1.25 milliseconds, respectively. For Spray C, the imposed signal durations of 0.95 and 1.25 milliseconds achieved the desired injector lift profiles. However, a 0.65-millisecond signal duration at 500 bar was insufficient to initiate injection. The ambient pressures of 1 and 10 bar investigated, whilst maintaining a constant temperature of 20°C. Each experiment was repeated four times to provide statistical information and reduce uncertainty, without excessively repeating the experiments to avoid rupturing the acrylic piece and thus ensuring the completion of the entire experiment matrix. The details of the conducted experiments and the operating conditions are presented in Table 4.2. As the properties of fuels play a crucial role in influencing in-nozzle flow dynamics and the resulting spray formation, Table 3.1 provides a detailed overview of the properties of the fuels investigated.

Table 4.2: Injection Parameters and Ambient Conditions for Variable Pulse Duration Experiments

Injector layout	Spray C	Spray D
Injection Pressure [bar]	500	700
Injection Duration [ms]	1.125-2	1.175-1.8-2.5
Ambient gas	N_2	
Ambient temperature [K]	293	
Ambient pressure [bar]	1-10	
Ambient density [kg/m^3]	1.15-11.5	
Fuel	Diesel-Dodecane-Jet A-C4-BCH	

4.3.1. Spray C Results

In this section, the results for the Spray C injector nozzle are presented, focusing on the analysis of high-speed images captured during the injection event. The post-processing of high-speed images throughout the injection event facilitated the calculation of vapour presence probability and its associated standard deviation, as illustrated in Figure 4.13 for the Spray C injector. The straight configuration of the injector holes in Spray C results in significant cavitation, with the nozzle being predominantly filled with vapour throughout most of the injection process, as indicated by the mean probability values. It is important to understand that this does not necessarily mean the entire orifice volume is filled with vapour; rather, a peripheral layer envelops the wall, preventing light from penetrating further. The high standard deviation values in certain localised areas indicate the presence of transient cavities within the core region.

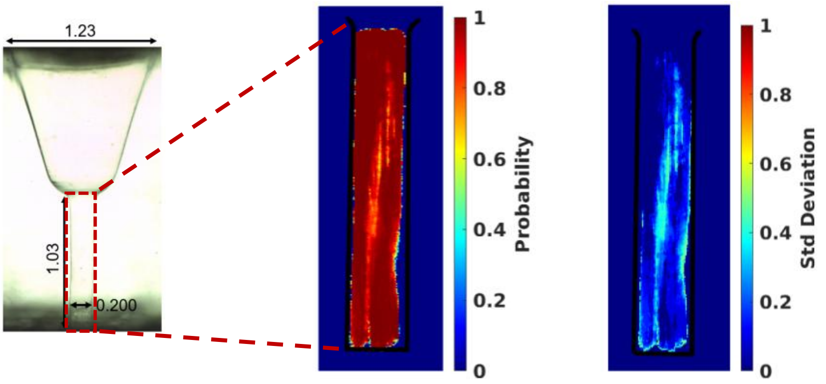

Figure 4.13: Vapour presence probability and respective standard deviation within the straight Spray C injector. Contour plots correspond to diesel fuel and ambient pressure of 500/10 bar. The black line indicates the outline of the injector-hole straight part. All dimensions in the schematic are in mm.

The vapour projected area was quantified for each frame using the binarised images, and its distribution over time for the entire injection event is depicted in Figure 4.1 for all test samples explored and an injection pulse duration of 1250 μs. The results depict well-expected trends, i.e., an increase in ambient pressure leads to reduced in-nozzle cavitation regardless of the fuel properties, thus, justifying the validity of the experiments. The trend between fuels does not change with different pulse durations, as discerned by juxtaposing Figure 4.14a and Figure 4.14b and Figure 4.14c and Figure 4.14d, and the effect of ambient pressure remains consistent across different pulse durations. It can be discerned that the projected vapour area remains relatively constant during the quasi-steady phase of the injection process ($0.2 < t^* < 0.8$), irrespective of the prevailing ambient conditions for the longer injection duration of 1250 μs. The needle lift varies with injection duration. Under analogue pressure conditions, longer durations generally increase the maximum needle lift, reducing throttling effects and stabilising the flow, allowing it to reach a steady state. In contrast, shorter injection durations result in lower needle lifts, potentially keeping the flow in a more transient state. Figure 4.16 presents additional high-speed images that highlight these transient features, providing a closer view of these dynamic changes.

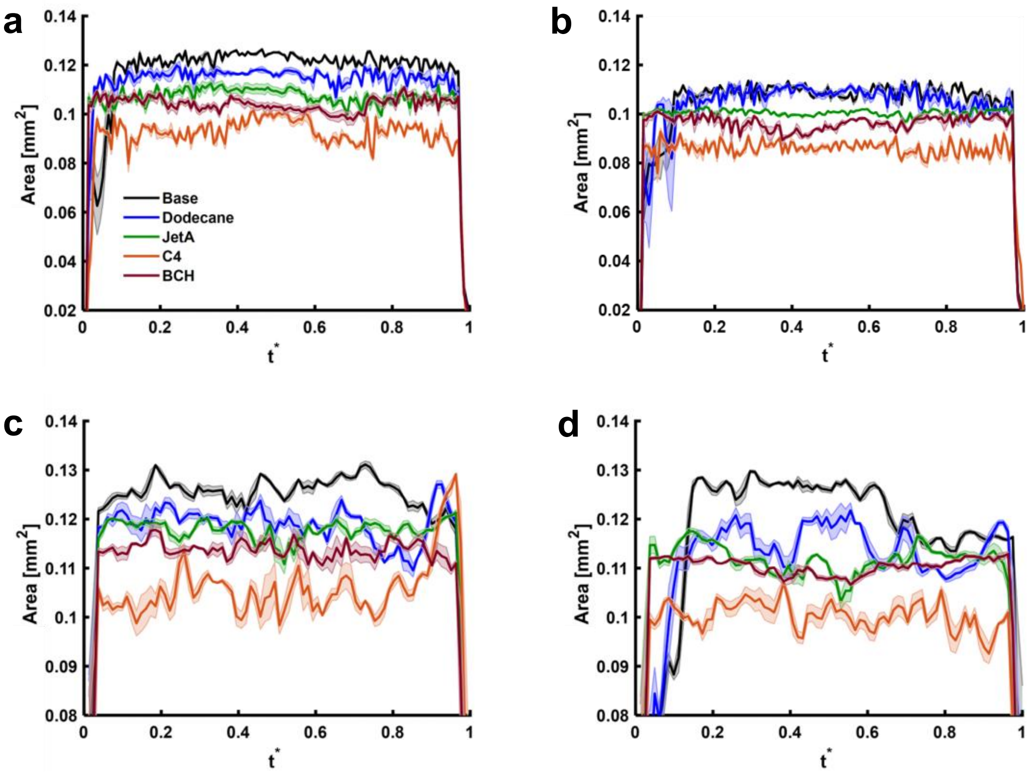

Figure 4.14: Distribution of vapour projected area with time for Spray C for different injection- pulse durations and ambient pressures of: (a) 1250 μs, 1 bar (b) 1250 μs, 10 bar, (c) 950 μs, 1 bar, (d) 950 μs, 10 bar. At each time point, the projected area corresponds to the total area of the structures identified in the binarised images. The shade of the same colour encompassing each graph line corresponds to standard statistical error. For graphs (c) and (d), a 3-point moving average was applied to smooth the data and improve clarity.

There is a direct link between the in-nozzle extent of cavitation and the near-field spray morphology and cone angle of the expelled spray. At 1 bar, as shown in Figure 4.15a, the spray cone angles for various fuels remain generally close to each other. Dodecane and diesel, in particular, demonstrate very similar behaviour, with both maintaining cone angles between 10 and 15 degrees, showing relatively minimal fluctuations throughout the injection period. Jet-A and C-4, however, show wider cone angles, peaking up to 25 degrees due to their higher evaporation rates and lower viscosities. BCH exhibits the highest variability, with cone angles ranging between 7 and 16 degrees. Similarly, at 10 bar, as depicted in Figure 4.15b, dodecane and diesel remain closely aligned, with cone angles still grouped around 10 to 15 degrees. However, the mean cone angles at 10 bar are slightly higher than those at 1 bar, due to the increase in backpressure and, therefore aerodynamic drag. Jet-A, C-4, and BCH exhibit more significant fluctuations, with cone angles regularly exceeding 20 degrees. It is important to emphasise that these observations are specific to the near-nozzle region, where spray morphology is more directly influenced by in-nozzle flow dynamics. These effects may not be as evident farther downstream, where additional aerodynamic and mixing processes shape the spray behaviour.

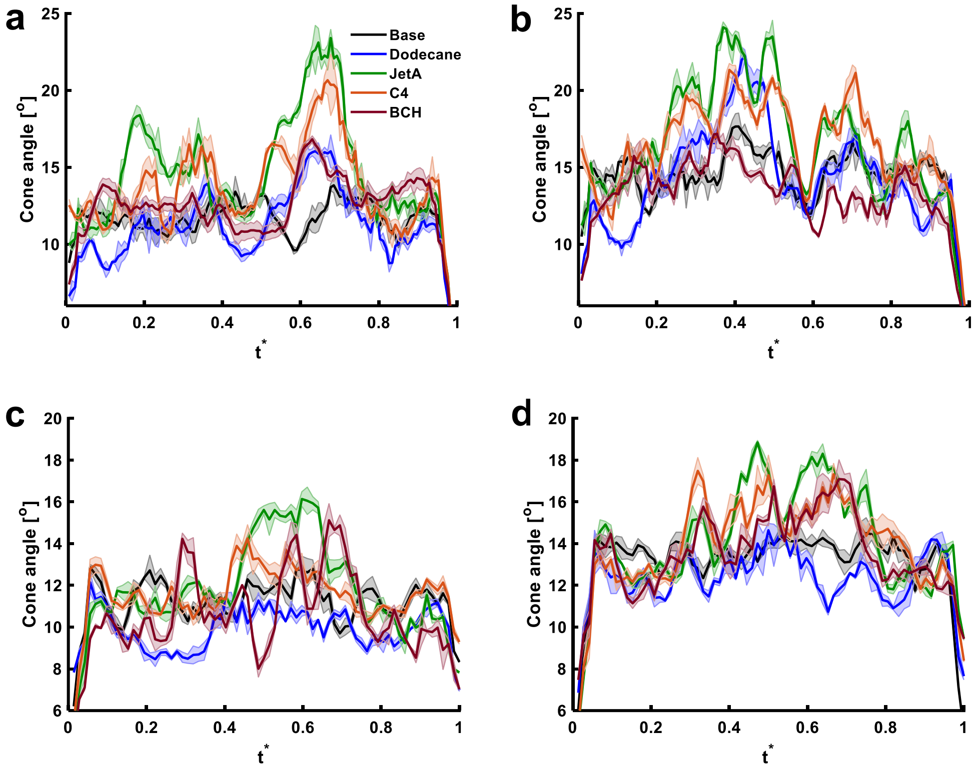

Figure 4.15: Distribution of the spray cone angle over time in Spray C for different injection- pulse durations and ambient pressures of: (a) 1250 µs, 1 bar 1250 µs, (b) 1250 µs, 10 bar, (c) 950 µs, 1 bar, (d) 950 µs, 10 bar. The shade of the same colour encompassing each graph line corresponds to standard statistical error. A 5-point moving average was applied to smooth the data and improve clarity.

Sequential images for Spray C with fuel C-4 are presented in Figure 4.16, under injection and ambient pressures of 500 bar and 1 bar, respectively, with a pulse duration of 950 μs, highlighting the distinct patterns observed in Figure 4.14 and Figure 4.15. As observed from the high-speed images, cavitation within the Spray C nozzle exhibits a multitude of transient features, apart from the wall-attached vapour layer already reported, which are reflected as fluctuations in the cavitating area (Figure 4.14c) and variations in spray angle values (Figure 4.15c) at the corresponding injection times. The shorter pulse duration of 950 μs enhances the fluctuating trend for C-4 fuel, leading to more pronounced variations in the cavitating area and greater variability in the spray angle.

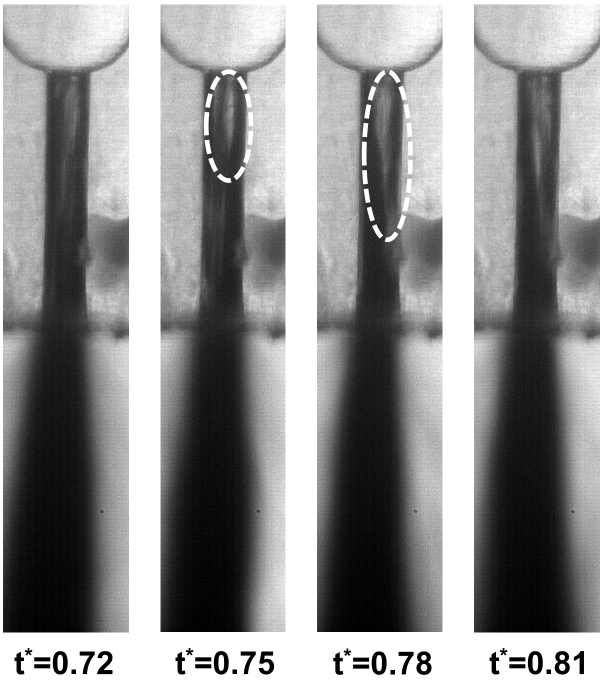

Figure 4.16: Sequential images depicting cavitation structures (highlighted by the white dash-line ovals) and spray behaviour for Spray C, with injection and ambient pressures of 500 bar and 1 bar, with a pulse duration of 950 μs, using C-4.

4.3.2. Spray D Results

This section presents the results for the Spray D injector nozzle, with a detailed analysis of high-speed images captured during the injection event. Post-processing of these images facilitated the calculation of vapour presence probability and its associated standard deviation, as illustrated in Figure 4.17. The figure presents contour plots of the same quantities as those in Figure 4.13 but for the Spray D injector. It is evident that vapour formation is suppressed in this device due to its tapered layout and hydro-grinded entrance. Transient cavities emerge towards the orifice outlet, as confirmed by the relatively high standard deviation values, which are primarily attributed to machining imperfections [103]. The majority of the injector hole is occupied by pure liquid, with cavitation being completely absent from the sac region.

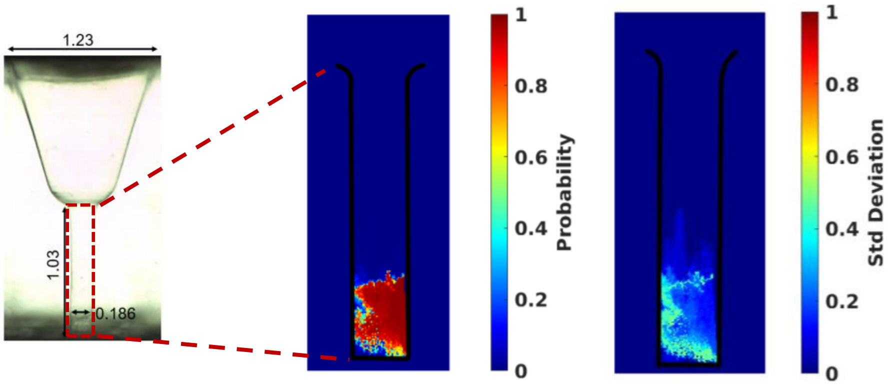

Figure 4.17: Vapour presence probability and respective standard deviation within the straight Spray D injector. Contour plots correspond to diesel fuel and ambient pressure of 10 bar. The black line indicates the outline of the injector-hole straight part. All dimensions in the schematic are in mm.

The vapour projected area was also quantified within the Spray D injector using binarised images, as shown in Figure 4.18. The data shows that increasing ambient pressure reduces cavitation across all fuels as also observed in Spray C. The trends remain unchanged for different pulse durations, as in Figure 4.18c and Figure 4.18d) and the projected vapour area is stable during the quasi-steady phase ($0.2 < t^* < 0.8$), regardless of ambient conditions. The fuel behaviour mirrors Spray C, except for BCH. For Spray D, BCH exhibits the highest cavitation area, showing more fluctuations than other fuels. The cavitation area increases significantly during the needle opening and closing phases for all fuels, but this effect is more intense for BCH, which is attributed to its higher viscosity [147], as further demonstrated by the spray cone angle graphs presented shortly thereafter (refer to Figure 4.21).

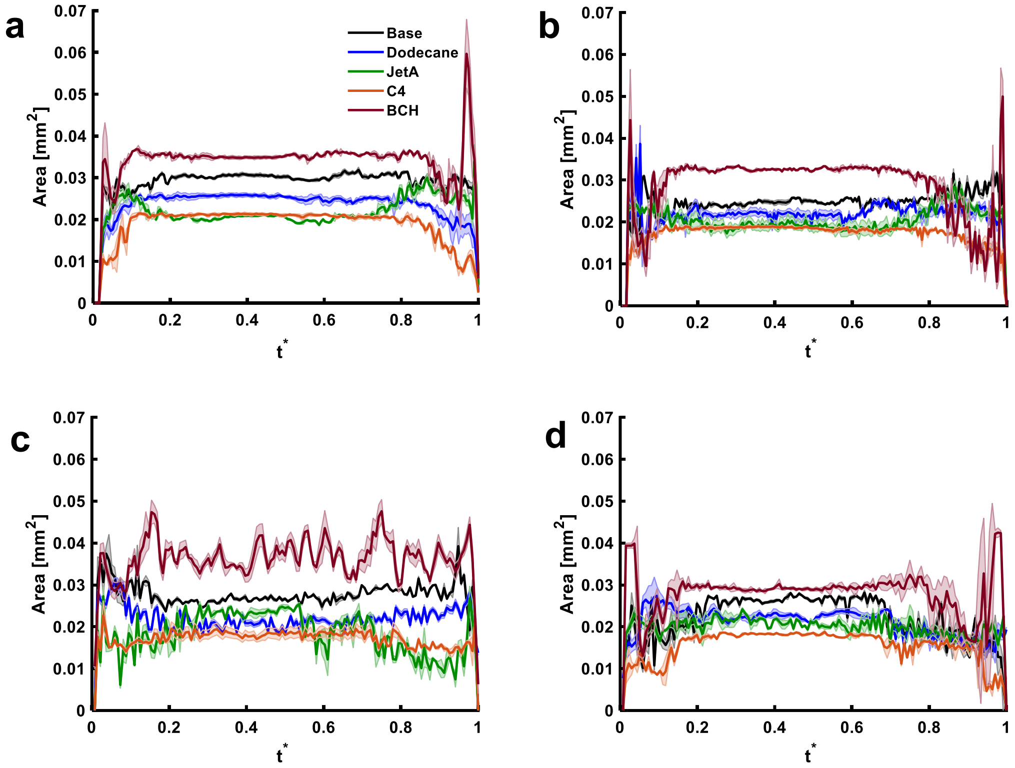

Figure 4.18: Distribution of vapour projected area with time for Spray D for different injection- pulse durations and ambient pressures of: (a) 1250 μs, 1 bar 1250 μs, (b) 1250 μs, 10 bar, (c) 950 μs, 1 bar, (d) 950 μs, 10 bar.

Sequential images for Spray C with fuel C-4 are presented in Figure 4.19, under injection and ambient pressures of 500 bar and 1 bar, respectively, with a pulse duration of 950 μs, highlighting the distinct patterns observed in Figure 4.14 and Figure 4.18. As observed from the high-speed images, cavitation within the Spray C nozzle exhibits a multitude of transient features, apart from the wall-attached vapour layer already reported, which are reflected as fluctuations in the cavitating area (Figure 4.14c) and variations in spray angle values (Figure 4.18c) at the corresponding injection times. The shorter pulse duration of 950 μs enhances the fluctuating trend for C-4 fuel, leading to more pronounced variations in the cavitating area and greater variability in the spray angle.

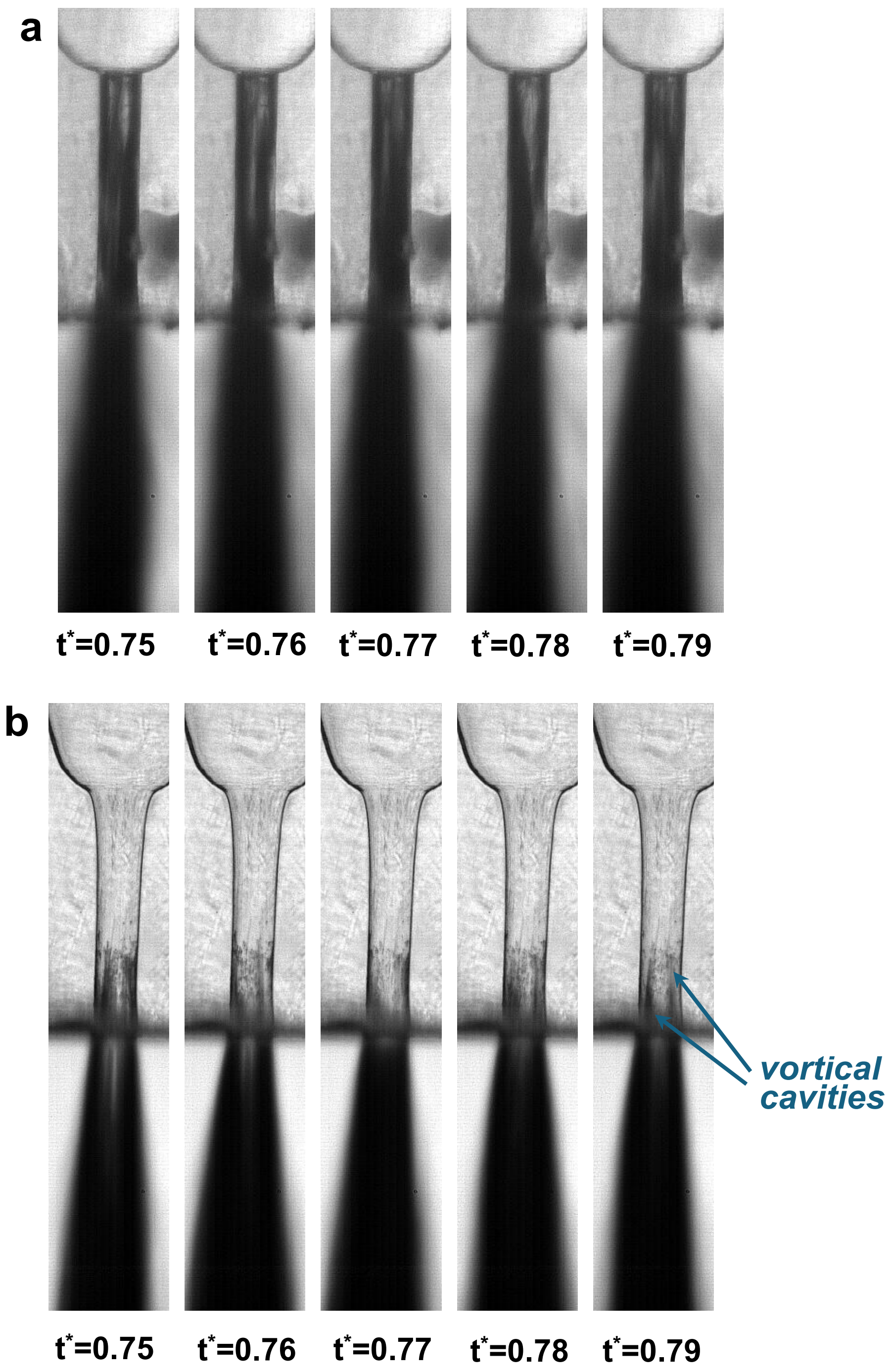

Figure 4.19: Sequential images depicting cavitation structure and spray behaviour for: (a) Spray C, with injection and ambient pressures of 500 bar and 1 bar, respectively, and (b) Spray D, with injection and ambient pressures of 700 bar and 1 bar, respectively. Both cases feature a pulse duration of 950 µs, using C-4.

Figure 4.20 illustrates the distribution of the projected area over time for varying injection durations in Spray D at an ambient pressure of 1 bar for both diesel and Jet-A fuels. As the pulse duration decreases, both the cavitating area and fluctuations increase. However, this variation cannot be discerned for Spray C, as demonstrated in Figure 4.14. This is expected because vortical cavitation is less pronounced in Spray C as geometric cavitation occupies most of the nozzle.

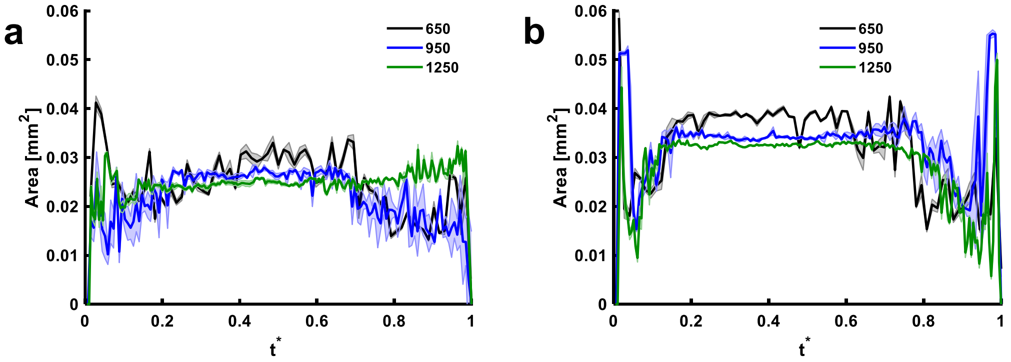

Figure 4.20: The distribution of the projected area with time for varying injection durations in Spray D at 10 Bar ambient pressure for fuels: (a) Diesel, (b) BCH.

Figure 4.21a and Figure 4.21b present the relationship between spray cone angle and normalised injection time (t^*) for various fuels. Four of the fuels, dodecane, diesel, Jet-A, and C-4, show similar mean values that are relatively close to one another, although BCH stands out with significantly higher mean cone angles. Diesel and dodecane display similar behaviour, with dodecane consistently maintaining a relatively stable and low cone angle throughout the injection process. Diesel, however, shows slightly higher cone angles at both the start and end of the injection process, which can be attributed to its higher cavitation potential, consistent with the behaviour observed in Spray C, as shown in Figure 4.18. Jet-A and C-4 display wider and more variable spray cone angles throughout the injection period compared to diesel and dodecane. Jet-A, in particular, demonstrates a broader spray cone angle than diesel, which is consistent with findings in the literature [148], largely due to Jetssho-A's higher evaporation rate and lower viscosity. The similarity observed between C-4, and Jet-A can be primarily attributed to their similar vapour pressures, with their overall fuel properties being closely related, as evidenced by the occurrence of peaks at siDistribution of vapour projected area with time for Spray D for different injection pulse durations and ambient pressures of milar points during the injection.

In contrast, BCH exhibits the greatest variability among the fuels tested, with cone angles consistently exceeding 15 degrees and often reaching up to 30 degrees. This pronounced variability is attributed to BCH's higher viscosity, leading to a greater cavitation tendency reflected in its larger projected cavitation area throughout the injection process. This correlation between high viscosity and increased cavitation in BCH aligns with findings from previous studies. Nouri et al. [149] investigated the effect of viscosity on vortical cavitation in a single-piston ring assembly. They observed that higher viscosity strongly promotes the formation and elongation of string cavities, as it helps preserve the coherent vortex structures. In contrast, lower viscosity accelerates string breakup, causing cavitation length to decrease by up to 35%. Similarly, Li et al. [150] stated that the cavitation area increases for high-viscosity lubricants, while lower viscosity leads to smaller cavitation areas and improved lubrication quality as the internal friction decreases and the lubricant flows more rapidly.

Figure 4.21c and Figure 4.21d extend the analysis to a shorter injection pulse duration of 950 µs. The trends among the fuels remain largely consistent with those previously discussed; however, the shorter injection duration introduces more pronounced transient effects, resulting in increased average cone angles as the injection becomes more transient, as expected. This increase is anticipated due to the enhanced influence of unsteady flow dynamics associated with rapid needle movements during shorter injections. While the overall spray patterns are similar to those at 1250 µs, the reduced duration leads to slightly higher cone angles and increased variability, particularly during the start and end of the injection process.

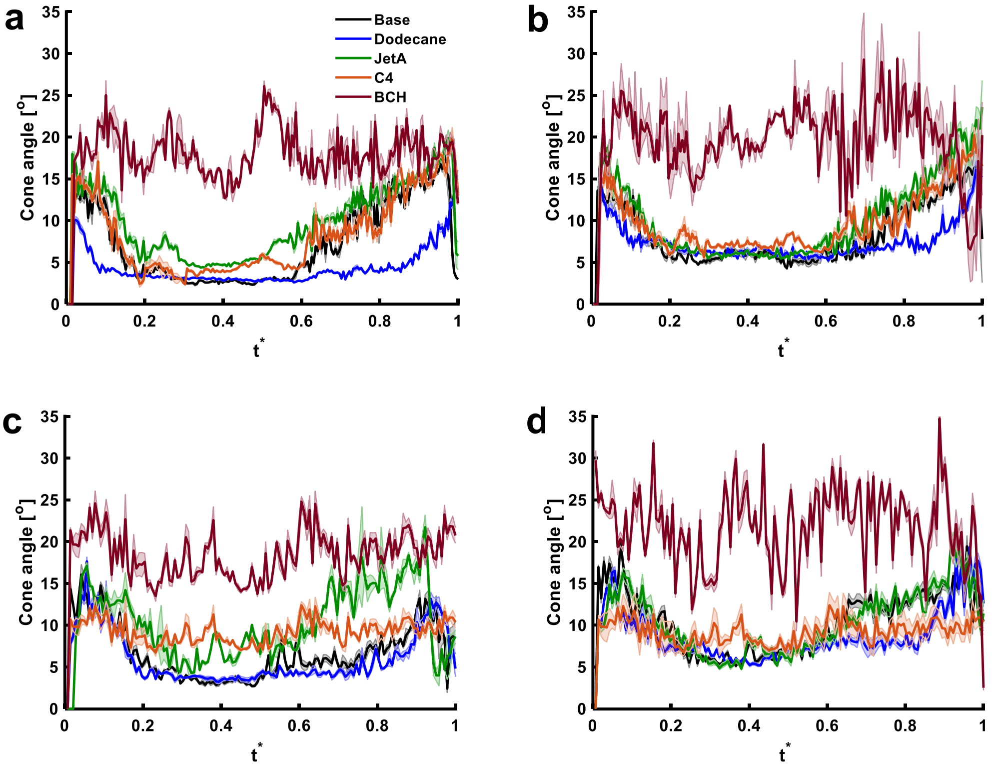

Figure 4.21: Distribution of the spray cone angle over time in Spray D angle for an injection pulse duration of 1250 µs at ambient pressures of (a) 1 bar, (b) 10 bar, (c) 950 µs, 1 bar, (d) 950 µs, 10 bar.

The cone angle displays consistent behaviour across both low and high ambient pressures, with an increase in backpressure correlating to a rise in the average cone angle, as observed in Spray C. Overall, results show a marked increase in cone angle at the start and end of injection for most fuels. Notably, Jet-A and C-4 remain close to each other and exhibit higher cone angles than dodecane and diesel. While diesel angle values occasionally approach those of C-4 near the start and end of the injection, C-4 generally surpasses diesel for most of the injection period. BCH stands out with the largest cone angles reflecting its highest cavitation projected area (refer to Figure 4.18), owing, to its high viscosity and the prevailing cavitation regime in the Spray D orifice, as explained above.

Although the Spray C and Spray D injectors share similar nominal dimensions, Spray D is a tapered orifice that is meant to suppress cavitation. Considering that vortical cavitation, especially if set in the vicinity of the injector outlet, has a critical influence on the spray cone angle [32],[151] compared to geometric cavitation [33],[152], the cone angle variations in the Spray D injector should be primarily attributed to this regime. In contrast, Spray C experiences both geometric and vortical cavitation, resulting in a greater overall extent. The difference in cavitation regime is postulated as the underlying cause leading to the counter-intuitive variations in spray-cone angle observed for BCH in the two injector outlets. Spray D suppresses geometrical cavitation due to its smooth, tapered orifice geometry, while vortical cavitation is still present near the exit. This contrasts with Spray C, in which both wall-attached and vortical cavitation co-exist and exhibit cavitation with all fuels, leading to consistently larger spray cone angles.

In a similar manner to Figure 4.20, as a way to illustrate the effect of pulse durations on specific fuels, Figure 4.22 presents comparative analyses of cone angles for diesel and BCH fuels at each pulse duration spanning from 650-1250 µs. As can be seen, a longer pulsation duration leads to stabler sprays in the quasi-steady injection period, $0.2 < t^* < 0.8$ for both fuels, with relatively small cone angles of around 7° for diesel and about 22° for BCH. By contrast, for a pulse duration of 650 µs, the spray topology becomes more fluctuating, and the cone angle reaches higher values during the steady-injection phase, up to 13.5° for diesel and 27° for BCH.

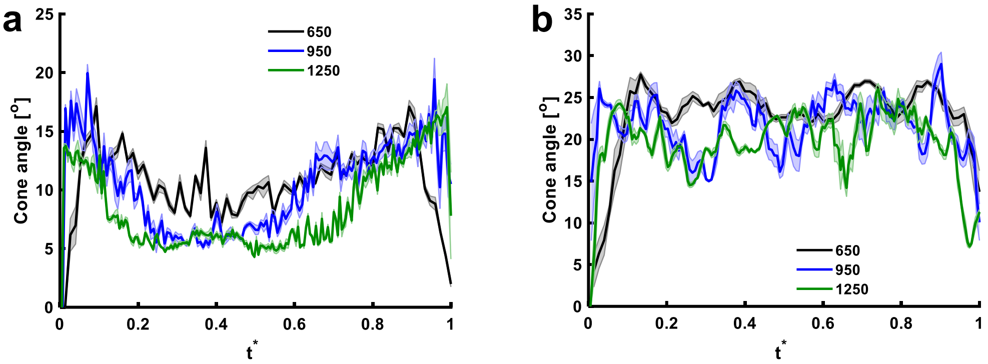

Figure 4.22: Spray D cone-angle distribution of (a) Diesel and (b) BCH for different pulse durations at ambient of 10 bar. For graph (b), a 3-point moving average was applied to smooth the data and improve clarity.

4.3.3. Conclusions

The in-nozzle flow dynamics and near-nozzle spray characteristics for five fuels, including conventional diesel, jet fuel (Jet-A), dodecane, and sustainable aviation fuels were analysed using high-speed DBI. Using two ECN nozzles, Spray C and Spray D, the evaluation examined fuel cavitation, spray characteristics, and transient effects under varying injection pulse durations. The comparative analysis revealed distinct cavitation and spray behaviours across the fuels, with BCH exhibiting particularly notable characteristics under Spray D conditions. Under Spray D, BCH showed the highest level of cavitation, primarily due to significant string cavitation, which is linked to its higher viscosity. The tapered shape of Spray D suppresses geometric cavitation but does not prevent string cavitation. Since vortical cavitation has a more significant impact on the spray cone angle than geometric cavitation, BCH fuel exhibits substantially higher cone angles in Spray D, supporting this observation. In contrast, Spray C, due to its straight design, does not suppress cavitation, resulting in high levels of geometric cavitation across all fuels. Consequently, BCH demonstrates only moderate cavitation in this configuration. This behaviour is further reflected in the spray cone angle measurements, where BCH shows the highest angles in Spray D but only average angles in Spray C compared to the other fuels.

The injection pulse duration also significantly impacted cavitation and spray dynamics. Shorter injection pulses led to more unsteady flows and intensified cavitation, causing greater fluctuations in the spray cone angle as the fuel struggled to stabilise. Longer injection pulses enabled higher needle lifts, stabilising the flow, reducing cavitation, and producing more consistent spray patterns. This highlights the importance of injection timing and needle dynamics in managing cavitation and optimising spray formation.

These insights are crucial for optimising fuel injection strategies, particularly for sustainable aviation fuels, to improve combustion efficiency and reduce emissions. This is the first experimental evaluation of the cavitation and spray behaviour of highly promising sustainable aviation fuels and provides a new database that will allow model validation and further research, ultimately supporting wider adoption for the decarbonisation of the aviation sector. Future research using multi-hole injectors, which may better differentiate between vortical and geometric cavitation, could yield a deeper understanding of BCH behaviour and contribute to the development of more efficient fuel systems.

4.3.4. Critical Review

This section provides a brief commentary on the literature that emerged following the submission of the article corresponding to this part of the Results chapter. It investigates in-nozzle flow and near-nozzle spray characteristics of fuels relevant to sustainable aviation, including Jet-A, diesel, two SAF candidates (BCH and C-4), and a surrogate (dodecane), under variable injection durations and two distinct nozzle geometries: a straight orifice (Spray C) and a converging orifice (Spray D).

Recent developments in SAF deployment in aero-engine systems provide relevant context for this study. Heavy-fuel compression ignition engines already operate effectively on Jet-A under similar injection condition [153],[154], and current research programmes are now extending the same hardware to SAF blends [155],[156]. Experimental work by Kleissner and Hoffman [156] confirms that modern engines can run on SAFs, such as hydrotreated vegetable oils and synthetic kerosene, without hardware modifications. These findings support the drop-in potential of SAFs, though optimised injection timing and duration remain critical for achieving consistent performance and low emissions.

This part of the thesis contributes to the fundamental understanding of diesel-injection cavitation and spray dynamics by offering a comparative analysis of cavitation and spray behaviours across a range of conventional and sustainable fuels. While most fuels exhibited broadly similar trends, BCH showed distinct behaviour under Spray D conditions, with pronounced string cavitation and wider spray cone angles attributed to its higher viscosity. In the straight-orifice configuration, where geometric cavitation dominated, BCH showed more typical cavitation levels and spray angles comparable to the other fuels.

Injection duration also played a significant role. Short pulses increased flow unsteadiness and cavitation, resulting in larger fluctuations in spray cone angle. Longer pulses led to more stable internal flow, reduced cavitation intensity, and more consistent spray development. These observations highlight the importance of accounting for transient injection effects when evaluating the atomisation performance of SAFs.

Overall, this part of the thesis provides the first detailed experimental characterisation of cavitation and spray behaviour for SAF candidates such as BCH and C-4 under variable injection conditions and nozzle geometries. The results support ongoing efforts to optimise injection strategies for sustainable fuels and contribute to a growing experimental database for model validation in the context of decarbonising aviation systems.

4.4. Combustion and Emission Characteristics Analysis

Experiments were conducted at the high constant-volume pre-burn chamber of the Combustion Research Facility at Sandia National Laboratories. In the specific apparatus, each injection event commences by filling the vessel to a specified density with a premixed, combustible gas mixture (C_2H_2, O_2, CO_2, H_2O and N_2). The mixture is then ignited to create a high pressure/temperature environment through the initial premixed combustion. The combustion products subsequently cool over a time period of the order of 1 second, due to heat transfer through the vessel walls, and therefore pressure slowly decreases. Once the desired p/T conditions are reached, fuel is injected and auto-ignites leading to the main combustion event. Fuel injection was performed using an ECN single-hole Spray D pressurised to 1500 bar at its inlet with the use of a syringe pump. Seven types of diesel fuel were examined in total, namely: (i) a conventional (fossil) base diesel, (ii) an RME biodiesel, (iii) a B10 base/biodiesel blend and a (iv) Hydrotreated Vegetable Oil (HVO) renewable fuel along with three counterparts for (v) the fossil diesel, (vi) RME biodiesel and (vii) HVO treated with a QAS-based viscoelasticity inducing agent at a concentration of 1000 mg/kg.

The total soot mass produced during the combustion event is calculated by integrating the mass per time instance over the entire duration that the soot cloud remains within the active measurement window. This methodology provides a basis for a straightforward comparison, and the results are presented in Figure 4.25 for all examined ambient conditions and fuels. It is noteworthy to mention that the peak measurable optical thickness value is limited by the characteristics of the optical system; the optical system utilised in this investigation can measure a maximum KL value of ~4. In some experimental conditions, localised regions reach this saturation limit, particularly at elevated ambient temperatures. For the ambient temperature of 1200 K, a comparison of high-soot fuels namely base diesel, B10 blend, and their additised counterparts are affected by this measurement ceiling, which introduces a potential bias. However, the effect of the additive action on these fuels is consistently illustrated, particularly from the combustion events at lower temperatures, notably between 900–1100 K, as detailed in Figure 4.25. Initially, a time sequence of optical-thickness contour plots is presented in Figure 4.23 to illustrate the basic features of the topology evolution of the soot cloud within the active window. For an ambient of 1000 K, soot formation begins approximately 0.90 milliseconds after injection. Optical thickness, KL, progressively increases as soot is formed in the fuel-rich head of the jet. It reaches its maximum level at around 1.20 ms after start of injection.

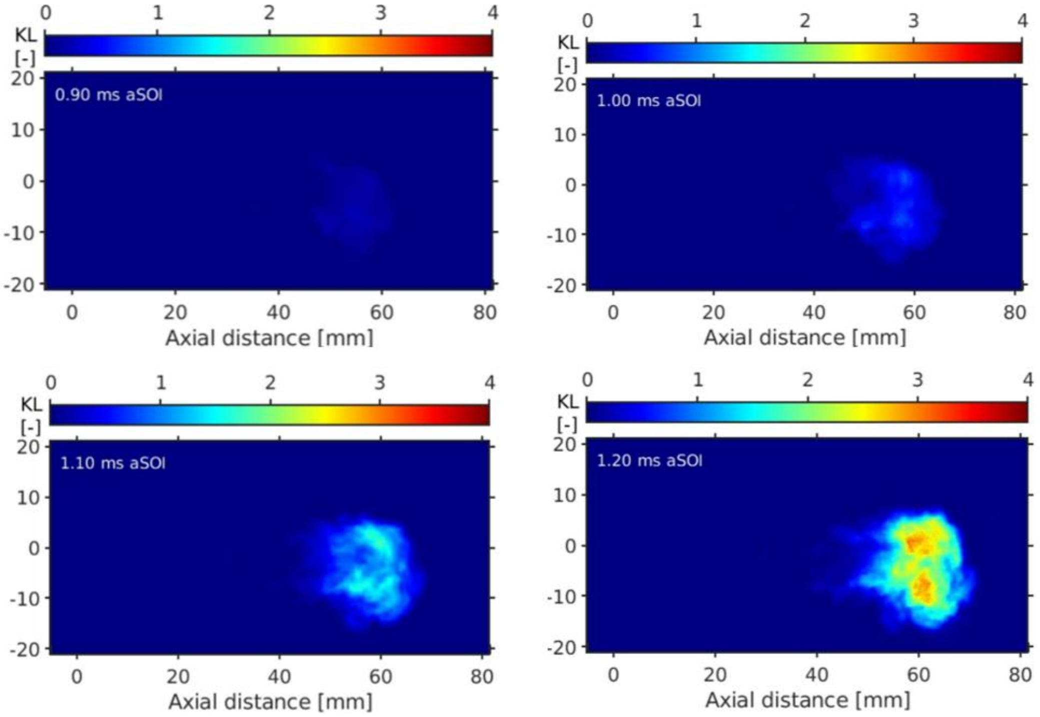

Figure 4.23: Time-sequenced images of the soot optical thickness (KL) for an ambient temperature of 900 K (base diesel).

Soot mass measurements over time, displayed for ambient temperatures from 900K to 1200K in Figure 4.24, reveal a uniform pattern in soot generation across all types of fuels and temperature conditions. Furthermore, an extensive array of measurements encompassing ignition delay, lift-off length, and liquid length for all fuels within the ambient temperature range of 800K to 1200K are presented in, Figure 4.26a-b and Figure 4.27 respectively. It is important to note that the ignition delay decreases with increasing ambient temperature, as substantiated by the temperature versus ignition delay graph presented in Figure 4.26a. This inverse relationship prompts an earlier initiation of soot formation as the ambient temperature rises. Therefore, at the highest ambient temperature of 1200K, the ignition delay is at its minimum, leading to the promptest appearance of peak soot mass during the measurement time frame. This trend highlights the sensitivity of soot generation dynamics to temperature variations, where elevated temperatures accelerate the combustion reactions, causing an advanced onset of peak soot accumulation. Ignition delay, the time taken for fuel to ignite after the onset of the combustion process, has a direct impact on the flame lift-off length. Lift-off length strongly affects combustion since the air entrained into a diesel spray upstream of the flame lift-off length will mix with the injected fuel [140]. An increase in ignition delay is typically associated with a longer flame lift-off length [157], which allows more air to mix with the fuel spray. This enhanced mixing between fuel and oxidizer leads to a more complete combustion process. As a result, fewer hydrocarbons remain unburned, reducing the mass of soot produced. Viscoelastic additive to diesel increased ignition delay and lift-off (as shown in Figure 4.26a and b), However, this effect was reversed in bio-derived fuels, aligning with the soot data depicted in Figure 4.24 and Figure 4.25.

Figure 4.27 depicts the length of the liquid core protruding from the injector outlet for all fuel samples at different ambient conditions. As anticipated, an increase in ambient temperature leads to enhanced liquid vaporisation, which consequently results in a reduction of the liquid length. Although differences between Newtonian and viscoelastic counterparts lie on the verge of measuring uncertainty, interestingly, there are hints that the additised fossil sample shows a slightly increased core length compared to the conventional fuel, a trend that is not followed in the cases of RME and HVO fuels. An increased liquid length indicates that fuel penetrates farther into the combustion chamber, producing a leaner mixture and necessitating a greater distance for flame stabilisation.

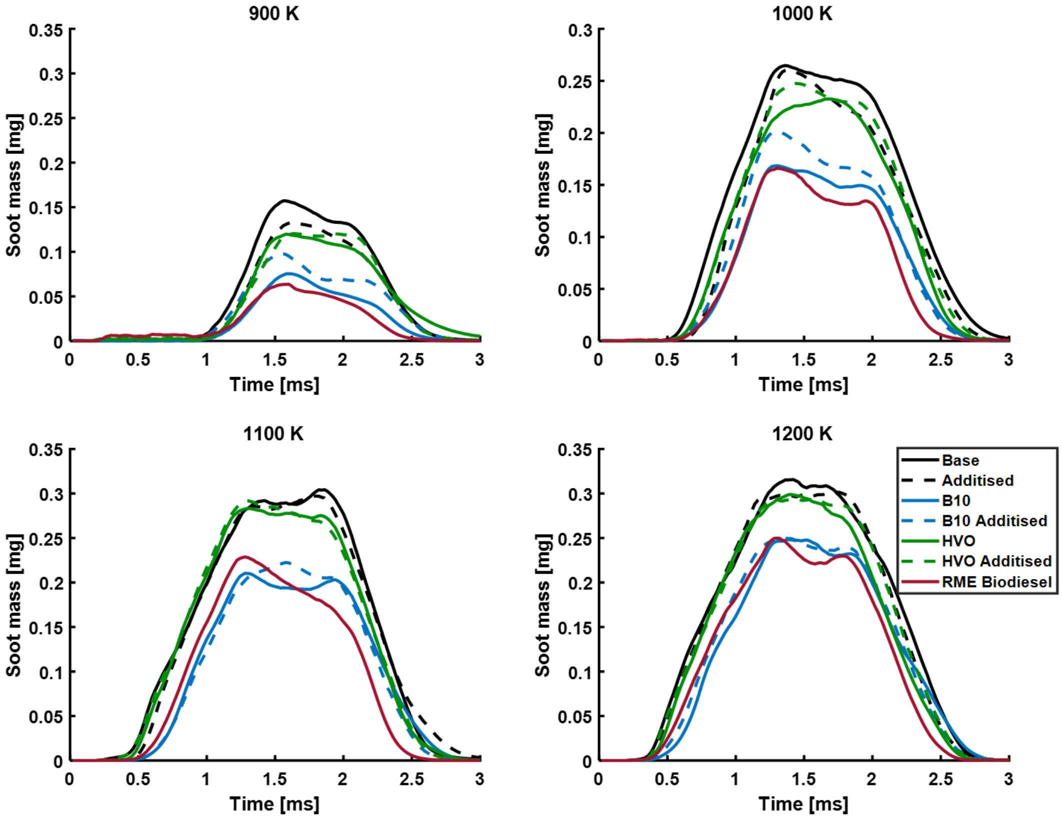

Figure 4.24: Temporal soot emission of all fuels at different temperatures.

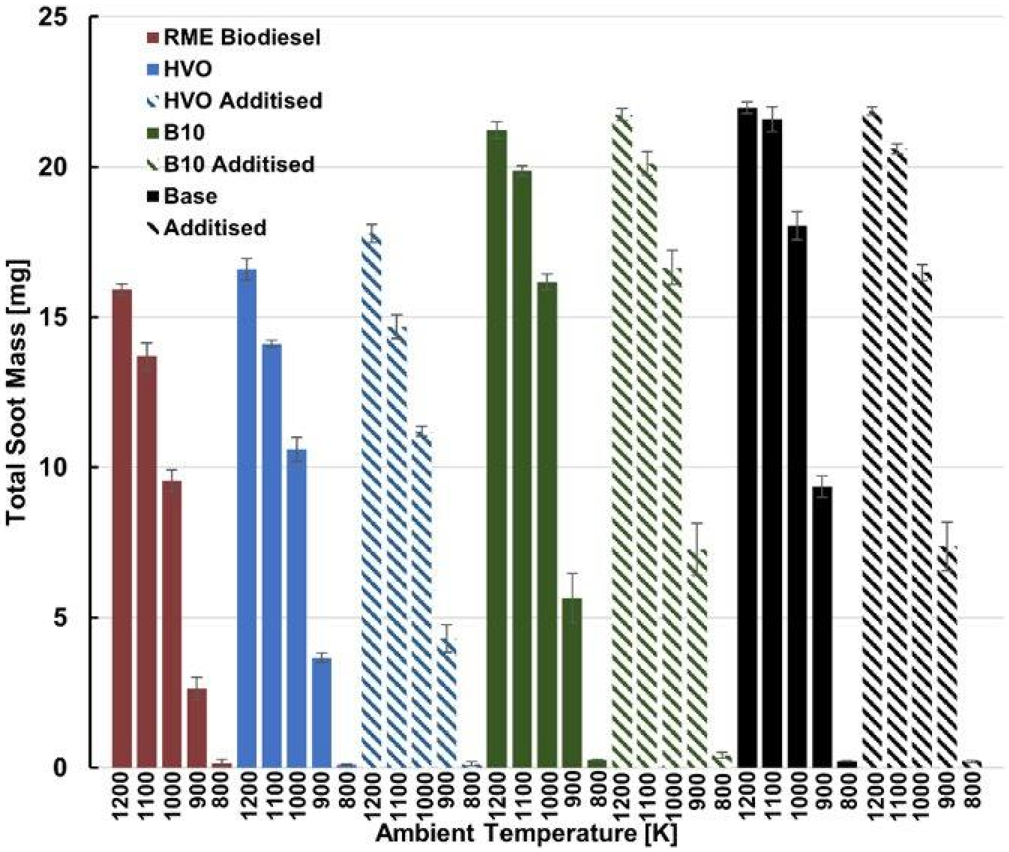

Figure 4.25: Total soot mass produced by the examined fuel samples during a combustion event. Error bars correspond to standard statistical error.

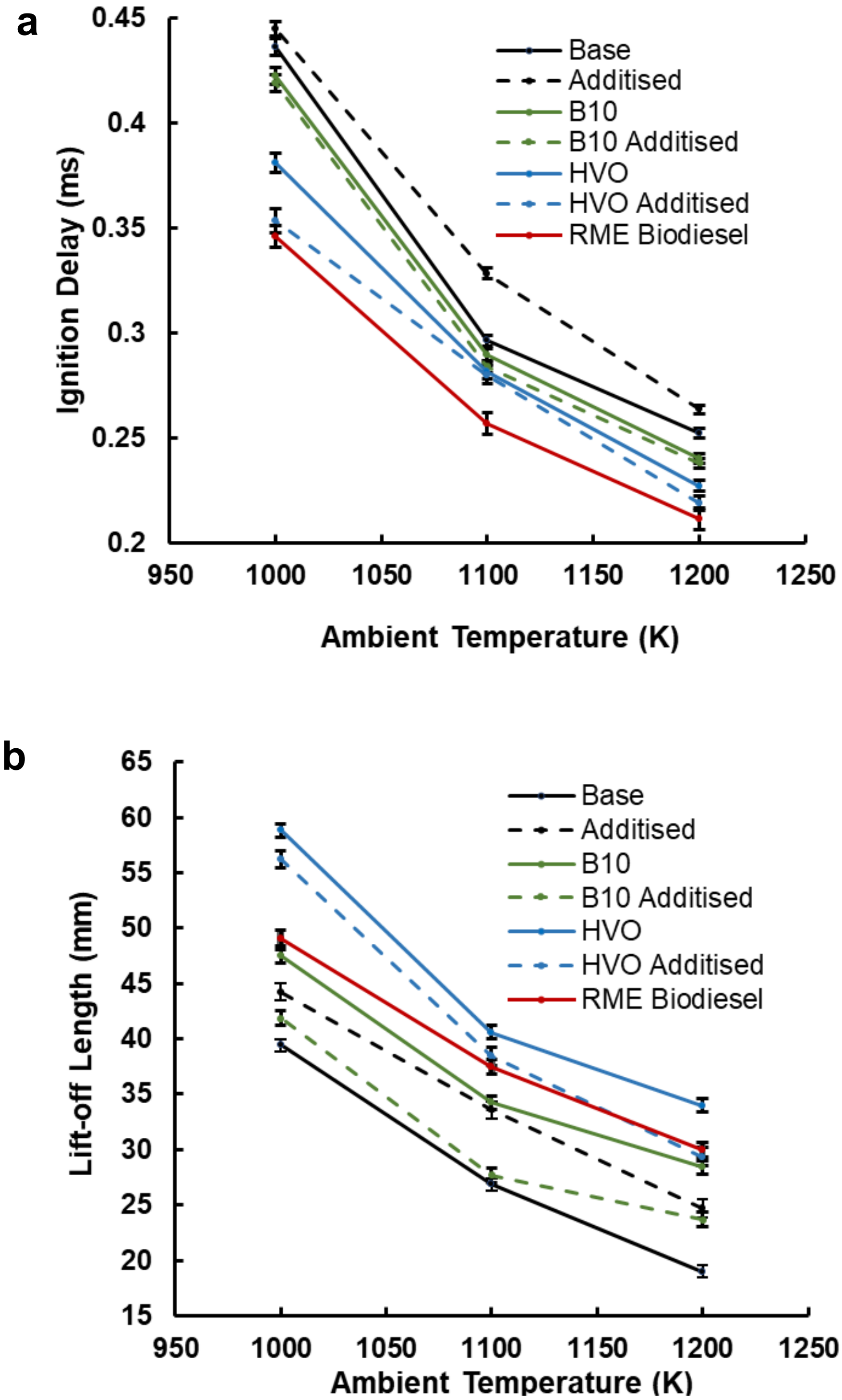

Figure 4.26: Lift-off length versus ambient temperature, error bars correspond to standard statistical error. (a) Ignition delay and (b) flame lift-off length as a function of ambient temperature. Additised samples are denoted with dashed lines. Error bars correspond to standard statistical error.

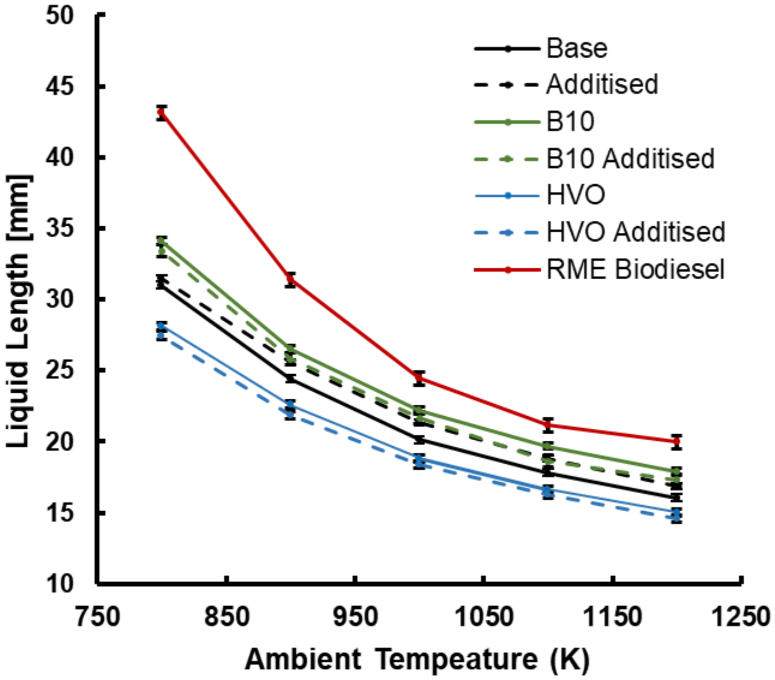

Figure 4.27: Liquid length versus ambient temperature, error bars correspond to standard statistical error.

To support the justification of the trends observed in the combustion chamber, complementary experiments were conducted in a miniaturised vessel with a DBI setup, as previously presented in Figure 3.5 and the imaging system in Figure 3.6. The experiments utilised the Spray C and Spray M injectors for base fuel, additised fuel, B10, and B10 additised fuel. For Spray C, an injection pressure of 700 bar and an ambient pressure of 1 bar were employed, whereas for Spray M, an injection pressure of 500 bar and an ambient pressure of 5 bar were used.

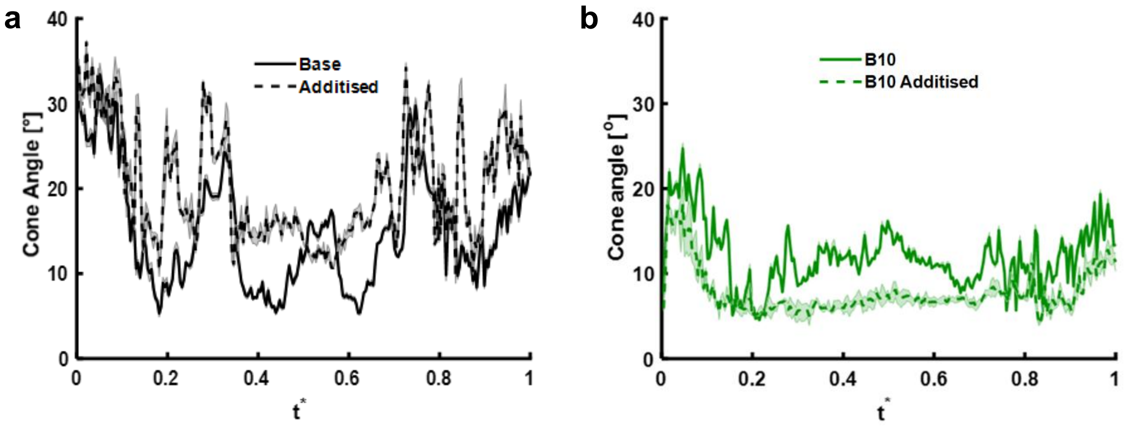

Figure 4.28: Comparison of spray cone angles for Spray C at 1 bar ambient condition.

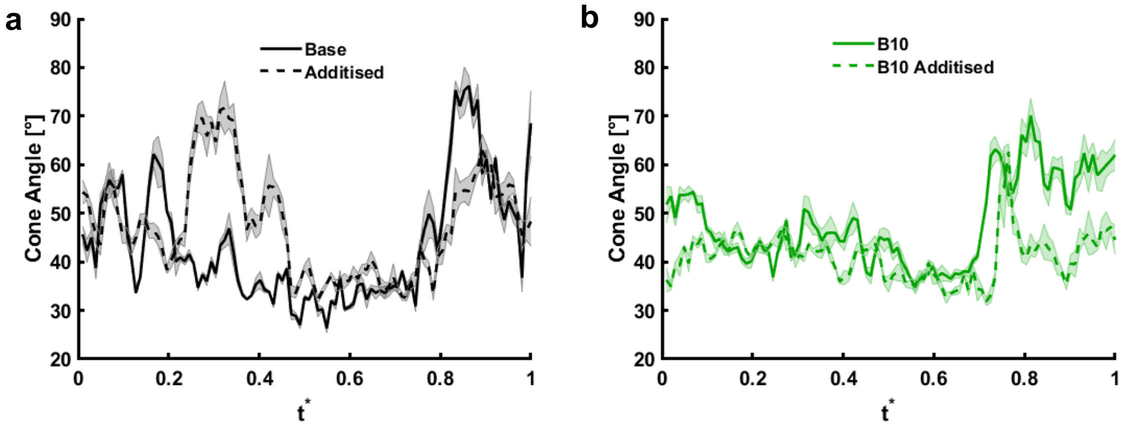

Figure 4.29: Comparison of spray cone angles for Spray M at 5 bar ambient condition.

Table 4.3: Mean spray angles of Spray C and Spray M throughout the injection event.

Fuel	**Mean Spray Angle [°]**	
	Spray C	Spray M
Base	15.1	43.8
Additised	20.3	47.5
B10	34.4	48.2
B10 Additised	30.2	41.1

The spray angle is associated with the air entrainment into the turbulent jet [158]. Viscoelastic additive enhances the spray cone angle for fossil fuel; which shows enhanced air entrainment into the fuel spray. This results in the formation of a leaner mixture, consequently leading to a reduction in soot formation. Contrastingly, the application of viscoelastic additives in renewable fuels manifests an inverse effect, leading to a reduction in the spray cone angle. This alteration promotes the development of a richer fuel mixture which promotes soot production [94],[159], subsequently escalating the propensity for soot formation.

4.4.1. Conclusions

High-speed diffuse backlight illumination extinction imaging and OH^* chemiluminescence visualisation provided a thorough evaluation of the impact of QAS-based additives, known for inducing viscoelastic properties, on the combustion dynamics and soot emissions of conventional and alternative diesel fuels. A detailed comparative analysis quantified soot emissions and investigated combustion efficiency metrics, including ignition delay and flame lift-off length. The investigation also explored the fuel spray morphology. Quantitative data derived from post-processed images were evaluated comparatively to clarify the effect of the QAS agent on the combustion characteristics of the various blends. The results indicated that the introduction of additives alters the flow behaviour of the fuel spray, subsequently influencing combustion quality and soot generation. These additives showed a beneficial effect for conventional fossil diesel, reducing soot mass by extending both the ignition delay and flame lift-off trajectory. Conversely, bio-derived fuels exhibited increased emissions when treated with additives. This disparity is attributed to the role of fluid viscoelastic properties, particularly the formation, size, structure, and flexibility of viscoelastic micelles, which are governed by the molecular composition of both the base fuel and the viscoelasticity-inducing agent.

4.4.2. Critical Review

This section provides a brief commentary on the literature that emerged following the submission of the article corresponding to this part of the Results chapter. It builds on the previous findings from the QAS cavitation–spray study [160], presented in the preceding section of this thesis, where QAS-treated fuels were shown to suppress wall-attached cavitation and enhance the formation of longitudinal vortices, resulting in broader spray cone angles. The current investigation extends this foundation by evaluating how these changes affect ignition behaviour and soot formation under engine-relevant thermodynamic conditions.

By combining DBI extinction imaging and OH^* chemiluminescence, this study provides rare experimental data linking nozzle flow phenomena to downstream combustion behaviour. The results confirm that QAS additives reduce soot emissions in fossil diesel by increasing ignition delay and flame lift-off length, allowing more time for fuel–air mixing. These combustion effects are consistent with the enhanced spray dispersion previously observed, supporting the hypothesis that viscoelastic fuel behaviour improves mixture preparation.

In contrast, when applied to renewable fuels such as FAME biodiesel and HVO, the same QAS additive produced higher soot emissions, despite similar trends in ignition delay. This divergence points to a complex interaction between additive-induced rheology and the chemical pathways of soot formation, which appears to be highly dependent on fuel composition. These findings underscore the need for additive strategies that are tailored to the specific characteristics of renewable fuels.

Taken together, the two parts of the research demonstrate that QAS additives influence both hydrodynamic and combustion phases of diesel engine operation. The work contributes to a growing body of evidence supporting the integrated evaluation of fuel properties, injector flow behaviour, and combustion chemistry when developing low-emission fuel blends. This approach is especially relevant as future engine technologies continue to explore renewable and additised fuels under increasingly stringent environmental constraints.

5. Conclusions and Future Work

This research has enhanced the understanding of the complex interrelation between fuel properties, cavitation dynamics, spray behaviour, and combustion characteristics under high-pressure injection conditions. By utilising real-size transparent nozzles and advanced diagnostic techniques, it has provided novel insights into how conventional diesel, biodiesel blends, sustainable aviation fuels, and Quaternary Ammonium Salt additised fuels influence injector performance, combustion efficiency, and soot emissions.

One of the critical findings of this study is the impact of QAS additives on cavitation and spray dynamics in diesel fuels. The research demonstrates that these additives suppress geometric cavitation while enhancing longitudinal vortices, leading to modified spray cone angles that improve air–fuel mixing. Using advanced imaging techniques such as high-speed diffuse backlight illumination extinction imaging and OH^* chemiluminescence, the research provided detailed combustion metrics like ignition delay, lift-off length, and soot mass.

In fossil-derived diesel fuels treated with QAS additives, a clear trend towards reduced soot formation was observed under the optically accessible, single-injector conditions studied in this work. Conversely, in non-fossil fuels like biodiesel blends, QAS treatment resulted in slightly increased emissions, revealing complex interactions influenced by fuel composition, molecular structure, and viscoelastic properties. These findings underscore the importance of considering fuel composition and viscoelastic properties when applying QAS additives, as their effectiveness varies depending on the type of fuel.

Table 5.1 is presented to illustrate the concentration and chemical function of several common fuel additives used to enhance combustion characteristics and overall fuel performance. Notably, while additives such as Olefin Copolymer (OCP) and Polyalkylmethacrylate (PMA) are typically employed at relatively high concentrations by weight to impart viscoelastic properties and modify shear-dependent flow resistance, the QAS additive used in this study was applied at a markedly lower concentration. Despite this modest dosage, QAS exhibited a pronounced impact on injector performance and soot reduction in fossil-derived diesel fuels. This underscores its high efficacy relative to its concentration, particularly when compared to other additives that require significantly larger quantities to achieve similar effects. The ability of QAS to influence cavitation dynamics and enhance air–

fuel mixing at such low concentrations highlights its potential as a highly effective and efficient additive for cleaner combustion strategies.

Table 5.1. Fuel additives with their chemical functions and typical weight concentrations [80],[161],[162].

Additive Type	Chemical Function	Concentration (weight%)
Combustion Improver CI-A	Increase cetane number; shorten ignition delay for smoother combustion	0.25
Olefin Copolymer (OCP)	Impart viscoelasticity; enhance heat transfer by reducing thermal boundary layers	3.04
Polyalkylmethacrylate (PMA)	Shear-thinning viscosity modifier; alters flow resistance under varying shear	4.44
Quaternary Ammonium Salt (QAS)	Remove and prevent injector and combustion deposits	0.10

The study also contributes to building a comprehensive database for new fuels by investigating their injection dynamics, including cavitation and spray characteristics, under varied injection pulse durations using ECN Spray C and Spray D nozzles. Experiments were conducted with conventional diesel, Jet-A, and sustainable aviation fuels such as bicyclohexyl and C-4. The comparative analysis revealed that specific fuel properties, particularly viscosity, influence cavitation and spray behaviour. Notably, BCH exhibited pronounced vortical cavitation in the Spray D nozzle, resulting in wider spray cone angles. Such behaviour is advantageous for enhancing air–fuel mixing, which is critical for efficient combustion and emissions reduction. These findings indicate that BCH, with its favourable spray characteristics, shows strong potential as an attractive SAF candidate for aviation applications. Furthermore, the results underscore the importance of optimising injection parameters, such as pulse duration and nozzle geometry, to tailor the spray behaviour of SAFs like BCH and C-4, thereby improving combustion efficiency and supporting the aviation sector's transition towards sustainable fuel alternatives.

Lastly, this research also makes a substantial methodological contribution by integrating dual-sided high-speed imaging techniques, enabling a comprehensive visualisation of in-nozzle and near-nozzle flow dynamics. The findings offer critical data for refining computational models, designing advanced injectors, and developing strategies to reduce emissions in internal combustion engines. Collectively, these insights represent a significant step towards achieving cleaner, more efficient fuel injection systems for transportation.

The optical diagnostics and the constant volume combustion chamber used in this study offer a controlled setting that allows the effects of fuel composition, cavitation, and early spray behaviour to be examined in detail. However, real diesel engines operate under a much more complex mix of thermochemical and fluid-mechanical effects than this simplified setup can fully capture. In real combustion engines, combustion begins within a swirling and tumbling in-cylinder flow that is created during the intake stroke and then reshaped by the recirculation produced by the piston bowl once injection starts. This movement influences the way the air and fuel blend, how ignition develops, how the flame holds, and how the equivalence ratio varies across the chamber. At the same time, pressure and temperature change rapidly during compression and expansion, affecting ignition chemistry, the formation of soot precursors, and the oxidation of emissions later in the cycle. These effects cannot be reproduced in a constant volume system.

Soot formation in real diesel engines is governed by a broader set of interacting processes than those captured in the constant-volume combustion chamber used in this study. Although the chamber allows precise control of temperature, pressure, oxygen concentration, and injection timing, it does not capture important in-cylinder features such as changing load conditions, strong swirl and tumble motion, recirculation generated by the piston bowl, or the development of wall films. In a real engine, these processes influence the local fuel–air ratio, the movement and residence time of soot precursors, and the spatial distribution of oxidising species. During the compression and expansion strokes, turbulence changes greatly, shifting the balance between soot inception, and agglomeration. These time-dependent processes cannot be fully represented in a chamber where the ambient field is uniform and stationary. As a result, although the soot-reducing behaviour seen with QAS-treated fossil diesel is well supported by the underlying chemistry, its overall impact may vary in real engines. In real engine conditions, factors such as cycle-to-cycle variability, and interactions between the fuel and engine walls introduce extra sources for soot formation [163],[164]. Spray-wall impingement can create liquid films that under engine conditions leading to generation of large quantities of soot [165]. This effect is not present in the optically accessible configuration. Furthermore, exhaust gas recirculation decreases the local oxygen available for combustion and raises the gas heat capacity, both of which act to slow soot oxidation and can therefore diminish some of the gains offered by improved spray dispersion [166]. The constant-volume configuration used in this study isolates in-flame soot formation, enabling clear attribution of trends to fuel composition, cavitation behaviour, spray development, and the effectiveness of viscoelastic additives. This isolation allows for a much clearer view than is possible in real engines, where many competing processes can obscure the effects of individual fuel or injector parameters. At the same time, chamber experiments cannot capture soot-turbulence interactions, late-cycle oxidation shaped by the expanding flow field, or the thermal interactions between the fuel and the chamber walls. Therefore, the soot dynamics measured here represent fundamental behaviour rather than complete engine-scale soot evolution. For this reason, the findings should be viewed as identifying the underlying mechanisms that govern soot formation rather than directly predicting in-cylinder soot emissions under practical operating conditions. To clarify which real-engine mechanisms are not fully represented in the present experiments, Table 5.2 outlines key diesel engine processes and indicates the extent to which they are represented in this study.

Table 5.2: Representation of key diesel engine processes in the present experiments.

Real-Engine Process	Importance in Real Engine	Present experiments
In-cylinder swirl and tumble	Influence mixture formation, ignition, flame stabilisation, and soot oxidation	Not represented; quiescent ambient used to isolate fuel and spray effects
Fuel-wall interaction	Major contributor to soot precursors	Not represented; chamber does not produce realistic wall impingement
Multi-pulse injection	Shape combustion phasing and influence soot–NOx behaviour	Not represented; single injections used for clarity and repeatability
Exhaust-gas dilution	Modifies soot oxidation rates and local oxygen availability	Only approximated through fixed oxygen concentration
Multi-hole jet interaction	Affects plume deflection, mixing, and soot distribution	Not represented in combustion experiments

The mechanisms defined in Table 5.2 which shows the limitations of this study also indicate important directions for future research, particularly those required to apply the present fundamental findings to real engine environments.

Despite these advancements, further research is needed to deepen the understanding of molecular-level interactions between QAS additives and bio-derived fuels. Although QAS has proven effective in reducing soot emissions in fossil diesel, its limited impact in biodiesel blends suggests that it interacts differently with components such as fatty acid methyl esters (FAMEs). Understanding these mechanisms could support the development of optimised additive formulations tailored to the specific chemistry of biofuels. Furthermore, a broader investigation into alternative additives is recommended to improve fuel performance across diverse fuel types. Experimental studies on non-Newtonian polymer additives used in hydraulic systems have shown that adjusting molecular characteristics, such as chain flexibility and normal stress differences, can significantly affect flow behaviour, vortex suppression, and friction losses in complex geometries [161]. Similarly, recent molecular dynamics simulations have demonstrated that modifying additive chemistry at the nanoscale can influence thermophysical properties and interfacial interactions in complex fluids, such as nanofluids for thermal management [79],[80]. These findings highlight the importance of atomistic-level insight in the optimisation of additive design. Applying such molecular-scale approaches to QAS–biofuel systems could enable the rational development of next-generation fuel additives, using principles that have already proven effective in other advanced fluid systems.

Additionally, investigating different injector geometries, particularly those widely used in modern diesel and aero-diesel engines under relevant operating conditions could offer deeper insights into how design influences cavitation and spray dynamics when using viscoelastic additives. Such an investigation is especially critical for SAFs, given that multi-hole injectors introduce complex flow phenomena that directly affect spray formation, air–fuel mixing, and subsequent combustion. Together with SAFs, this area constitutes a principal strength of the present work, demonstrating the relevance of advanced nozzle diagnostics and high-fidelity spray analysis for future fuel injection research. Long-term engine performance testing, such as extended endurance evaluations under standardised transient and steady-state engine cycles, is essential to scientifically validate the sustained impact of QAS additives on fuel injection and combustion systems. Additionally, evaluating the environmental impacts of QAS additives, exploring alternative emission reduction strategies, expanding research to other sustainable fuels, investigating the effects of injection parameters, and integrating findings with aftertreatment systems could further advance cleaner combustion technologies, supporting the transition towards sustainable and environmentally friendly internal combustion engines.

This research has laid a strong foundation for understanding the complex interplay between fuel properties, additives, and injection dynamics. By addressing these areas in future studies, researchers can advance the development of sustainable, efficient, and low-emission technologies for internal combustion engines, driving progress across automotive, aviation, and heavy-duty transportation sectors.

6. Publications

Peer-reviewed journal publications

- O. Baran, I. K. Karathanassis, P. Koukouvinis, J. Hwang, L. M. Pickett, D. Spivey, and M. Gavaises, “Assessment of injector-flow characteristics of additised and renewable diesel blends through high-speed imaging” Fuel, vol. 352, no. 129076, Jul. 2023, doi: 10.1016/j.fuel.2023.129076.

- O. Baran, I. K. Karathanassis, L. M. Pickett, J. Manin, and M. Gavaises, “High-Speed Optical Imaging of Cavitation and Spray Dynamics for Sustainable Aviation Fuels” Energy & Fuels, vol.39, no. 24, June 2025, doi: 10.1021/acs.energyfuels.5c01353.

Pending journal publications

- I. K. Karathanassis, O. Baran, J. Manin, L. M. Pickett, and M. Gavaises, “Combustion and emissions characteristics of conventional, renewable and synthetic diesel fuels at realistic operating conditions”, Combustion and Flame, Under Review.

Conference/workshop proceedings

- I. K. Karathanassis, O. Baran, J. Manin, L. Pickett, D. Spivey, and M. Gavaises, "Combustion and emissions characteristics of alternative diesel-fuel blends," in Proc. ILASS Europe 2023, 32nd European Conf. Liquid Atomization & Spray Systems, Napoli, Italy, Sep. 2023.

REFERENCES

[1] S. Tagliapietra, "Energy Consumption and Energy Efficiency," in *Global Energy Fundamentals (Economics, Politics, and Technology)*, no. June 2019, Cambridge University, 2020, ch. 8, pp. 168–189.

[2] F. Leach, G. Kalghatgi, R. Stone, and P. Miles, "The scope for improving the efficiency and environmental impact of internal combustion engines," *Transportation Engineering*, vol. 1, no. April, 2020, doi: 10.1016/j.treng.2020.100005.

[3] T. M. Letcher, *Observed impacts on Planet Earth*, Second Edi. Elsevier, 2009.

[4] ExxonMobil, "2017 Outlook for Energy : A View to 2040 Our energy to 2040 : Seven things to know," 2017.

[5] C. S. Lee and S. W. Park, "An experimental and numerical study on fuel atomization characteristics of high-pressure diesel injection sprays," *Fuel*, vol. 81, no. 18, pp. 2417–2423, 2002, doi: 10.1016/S0016-2361(02)00158-8.

[6] L. Broniarz-Press *et al.*, "The effect of orifice shape and the injection pressure on enhancement of the atomization process for pressure-swirl atomizers," *Crop Protection*, vol. 82, pp. 65–74, 2016, doi: 10.1016/j.cropro.2016.01.005.

[7] J. E. Johnson *et al.*, "Characteristics of 3000 bar Diesel spray injection under non-vaporizing and vaporizing conditions," *ICLASS 2012 - 12th International Conference on Liquid Atomization and Spray Systems*, vol. c, no. Figure 1, pp. 6–13, 2012.

[8] G. Boccardo *et al.*, "Experimental investigation on a 3000 bar fuel injection system for a SCR-free non-road diesel engine," *Fuel*, vol. 243, no. October 2018, pp. 342–351, 2019, doi: 10.1016/j.fuel.2019.01.122.

[9] W. Vera-Tudela, R. Haefeli, C. Barro, B. Schneider, and K. Boulouchos, "An experimental study of a very high-pressure diesel injector (up to 5000 bar) by means of optical diagnostics," *Fuel*, vol. 275, no. April, p. 117933, 2020, doi: 10.1016/j.fuel.2020.117933.

[10] C. Y. Moon, G. M. Magnotti, B. A. Sforzo, A. Tekawade, A. L. Kastengren, and C. F. Powell, "Experimental Investigation of Cavitation-Induced Erosion Using X-Ray Imaging and Tomography," *Front Mech Eng*, vol. 8, no. May, pp. 1–10, 2022, doi: 10.3389/fmech.2022.869165.

[11] B. Rajesh Kumar and S. Saravanan, "Partially premixed low temperature combustion using dimethyl carbonate (DMC) in a di diesel engine for favorable smoke/NOx emissions," *Fuel*, vol. 180, pp. 396–406, 2016, doi: 10.1016/j.fuel.2016.04.060.

[12] S. Niemi *et al.*, "Effects of wood-based renewable diesel fuel blends on the performance and emissions of a non-road diesel engine," *Fuel*, vol. 186, pp. 1–10, 2016, doi: 10.1016/j.fuel.2016.08.048.

[13] H. K. Suh and C. S. Lee, “A review on atomization and exhaust emissions of a biodiesel-fueled compression ignition engine,” *Renewable and Sustainable Energy Reviews*, vol. 58, pp. 1601–1620, 2016, doi: 10.1016/j.rser.2015.12.329.

[14] X. Zhu and Ö. Andersson, “Performance of new and aged injectors with and without fuel additives in a light duty diesel engine,” *Transportation Engineering*, vol. 1, no. April, p. 100007, 2020, doi: 10.1016/j.treng.2020.100007.

[15] A. K. Agarwal, A. P. Singh, and R. K. Maurya, “Evolution, challenges and path forward for low temperature combustion engines,” *Prog Energy Combust Sci*, vol. 61, pp. 1–56, 2017, doi: 10.1016/j.pecs.2017.02.001.

[16] A. K. Agarwal, D. K. Srivastava, A. Dhar, R. K. Maurya, P. C. Shukla, and A. P. Singh, “Effect of fuel injection timing and pressure on combustion, emissions and performance characteristics of a single cylinder diesel engine,” *Fuel*, vol. 111, pp. 374–383, 2013, doi: 10.1016/j.fuel.2013.03.016.

[17] D. N. Cao, A. T. Hoang, H. Q. Luu, V. G. Bui, and T. T. H. Tran, “Effects of injection pressure on the NOx and PM emission control of diesel engine: A review under the aspect of PCCI combustion condition,” 2020, *Taylor and Francis Inc.* doi: 10.1080/15567036.2020.1754531.

[18] M. Gumus, C. Sayin, and M. Canakci, “The impact of fuel injection pressure on the exhaust emissions of a direct injection diesel engine fueled with biodiesel-diesel fuel blends,” *Fuel*, vol. 95, pp. 486–494, May 2012, doi: 10.1016/j.fuel.2011.11.020.

[19] L. Zhang, Z. He, W. Guan, Q. Wang, and S. Som, “Simulations on the cavitating flow and corresponding risk of erosion in diesel injector nozzles with double array holes,” *Int J Heat Mass Transf*, vol. 124, pp. 900–911, Sep. 2018, doi: 10.1016/j.ijheatmasstransfer.2018.03.086.

[20] C. Author, R. Abu Bakar, and A. Rahim Ismail, “Fuel Injection Pressure Effect on Performance of Direct Injection Diesel Engines Based on Experiment,” *Am J Appl Sci*, vol. 5, no. 3, pp. 197–202, 2008.

[21] X. Wang, Z. Huang, O. A. Kuti, W. Zhang, and K. Nishida, “An experimental investigation on spray, ignition and combustion characteristics of biodiesels,” *Proceedings of the Combustion Institute*, vol. 33, no. 2, pp. 2071–2077, 2011, doi: 10.1016/j.proci.2010.07.037.

[22] L. Brennan and P. Owende, “Biofuels from microalgae-A review of technologies for production, processing, and extractions of biofuels and co-products,” *Renewable and Sustainable Energy Reviews*, vol. 14, no. 2, pp. 557–577, 2010, doi: 10.1016/j.rser.2009.10.009.

[23] F. R. Westlye, M. Battistoni, S. A. Skeen, J. Manin, L. M. Pickett, and A. Ivarsson, “Penetration and combustion characterization of cavitating and non-cavitating fuel

injectors under diesel engine conditions," *SAE Technical Papers*, vol. 2016-April, no. April, 2016, doi: 10.4271/2016-01-0860.

[24] F. Payri, V. Bermúdez, R. Payri, and F. J. Salvador, "The influence of cavitation on the internal flow and the spray characteristics in diesel injection nozzles," *Fuel*, vol. 83, no. 4–5, pp. 419–431, 2004, doi: 10.1016/j.fuel.2003.09.010.

[25] P. Koukouvinis, N. Mitroglou, M. Gavaises, M. Lorenzi, and M. Santini, "Quantitative predictions of cavitation presence and erosion-prone locations in a high-pressure cavitation test rig," *J Fluid Mech*, vol. 819, pp. 21–57, 2017, doi: 10.1017/jfm.2017.156.

[26] L. C. Ganippa, G. Bark, S. Andersson, and J. Chomiak, "Comparison of cavitation phenomena in transparent scaled-up single-hole Diesel nozzles," *Symposium on Cavitation*, pp. 1–9, 2001, [Online]. Available: http://caltechconf.library.caltech.edu/68/

[27] H. Roth, M. Gavaises, and C. Arcoumanis, "Cavitation initiation, its development and link with flow turbulence in diesel injector nozzles," *SAE Technical Papers*, vol. 2002, no. 724, 2002, doi: 10.4271/2002-01-0214.

[28] R. Balz, A. Schmid, and D. Sedarsky, "In-Nozzle Flow Visualization of Marine Diesel Injector Nozzles with Different Inlet Radii," *Proceedings of the 10th International Symposium on Cavitation (CAV2018)*, pp. 567–571, 2019, doi: 10.1115/1.861851_ch108.

[29] J. Manin, L. M. Pickett, and K. Yasutomi, "Transient cavitation in transparent diesel injectors," *ICLASS 2018 - 14th International Conference on Liquid Atomization and Spray Systems*, pp. 1–9, 2020.

[30] E. Cenker, A. Bennett, and W. L. Roberts, "Investigations of the long-term effects of LII on soot and bath gas," *Aerosol Science and Technology*, vol. 51, no. 12, pp. 1354–1367, Dec. 2017, doi: 10.1080/02786826.2017.1368444.

[31] M. Gavaises, "Flow in valve covered orifice nozzles with cylindrical and tapered holes and link to cavitation erosion and engine exhaust emissions," *International Journal of Engine Research*, vol. 9, no. 6, pp. 435–447, 2008, doi: 10.1243/14680874JER01708.

[32] A. Andriotis, M. Gavaises, and C. Arcoumanis, "Vortex flow and cavitation in diesel injector nozzles," *J Fluid Mech*, vol. 610, pp. 195–215, 2008, doi: 10.1017/S0022112008002668.

[33] Z. Chen *et al.*, "Experimental study on the effect of nozzle geometry on string cavitation in real-size optical diesel nozzles and spray characteristics," *Fuel*, vol. 232, no. May, pp. 562–571, 2018, doi: 10.1016/j.fuel.2018.05.132.

[34] M. Gavaises, D. Papoulias, A. Andriotis, E. Giannadakis, and A. Theodorakakos, "Link between cavitation development and erosion damage in diesel injector nozzles,"

SAE Technical Papers, vol. 2007, no. 724, pp. 776–790, 2007, doi: 10.4271/2007-01-0246.

[35] P. Dong, K. Nishida, and Y. Ogata, "Characterization of multi-hole nozzle sprays and internal flow for different nozzle hole lengths in direct-injection diesel engines," *Proceedings of the Institution of Mechanical Engineers, Part D: Journal of Automobile Engineering*, vol. 231, no. 4, pp. 500–515, 2017, doi: 10.1177/0954407016653890.

[36] M. Gavaises, A. Andriotis, D. Papoulias, N. Mitroglou, and A. Theodorakakos, "Characterization of string cavitation in large-scale Diesel nozzles with tapered holes," *Physics of Fluids*, vol. 21, no. 5, 2009, doi: 10.1063/1.3140940.

[37] H. Chaves and C. Ludwig, "Characterization of cavitation in transparent nozzles depending on the nozzle geometry," *Proceedings of the 20th ILASS - Europe Meeting 2005*, no. August, 2005, [Online]. Available: https://www.researchgate.net/profile/Humberto_Chaves/publication/259592708_Characterization_of_cavitation_in_transparent_nozzles_depending_on_the_nozzle_geometry/links/0046352cd68ac6c37a000000.pdf

[38] M. Blessing, G. König, C. Krüger, U. Michels, and V. Schwarz, "Analysis of flow and cavitation phenomena in diesel injection nozzles and its effects on spray and mixture formation," *SAE Technical Papers*, 2003, doi: 10.4271/2003-01-1358.

[39] M. Battistoni and C. N. Grimaldi, "Analysis of transient cavitating flows in diesel injectors using diesel and biodiesel fuels," *SAE Int J Fuels Lubr*, vol. 3, no. 2, pp. 879–900, 2010, doi: 10.4271/2010-01-2245.

[40] G. M. Magnotti and S. Som, "Assessing Fuel Property Effects on Cavitation and Erosion Propensity Using a Computational Fuel Screening Tool," *J Eng Gas Turbine Power*, vol. 142, no. 11, pp. 1–9, 2020, doi: 10.1115/1.4048457.

[41] Z. He, W. Zhong, Q. Wang, Z. Jiang, and Y. Fu, "An investigation of transient nature of the cavitating flow in injector nozzles," *Appl Therm Eng*, vol. 54, no. 1, pp. 56–64, 2013, doi: 10.1016/j.applthermaleng.2013.01.024.

[42] X. Zhang *et al.*, "Effect of fuel temperature on cavitation flow inside vertical multi-hole nozzles and spray characteristics with different nozzle geometries," *Exp Therm Fluid Sci*, vol. 91, pp. 374–387, 2018, doi: 10.1016/j.expthermflusci.2017.06.006.

[43] J. Matheis and S. Hickel, "Multi-component vapor-liquid equilibrium model for LES of high-pressure fuel injection and application to ECN Spray A," *International Journal of Multiphase Flow*, vol. 99, pp. 294–311, 2018, doi: 10.1016/j.ijmultiphaseflow.2017.11.001.

[44] C. Rodriguez Fernandez, "Supercritical, transcritical and subcritical real-fluid mixing at high-pressure conditions using the PC-SAFT EoS," City, University of London, 2019. [Online]. Available: http://openaccess.city.ac.uk/1189/

[45] N. Damanik, H. C. Ong, C. W. Tong, T. M. I. Mahlia, and A. S. Silitonga, "A review on the engine performance and exhaust emission characteristics of diesel engines fueled with biodiesel blends," *Environmental Science and Pollution Research*, vol. 25, no. 16, pp. 15307–15325, 2018, doi: 10.1007/s11356-018-2098-8.

[46] E. Buyukkaya, "Effects of biodiesel on a di diesel engine performance, emission and combustion characteristics," *Fuel*, vol. 89, no. 10, pp. 3099–3105, 2010, doi: 10.1016/j.fuel.2010.05.034.

[47] D. Singh, D. Sharma, S. L. Soni, S. Sharma, P. Kumar Sharma, and A. Jhalani, "A review on feedstocks, production processes, and yield for different generations of biodiesel," *Fuel*, vol. 262, no. November 2019, p. 116553, 2020, doi: 10.1016/j.fuel.2019.116553.

[48] A. K. Babu and G. Devaradjane, "Vegetable oils and their derivatives as fuels for CI engines: An overview," *SAE Technical Papers*, 2003, doi: 10.4271/2003-01-0767.

[49] B. R. Moser, "Biodiesel production, properties, and feedstocks," in *Biodiesel Production Properties and Feedstocks Biofuels*, vol. 45, no. 3, 2009, pp. 285–347. doi: 10.1007/s11627-009-9204-z.

[50] M. Elkelawy, M. Aly Farag, and H. E. Seleem, "Enhancing Diesel Engine Power Plant Efficiency and Cutting Emissions with Commercial Fuel Additives in Generator Systems," *Pharos Engineering Science Journal*, vol. 2, no. 1, pp. 37–46, Jun. 2025, doi: 10.21608/pesj.2025.352985.1012.

[51] A. K. Agarwal, "Biofuels (alcohols and biodiesel) applications as fuels for internal combustion engines," Jun. 2007. doi: 10.1016/j.pecs.2006.08.003.

[52] G. Kalghatgi, "Development of Fuel/Engine Systems—The Way Forward to Sustainable Transport," Jun. 01, 2019, *Elsevier Ltd*. doi: 10.1016/j.eng.2019.01.009.

[53] R. H. Barbour, R. Quigley, and A. Panesar, "Investigations into Fuel Additive Induced Power Gain in the CEC F-98-08 DW10B Injector Fouling Engine Test," *SAE Technical Papers*, vol. 2014-01–2721, 2014, doi: 10.4271/2014-01-2721.

[54] I. K. Karathanassis, K. Trickett, P. Koukouvinis, J. Wang, R. Barbour, and M. Gavaises, "Illustrating the effect of viscoelastic additives on cavitation and turbulence with X-ray imaging," *Sci Rep*, vol. 8, no. 1, pp. 1–15, 2018, doi: 10.1038/s41598-018-32996-w.

[55] H. Naseri, "Modelling of nozzle cavitation in newtonian and viscoelastic fluids," 2019.

[56] R. I. Taylor, "Fuel-Lubricant Interactions: Critical Review of Recent Work," 2021, doi: 10.3390/lubricants.

[57] J. Bennett and C. Mabille, "Advanced fuel additives for modern internal combustion engines," in *Alternative Fuels and Advanced Vehicle Technologies for Improved*

Environmental Performance: Towards Zero Carbon Transportation, Elsevier, 2022, pp. 197–229. doi: 10.1016/B978-0-323-90979-2.00002-0.

[58] S. De Jong *et al.*, "Life-cycle analysis of greenhouse gas emissions from renewable jet fuel production," *Biotechnol Biofuels*, vol. 10, no. 1, Mar. 2017, doi: 10.1186/s13068-017-0739-7.

[59] M. Shahabuddin, M. T. Alam, B. B. Krishna, T. Bhaskar, and G. Perkins, "A review on the production of renewable aviation fuels from the gasification of biomass and residual wastes," *Bioresour Technol*, vol. 312, Sep. 2020, doi: 10.1016/j.biortech.2020.123596.

[60] C. Bergero, G. Gosnell, D. Gielen, S. Kang, M. Bazilian, and S. J. Davis, "Pathways to net-zero emissions from aviation," *Nat Sustain*, vol. 6, no. 4, pp. 404–414, Apr. 2023, doi: 10.1038/s41893-022-01046-9.

[61] M. C. Massaro, R. Biga, A. Kolisnichenko, P. Marocco, A. H. A. Monteverde, and M. Santarelli, "Potential and technical challenges of on-board hydrogen storage technologies coupled with fuel cell systems for aircraft electrification," *J Power Sources*, vol. 555, Jan. 2023, doi: 10.1016/j.jpowsour.2022.232397.

[62] Z. Ji, M. M. Rokni, J. Qin, S. Zhang, and P. Dong, "Energy and configuration management strategy for battery/fuel cell/jet engine hybrid propulsion and power systems on aircraft," *Energy Convers Manag*, vol. 225, Dec. 2020, doi: 10.1016/j.enconman.2020.113393.

[63] European Union Aviation Safety Agency (EASA), "European Aviation Environmental Report 2022," 2022.

[64] S. S. Doliente, A. Narayan, J. F. D. Tapia, N. J. Samsatli, Y. Zhao, and S. Samsatli, "Bio-aviation Fuel: A Comprehensive Review and Analysis of the Supply Chain Components," *Front Energy Res*, vol. 8, Jul. 2020, doi: 10.3389/fenrg.2020.00110.

[65] E. Cabrera and J. M. Melo de Sousa, "Use of Sustainable Fuels in Aviation—A Review," *Energies (Basel)*, vol. 15, no. 7, Mar. 2022, doi: 10.3390/en15072440.

[66] Y. Mao *et al.*, "An experimental study of n-dodecane and the development of an improved kinetic model," *Combust Flame*, vol. 212, pp. 388–402, Feb. 2020, doi: 10.1016/j.combustflame.2019.11.014.

[67] J. Yu, Z. Wang, X. Zhuo, W. Wang, and X. Gou, "Surrogate Definition and Chemical Kinetic Modeling for Two Different Jet Aviation Fuels," *Energy and Fuels*, vol. 30, no. 2, pp. 1375–1382, Feb. 2016, doi: 10.1021/acs.energyfuels.5b02414.

[68] T. Edwards, L. Maurice, T. Edwards, and L. Maurice, "Surrogate Mixtures to Represent Complex Aviation and Rocket Fuels," in *35th AIAA/ASME/SAE/ASEE Joint' Propulsion Conference and Exhibit*, 1999.

[69] B. L. Smith and T. J. Bruno, "Composition-explicit distillation curves of aviation fuel JP-8 and a coal-based jet fuel," *Energy and Fuels*, vol. 21, no. 5, pp. 2853–2862, Sep. 2007, doi: 10.1021/ef070181r.

[70] X. Zhang, H. Lei, L. Zhu, J. Wu, and S. Chen, "From lignocellulosic biomass to renewable cycloalkanes for jet fuels," *Green Chemistry*, vol. 17, no. 10, pp. 4736–4747, Aug. 2015, doi: 10.1039/c5gc01583a.

[71] L. Cosimbescu *et al.*, "Properties of Bicyclic and Multicyclic Hydrocarbons as Bio-derived Compression Ignition Fuels That Can Be Prepared via Efficient and Scalable Routes from Biomass."

[72] Q. Liu *et al.*, "Relationship between molecular structure and pyrolysis performance for high-energy-density fuels," *Fuel*, vol. 358, Feb. 2024, doi: 10.1016/j.fuel.2023.130342.

[73] M. A. Díaz-Pérez and J. C. Serrano-Ruiz, "Catalytic production of jet fuels from biomass," *Molecules*, vol. 25, no. 4, Feb. 2020, doi: 10.3390/molecules25040802.

[74] M. Colket *et al.*, "Overview of the national jet fuels combustion program," in *AIAA Journal*, American Institute of Aeronautics and Astronautics Inc., 2017, pp. 1087–1104. doi: 10.2514/1.J055361.

[75] F. Di Sabatino, J. Manin, and K. Wan, "Single-Hole Atomizer (SHA) Research to Study Spray Flame Dynamics and Soot Formation for Aero-engine Combustion," American Institute of Aeronautics and Astronautics (AIAA), Jan. 2023. doi: 10.2514/6.2023-2046.

[76] E. C. Owens, M. E. Lepera, and S. J. Lestz, "Use of Aviation Turbine Fuel JP-8 as the Single Fuel on the Battlefield," in *SAE Technical Paper Series*, 1989.

[77] R. G. Papagiannakis, P. N. Kotsiopoulos, D. T. Hountalas, and E. Yfantis, "Single Fuel Research Program Comparative Results of the Use of JP-8 Aviation Fuel versus Diesel Fuel on a Direct Injection and Indirect Injection Diesel Engine," in *SAE Technical Papers*, 2006. doi: 10.4271/2006-01-1673.

[78] I. K. Karathanassis *et al.*, *X-ray phase contrast and absorption imaging for the quantification of transient cavitation in high-speed nozzle flows*, vol. 33, no. 3. 2021. doi: 10.1063/5.0038475.

[79] B. Ravikumar, I. K. Karathanassis, T. Smith, and M. Gavaises, "Multi-scale modelling of dilute viscoelastic liquids: Atomistic to mesoscale mapping of polymer solutions," *Polymer (Guildf)*, vol. 285, Oct. 2023, doi: 10.1016/j.polymer.2023.126360.

[80] B. Ravikumar, I. K. Karathanassis, T. Smith, and M. Gavaises, "Atomistic Investigation of Viscoelastic Nanofluids as Heat Transfer Liquids for Immersive-Cooling Applications," *Ind Eng Chem Res*, vol. 63, no. 48, pp. 21023–21037, Dec. 2024, doi: 10.1021/acs.iecr.4c01832.

[81] R. Niranjan and A. K. Thakur, "The toxicological mechanisms of environmental soot (black carbon) and carbon black: Focus on Oxidative stress and inflammatory pathways," *Front Immunol*, vol. 8, no. JUN, pp. 1–20, 2017, doi: 10.3389/fimmu.2017.00763.

[82] T. C. Bond, S. J. Doherty, D. W. Fahey, and E.t.al, "Bounding the role of black carbon in the climate system: A scientific assessment," *Journal of Geophysical Research Atmospheres*, vol. 118, no. 11, pp. 5380–5552, 2013, doi: 10.1002/jgrd.50171.

[83] European Commission, "Euro 7 Press Release," 2022. Accessed: Jun. 16, 2024. [Online]. Available: https://ec.europa.eu/commission/presscorner/detail/en/ip_22_6495

[84] T. Kamimoto, H. Yokota, and H. Kobayashi, "Effect of high pressure injection on soot formation processes in a rapid compression machine to simulate diesel flames," *SAE Technical Papers*, vol. 96, no. 1987, pp. 783–791, 1987, doi: 10.4271/871610.

[85] J. V Pastor, J. M. García-Oliver, C. Micó, and A. A. García-Carrero, "An experimental study with renewable fuels using ECN Spray A and D nozzles," *International Journal of Engine Research*, 2021, doi: 10.1177/14680874211031200.

[86] H. Bousbaa *et al.*, "Prediction and Simulation of Biodiesel Combustion in Diesel Engines: Evaluating Physicochemical Properties, Performance, and Emissions," *Fire*, vol. 7, no. 10, Oct. 2024, doi: 10.3390/fire7100364.

[87] S. Mohankumar and P. Senthilkumar, "Particulate matter formation and its control methodologies for diesel engine: A comprehensive review," 2017, *Elsevier Ltd*. doi: 10.1016/j.rser.2017.05.133.

[88] Z. A. Mansurov, "Soot formation in combustion processes (review)," Nov. 2005. doi: 10.1007/s10573-005-0083-2.

[89] H. Omidvarborna, A. Kumar, and D. S. Kim, "Variation of diesel soot characteristics by different types and blends of biodiesel in a laboratory combustion chamber," *Science of the Total Environment*, vol. 544, pp. 450–459, 2016, doi: 10.1016/j.scitotenv.2015.11.076.

[90] R. Payri, J. P. Viera, Y. Pei, and S. Som, "Experimental and numerical study of lift-off length and ignition delay of a two-component diesel surrogate," *Fuel*, vol. 158, no. December, pp. 957–967, 2015, doi: 10.1016/j.fuel.2014.11.072.

[91] Z. Wang, L. Li, J. Wang, and R. D. Reitz, "Effect of biodiesel saturation on soot formation in diesel engines," *Fuel*, vol. 175, pp. 240–248, 2016, doi: 10.1016/j.fuel.2016.02.048.

[92] M. P. B. Musculus, S. N. Laboratories, J. Dietz, and T. L. Corporation, "Effects of Diesel Fuel Combustion- Modifier Additives on In-Cylinder Soot Formation in a Heavy-Duty DI Diesel Engine," no. July, 2005.

[93] C. J. Mueller, W. J. Pitz, L. M. Pickett, G. C. Martin, D. L. Siebers, and C. K. Westbrook, "Effects of oxygenates on soot processes in di diesel engines: Experiments and numerical simulations," *SAE Technical Papers*, vol. 112, 2003, doi: 10.4271/2003-01-1791.

[94] D. Siebers and B. Higgins, "Flame lift-off on direct-injection diesel sprays under quiescent conditions," *SAE Technical Papers*, no. 724, 2001, doi: 10.4271/2001-01-0530.

[95] L. M. Pickett, D. L. Siebers, and C. A. Idicheria, "Relationship between ignition processes and the lift-off length of diesel fuel jets," *SAE Technical Papers*, no. 724, 2005, doi: 10.4271/2005-01-3843.

[96] S. Hong, M. S. Wooldridge, H. G. Im, D. N. Assanis, and H. Pitsch, "Development and application of a comprehensive soot model for 3D CFD reacting flow studies in a diesel engine," *Combust Flame*, vol. 143, no. 1–2, pp. 11–26, Oct. 2005, doi: 10.1016/j.combustflame.2005.04.007.

[97] K. M. Pang, N. Karvounis, J. H. Walther, and J. Schramm, "Numerical investigation of soot formation and oxidation processes under large two-stroke marine diesel engine-like conditions using integrated CFD-chemical kinetics," *Appl Energy*, vol. 169, pp. 874–887, May 2016, doi: 10.1016/j.apenergy.2016.02.081.

[98] X. Cheng, L. Chen, F. Yan, and S. Dong, "Study on soot formation characteristics in the diesel combustion process based on an improved detailed soot model," *Energy Convers Manag*, vol. 75, pp. 1–10, 2013, doi: 10.1016/j.enconman.2013.05.033.

[99] C. Lou, C. Chen, Y. Sun, and H. Zhou, "Review of soot measurement in hydrocarbon-air flames," *Sci China Technol Sci*, vol. 53, no. 8, pp. 2129–2141, 2010, doi: 10.1007/s11431-010-3212-4.

[100] A. E. Karataş and Ö. L. Gülder, "Soot formation in high pressure laminar diffusion flames," Dec. 2012. doi: 10.1016/j.pecs.2012.04.003.

[101] R. Balz, I. G. Nagy, G. Weisser, and D. Sedarsky, "Experimental and numerical investigation of cavitation in marine Diesel injectors," *Int J Heat Mass Transf*, vol. 169, p. 120933, 2021, doi: 10.1016/j.ijheatmasstransfer.2021.120933.

[102] C. Badock, R. Wirth, A. Fath, and A. Leipertz, "Investigation of cavitation in real size diesel injection nozzles," *Int J Heat Fluid Flow*, vol. 20, no. 5, pp. 538–544, 1999, doi: 10.1016/S0142-727X(99)00043-0.

[103] I. K. Karathanassis, J. Hwang, P. Koukouvinis, L. Pickett, and M. Gavaises, "Combined visualisation of cavitation and vortical structures in a real-size optical diesel injector," *Exp Fluids*, vol. 62, no. 1, Jan. 2021, doi: 10.1007/s00348-020-03096-1.

[104] A. Tekawade, B. A. Sforzo, K. E. Matusik, K. Fezzaa, A. L. Kastengren, and C. F. Powell, "Time-resolved 3D imaging of two-phase fluid flow inside a steel fuel injector

using synchrotron X-ray tomography," *Sci Rep*, vol. 10, no. 1, pp. 1–9, 2020, doi: 10.1038/s41598-020-65701-x.

[105] D. Guénot *et al.*, "Simultaneous laser-driven x-ray and two-photon fluorescence imaging of atomizing sprays," *Optica*, vol. 7, no. 2, p. 131, Feb. 2020, doi: 10.1364/optica.378063.

[106] T. J. Heindel, "A review of X-ray flow visualization with applications to multiphase flows," *Journal of Fluids Engineering, Transactions of the ASME*, vol. 133, no. 7, pp. 1–16, 2011, doi: 10.1115/1.4004367.

[107] D. Lazaro, S. Legoupil, G. Blokkeel, and B. Jeanne, "Metrology of steel micro-nozzles using X-ray microtomography," *Components*, no. April 2014, 2007.

[108] N. Mitroglou, M. Lorenzi, M. Santini, and M. Gavaises, "Application of X-ray micro-computed tomography on high-speed cavitating diesel fuel flows," *Exp Fluids*, vol. 57, no. 11, pp. 1–14, 2016, doi: 10.1007/s00348-016-2256-z.

[109] H. K. Suh and C. S. Lee, "Effect of cavitation in nozzle orifice on the diesel fuel atomization characteristics," *Int J Heat Fluid Flow*, vol. 29, no. 4, pp. 1001–1009, 2008, doi: 10.1016/j.ijheatfluidflow.2008.03.014.

[110] K. S. Varde, D. M. Popa, and L. K. Varde, "Spray angle and atomization in diesel sprays," *SAE Technical Papers*, vol. 93, pp. 779–787, 1984, doi: 10.4271/841055.

[111] B. Mohan, W. Yang, K. L. Tay, and W. Yu, "Experimental study of spray characteristics of biodiesel derived from waste cooking oil," *Energy Convers Manag*, vol. 88, pp. 622–632, 2014, doi: 10.1016/j.enconman.2014.09.013.

[112] Y. Wei, H. Zhang, L. Fan, B. Li, X. Leng, and Z. He, "Experimental study on influence of pressure fluctuation and cavitation characteristics of nozzle internal flow on near field spray," *Fuel*, vol. 337, Apr. 2023, doi: 10.1016/j.fuel.2022.126843.

[113] I. Ruiz-Rodriguez, R. Pos, T. Megaritis, and L. C. Ganippa, "Investigation of Spray Angle Measurement Techniques," *IEEE Access*, vol. 7, pp. 22276–22289, 2019, doi: 10.1109/ACCESS.2019.2899214.

[114] Q. Cheng, Z. Ahmad, V. Grahn, J. Hyvönen, L. Martti, and O. Kaario, "Multi-scale optical diagnostics for marine diesel spray," *Energy*, vol. 317, Feb. 2025, doi: 10.1016/j.energy.2025.134624.

[115] J. K. Bothell, T. B. Morgan, A. L. Kastengren, and T. J. Heindel, "FLUID FLOW OBSERVATIONS OF THE SPRAY NEAR-FIELD USING HIGH-SPEED X-RAY IMAGING," 2022. [Online]. Available: www.begellhouse.com

[116] R. J. H. Klein-Douwel, P. J. M. Frijters, L. M. T. Somers, W. A. de Boer, and R. S. G. Baert, "Macroscopic diesel fuel spray shadowgraphy using high speed digital imaging in a high pressure cell," *Fuel*, vol. 86, no. 12–13, pp. 1994–2007, 2007, doi: 10.1016/j.fuel.2006.11.039.

[117] M. Tang *et al.*, “Development of a Transient Spray Cone Angle Correlation for CFD Simulations at Diesel Engine Conditions,” *SAE Technical Papers*, vol. 2018-April, pp. 1–20, 2018, doi: 10.4271/2018-01-0304.

[118] Safiullah, K. Nishida, Y. Ogata, T. Oda, and K. Ohsawa, “Effects of nozzle hole size and rail pressure on diesel spray and mixture characteristics under similar injection rate profile – experimental, computational and analytical studies under non-evaporating spray condition,” *Proceedings of the Institution of Mechanical Engineers, Part D: Journal of Automobile Engineering*, pp. 1–4, 2021, doi: 10.1177/09544070211022099.

[119] S. Riess, L. Weiss, A. Peter, J. Rezaei, and M. Wensing, “Air entrainment and mixture distribution in Diesel sprays investigated by optical measurement techniques,” *International Journal of Engine Research*, vol. 19, no. 1, pp. 120–133, 2018, doi: 10.1177/1468087417742527.

[120] F. Payri, J. V. Pastor, R. Payri, and J. Manin, “Determination of the optical depth of a DI diesel spray,” *Journal of Mechanical Science and Technology*, vol. 25, no. 1, pp. 209–219, Jan. 2011, doi: 10.1007/s12206-010-1024-x.

[121] M. Linne, M. Paciaroni, T. Hall, and T. Parker, “Ballistic imaging of the near field in a diesel spray,” *Exp Fluids*, vol. 40, no. 6, pp. 836–846, 2006, doi: 10.1007/s00348-006-0122-0.

[122] D. Bauer, F. Barthel, and U. Hampel, “High-speed x-ray CT imaging of a strongly cavitating nozzle flow,” *J Phys Commun*, vol. 2, no. 7, Jul. 2018, doi: 10.1088/2399-6528/aad217.

[123] J. V. Pastor, J. M. García-Oliver, C. Micó, A. A. García-Carrero, and A. Gómez, “Experimental study of the effect of hydrotreated vegetable oil and oxymethylene ethers on main spray and combustion characteristics under engine combustion network spray A conditions,” *Applied Sciences (Switzerland)*, vol. 10, no. 16, Aug. 2020, doi: 10.3390/APP10165460.

[124] T. Buschhagen *et al.*, “Effect of aviation fuel type and fuel injection conditions on non-reacting spray characteristics of a hybrid airblast fuel injector,” in *54th AIAA Aerospace Sciences Meeting*, American Institute of Aeronautics and Astronautics Inc, AIAA, 2016. doi: 10.2514/6.2016-1154.

[125] J. C. Dearden, “Quantitative structure-property relationships for prediction of boiling point, vapor pressure, and melting point,” *Environ Toxicol Chem*, vol. 22, no. 8, pp. 1696–1709, Aug. 2003, doi: 10.1897/01-363.

[126] S. V.D. Freitas, M. B. Oliveira, A. J. Queimada, M. J. Pratas, Á. S. Lima, and J. A. P. Coutinho, “Measurement and prediction of biodiesel surface tensions,” *Energy and Fuels*, vol. 25, no. 10, pp. 4811–4817, Oct. 2011, doi: 10.1021/ef201217q.

[127] J. A. Pumphrey, J. I. Brand, and W. A. Scheller, “Vapour pressure measurements and predictions for alcohol-gasoline blends,” *Fuel*, vol. 79, no. 11, Sep. 2000, [Online]. Available: www.elsevier.com/locate/fuel

[128] B. A. Reid, G. K. Hargrave, C. P. Garner, and R. M. McDavid, “An optical comparison of the cavitation characteristics of diesel and bio-diesel blends in a true-scale nozzle geometry,” *International Journal of Engine Research*, vol. 14, no. 6, pp. 622–629, 2013, doi: 10.1177/1468087413501499.

[129] Engine Combustion Network, “Spray C Nozzle Geometry.” Accessed: Jul. 05, 2022. [Online]. Available: https://ecn.sandia.gov/diesel-spray-combustion/target-condition/spray-c-nozzle-geometry/

[130] Engine Combustion Network, “Spray D Nozzle Geometry.” Accessed: Jul. 07, 2022. [Online]. Available: https://ecn.sandia.gov/diesel-spray-combustion/target-condition/spray-d-nozzle-geometry/

[131] Nobuyuki Otsu, “A Threshold Selection Method from Gray-Level Histograms,” *IEE Transactions on Systems, Man, and Cybernetics*, vol. 9, no. 1, pp. 62–66, 1979.

[132] J. Canny, “A Computational Approach to Edge Detection,” 1986.

[133] L. M. Pickett, C. L. Genzale, and J. Manin, “Uncertainty quantification for liquid penetration of evaporating sprays at diesel-like conditions,” *Atomization and Sprays*, vol. 25, no. 5, pp. 425–452, 2015, doi: 10.1615/AtomizSpr.2015010618.

[134] F. R. Westlye, K. Penney, A. Ivarsson, L. M. Pickett, J. Manin, and S. A. Skeen, “Diffuse back-illumination setup for high temporally resolved extinction imaging,” *Appl Opt*, vol. 56, no. 17, p. 5028, 2017, doi: 10.1364/ao.56.005028.

[135] S. Skeen, K. Yasutomi, E. Cenker, B. Adamson, N. Hansen, and L. Pickett, “Standardized Optical Constants for Soot Quantification in High-Pressure Sprays,” *SAE Int J Engines*, vol. 11, no. 6, pp. 805–816, 2018, doi: 10.4271/2018-01-0233.

[136] D. L. Siebers, “Liquid-phase fuel penetration in diesel sprays,” *SAE Technical Papers*, no. 724, 1998, doi: 10.4271/980809.

[137] J. Manin, M. Bardi, and L. Pickett, “Evaluation of the liquid length via diffused back-illumination imaging in vaporizing diesel sprays,” in *The Eight International Conference on Modeling and Diagnostic for Advanced Engine Systems (COMODIA)*, 2012, pp. 665–673.

[138] Sandia National Laboratory, “Liquid Length Measurement Method.” Accessed: Jul. 04, 2023. [Online]. Available: https://ecn.sandia.gov/diesel-spray-combustion/experimental-diagnostics/liquid-penetration-length/length/

[139] L. M. Pickett and D. L. Siebers, “Soot in diesel fuel jets: Effects of ambient temperature, ambient density, and injection pressure,” *Combust Flame*, vol. 138, no. 1–2, pp. 114–135, 2004, doi: 10.1016/j.combustflame.2004.04.006.

[140] B. Higgins and D. Siebers, “Measurement of the flame lift-off location on di diesel sprays using OH chemiluminescence,” *SAE Technical Papers*, no. 724, 2001, doi: 10.4271/2001-01-0918.

[141] H. Naseri, P. Koukouvinis, I. Karathanassis, and M. Gavaises, “Flow Enhancement and Cavitation Suppression in Nozzle Flow by Viscoelastic Additives,” *Proceedings of the 10th International Symposium on Cavitation (CAV2018)*, pp. 462–467, 2019, doi: 10.1115/1.861851_ch88.

[142] A. J. Rowane, R. R. Mallepally, M. Gavaises, and M. A. McHugh, “Interfacial tension of isomers n-hexadecane and 2,2,4,4,6,8,8- heptamethylnonane with nitrogen at high pressures and temperatures,” *Ind Eng Chem Res*, vol. 59, no. 19, pp. 9293–9299, 2020, doi: 10.1021/acs.iecr.0c00213.

[143] A. J. Rowane, A. Gupta, M. Gavaises, and M. A. McHugh, “Experimental and modeling investigations of the interfacial tension of three different diesel + nitrogen mixtures at high pressures and temperatures,” *Fuel*, vol. 280, no. June, p. 118543, 2020, doi: 10.1016/j.fuel.2020.118543.

[144] S. K. Puri *et al.*, “Synergestic Deposit Control Additive Composition for Diesel Fuel and Process Thereof,” 2006/0277819 A1, 2006

[145] M. Heidari-Koochi *et al.*, “Flow visualisation in real-size optical injectors of conventional, additised, and renewable gasoline blends,” *Energy Convers Manag*, vol. 252, p. 115109, 2022, doi: 10.1016/j.enconman.2021.115109.

[146] H. Naseri, P. Koukouvinis, I. Malgarinos, and M. Gavaises, “On viscoelastic cavitating flows: A numerical study,” *Physics of Fluids*, vol. 30, no. 3, 2018, doi: 10.1063/1.5011978.

[147] R. H. Pratama, W. Huang, and S. Moon, “Unveiling needle lift dependence on near-nozzle spray dynamics of diesel injector,” *Fuel*, vol. 285, Feb. 2021, doi: 10.1016/j.fuel.2020.119088.

[148] J. Lee and C. Bae, “Application of JP-8 in a heavy duty diesel engine,” *Fuel*, vol. 90, no. 5, pp. 1762–1770, May 2011, doi: 10.1016/j.fuel.2011.01.032.

[149] J. M. Nouri, I. Vasilakos, Y. Yan, and C. C. Reyes-Aldasoro, “Effect of viscosity and speed on oil cavitation development in a single piston-ring lubricant assembly,” *Lubricants*, vol. 7, no. 10, Oct. 2019, doi: 10.3390/lubricants7100088.

[150] L. L. Wang and C. H. Lu, “The effect of viscosity on the cavitation characteristics of high speed sleeve bearing,” *Journal of Hydrodynamics*, vol. 27, no. 3, pp. 367–372, Jun. 2015, doi: 10.1016/S1001-6058(15)60494-2.

[151] N. Mitroglou, M. Gavaises, and J. Nouri, “Cavitation Inside Enlarged and Real-Size Fully Transparent Injector Nozzles and Its Effect on Near Nozzle Spray Formation,” in *Droplet Impact Phenomena and Spray Investigations Workshop*, Bergamo, 2011.

[152] M. Gavaises and A. Andriotis, “Cavitation inside multi-hole injectors for large Diesel engines and its effect on the near-nozzle spray structure,” *SAE Technical Papers*, vol. 2006, no. 724, 2006, doi: 10.4271/2006-01-1114.

[153] S. Underwood, R. Taghavi, and T. S. Miller, “Analysis of exhaust emissions of an aircraft diesel engine using jet-a,” in *AIAA Aviation 2019 Forum*, American Institute of Aeronautics and Astronautics Inc, AIAA, 2019, pp. 1–14. doi: 10.2514/6.2019-3345.

[154] E. R. Amezcua, K. Kim, C. M. Kweon, and D. A. Rothamer, “Investigation of the combustion process and modes of energy-assisted compression-ignition for low cetane number sustainable aviation fuels,” *Fuel*, vol. 393, p. 134605, Aug. 2025, doi: 10.1016/j.fuel.2025.134605.

[155] Z. Xu *et al.*, “Emission reduction characteristics of heavy-fuel aircraft piston engine fueled with 100% HEFA sustainable aviation fuel,” *Environmental Pollution*, vol. 368, Mar. 2025, doi: 10.1016/j.envpol.2025.125661.

[156] F. Kleissner and P. Hoffman, “Operation of a Compression-Ignition Kerosene Aviation Engine with Sustainable Fuel: An Experimental Study,” *SAE Technical Paper*, 2024, doi: 10.4261/2024-01-6005.

[157] A. J. Donkerbroek, M. D. Boot, C. C. M. Luijten, N. J. Dam, and J. J. ter Meulen, “Flame lift-off length and soot production of oxygenated fuels in relation with ignition delay in a DI heavy-duty diesel engine,” *Combust Flame*, vol. 158, no. 3, pp. 525–538, 2011, doi: 10.1016/j.combustflame.2010.10.003.

[158] J. D. Naber and D. L. Siebers, “Effects of gas density and vaporization on penetration and dispersion of diesel sprays,” *SAE Technical Papers*, no. 412, 1996, doi: 10.4271/960034.

[159] C. A. Idicheria and L. M. Pickett, “Ignition, soot formation, and end-of-combustion transients in diesel combustion under high-EGR conditions,” *International Journal of Engine Research*, vol. 12, no. 4, pp. 376–392, Aug. 2011, doi: 10.1177/1468087411399505.

[160] O. Baran *et al.*, “Assesment of Injector-flow characteristics of additised and renewable diesel blends through high-speed imaging,” *Fuel*, 2023.

[161] I. K. Karathanassis *et al.*, “Non-Newtonian flow of highly-viscous oils in hydraulic components,” *J Nonnewton Fluid Mech*, vol. 275, pp. 0–3, 2020, doi: 10.1016/j.jnnfm.2019.104221.

[162] B. Duboc, “The effect of fuel additives on diesel fuel delivery system and combustion performance.”

[163] T. D. Fansler, M. F. Trujillo, and E. W. Curtis, “Spray-wall interactions in direct-injection engines: An introductory overview,” *International Journal of Engine Research*, vol. 21, no. 2, pp. 241–247, Feb. 2020, doi: 10.1177/1468087419897994.

[164] W. Gu and W. Su, “Study on the Effects of Exhaust Gas Recirculation and Fuel Injection Strategy on Transient Process Performance of Diesel Engines,” *Sustainability (Switzerland)*, vol. 15, no. 16, Aug. 2023, doi: 10.3390/su151612403.

[165] R. O. Grover, T. D. Fansler, A. Lippert, M. C. Drake, and D. N. Assanis, “A numerical–experimental assessment of wall impingement models for spark-ignition direct-injection engines,” *International Journal of Engine Research*, vol. 21, no. 2, pp. 281–301, Feb. 2020, doi: 10.1177/1468087419863966.

[166] D. R. Tree and K. I. Svensson, “Soot processes in compression ignition engines,” Jun. 2007. doi: 10.1016/j.pecs.2006.03.002.

APPENDIX

A.1 Cavitation Code

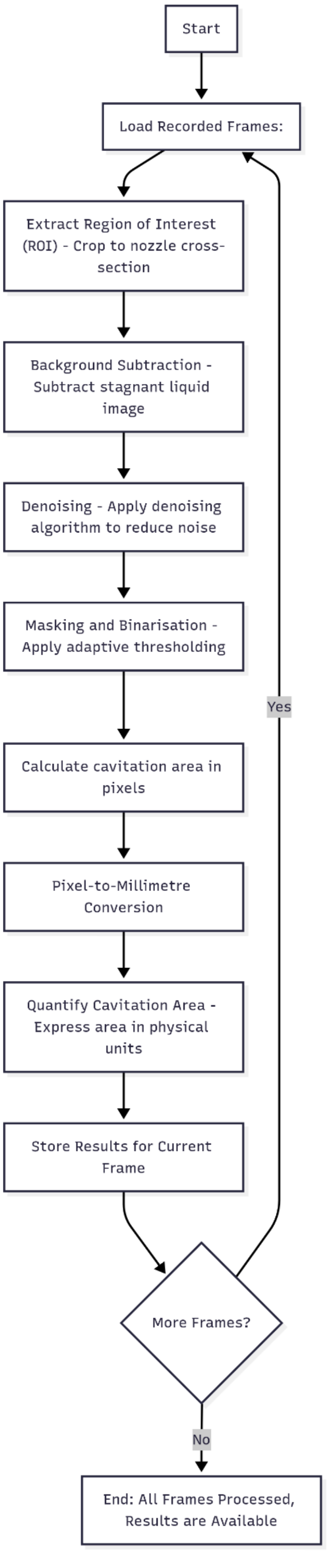

Figure A.1: Flowchart of the cavitation image analysis algorithm applied to high-speed recorded frames.

Algorithm materialising the post-processing steps as schematically depicted in Figure A.1:

```
% Cavitation Analysis for SprayD (C4 fuel) %% Start & Load Recorded Frames

clear; close all; clc;


% Directories

code_direc = '...';  % [your original paths remain unchanged]

results_direc = '...';

fuel_direc = '...';

...

frame_rate = 100000;

position = [300 200];


%% Load Mask and Background Image (Pre-processing Setup)

mask_dir = '...';

cd(mask_dir);

load C4_700_10_3.mat;

cd(fuel_direc);


% Load and process background frame (stagnant liquid image)

bckdir = dir('*backgroundframe.tif');

bck = bckdir(1).name;

bk = imread(bck);

crop_matrix = [14.5 100.5 96 268];  % ROI cropping

xmi = crop_matrix(1); ymi = crop_matrix(2); wid = crop_matrix(3); hei =
crop_matrix(4);

bk = imcrop(bk, [xmi ymi wid hei]);

bk_adjusted = imadjust(bk);

bg_avg1 = mat2gray(im2uint16(bk_adjusted));  % Background image


%% Prepare Video Output and Image List

cd(results_direc);

videoRaw = VideoWriter([condition '_Raw.avi']);
```

```
videoDiff = VideoWriter([condition '_Diff.avi']);
videoBW = VideoWriter([condition '_BW.avi']);
open(videoRaw); open(videoDiff); open(videoBW);

mkdir(['BW_images_' condition]);
cd(fuel_direc);
imglist = dir('*.tif');
imglist(end) = [];  % Remove background frame
imglist = struct2cell(imglist);
imglist(2:6,:) = [];
imglist = imglist';
cd(code_direc);
imglist = natsort(imglist);
cd(fuel_direc);

%% Initialise Storage for Results
THRMAT = zeros(length(imglist), 1);
meann = 0;
sumstdev = 0;
stf = 55;
fnf = 245;

%% Main Frame Processing Loop
for i = stf:fnf
    cd(fuel_direc);
    time = i / frame_rate;
    time_in_us = time * 1E6;
    cavity_area(i,1) = time;

    %% Extract ROI
    img1 = char(imglist(i));
    dbi_img = imread(img1);
    dbi_img = imcrop(dbi_img, [xmi ymi wid hei]);
```

```
%% Background Subtraction
dbi_img_video = mat2gray(dbi_img);
dbi_img = mat2gray(im2uint16(dbi_img));
dbi_img = dbi_img .* mask;
bg_avg1_masked = bg_avg1 .* mask;

%% Save RAW Video
timestring = [num2str(time_in_us, '%0.0f') 'us'];
raw_text = insertText(dbi_img_video, position, timestring, ...
    'FontSize', 32, 'TextColor', 'black', 'BoxOpacity', 0.0);
writeVideo(videoRaw, raw_text);

%% Image Difference + Denoising
cavity = imfuse(dbi_img, bg_avg1_masked, 'diff');
cavity = imsharpen(cavity);  % Apply basic denoising

%% Contrast Adjustment (optional before binarisation)
Low_in = min(cavity(cavity > 0), [], 'all');
High_in = max(cavity(cavity < 1), [], 'all');
if Low_in < High_in
    cavity = imadjust(cavity, [Low_in; High_in], [0 1]);
end

%% Save Difference Video Frame
cavity_text = insertText(cavity, position, timestring, ...
    'FontSize', 32, 'TextColor', 'white', 'BoxOpacity', 0.0);
writeVideo(videoDiff, cavity_text);

%% Masking and Binarisation (Adaptive Thresholding)
level2 = graythresh(cavity);  % Otsu's threshold
level = 0.25;  % Manual override
THRMAT(i,1) = level2;
```

```
    BW = imbinarize(cavity, level);
    BW = bwareaopen(BW, 20);  % Remove small artefacts

    %% Calculate Cavitation Area in Pixels
    cavity_area(i,2) = nnz(BW);

    %% Save BW Image
    cd([results_direc '/BW_images_' condition]);
    imwrite(BW, sprintf('BW_%d.tif', i));
    meann = meann + BW;

    %% Save BW Frame to Video
    BWdouble_video = insertText(mat2gray(BW), position, timestring, ...
        'FontSize', 32, 'TextColor', 'white', 'BoxOpacity', 0.0);
    writeVideo(videoBW, BWdouble_video);
end

%% Post-Processing: Compute Mean Image from All Frames
cd(fuel_direc);
mean_image = meann / ((fnf - stf) + 1);

%% Compute Standard Deviation Image (Per Pixel)
for l = stf:fnf
    cd([results_direc '/BW_images_' condition]);
    BW2 = mat2gray(im2uint16(imread(sprintf('BW_%d.tif', l))));
    sumstdev = sumstdev + (BW2 - mean_image).^2;
end
variance = sumstdev / (fnf - stf);
stdv_image = sqrt(variance);

%% Save All Resulting Data
cd([results_direc '/BW_images_' condition]);
save(sprintf('Mean_img_prob_%s.mat', condition), "mean_image");
```

```
save(sprintf('cavitation_%s.mat', condition), "cavity_area");

save(sprintf('StDev_%s.mat', condition), "stdv_image");


%% Plot Mean Cavitation Image

x = [0 crop_matrix(3)];

y = [0 crop_matrix(4)];

clims = [0 1];

figure(2); imagesc(x, y, mean_image, clims); axis tight; box off;

...

saveas(f1, sprintf('Mean_img_prob_%s.bmp', condition));


%% Plot Standard Deviation Image

figure(3); imagesc(x, y, stdv_image, clims); axis tight; box off;

...

saveas(f2, sprintf('stdev_%s.bmp', condition));


%% Close Video Files (Final Step of Processing)

close(videoRaw); close(videoDiff); close(videoBW);

%% Area vs Time Plot

figure(4);

...

plot(time_star_high, cavity_area(:,2) * scale);

...

saveas(f3, sprintf('area_time_graph.bmp', condition));


%% Visualise Mask with First Frame (Debugging / Visual Verification)

figure(5);

imshowpair(bk, BW);

...

saveas(f5, sprintf('Mask_and_Firstframe.bmp', condition));

%% Show Last BW Frame

figure(6);

imshow(BW);
```

A.2 Spray Angle Code

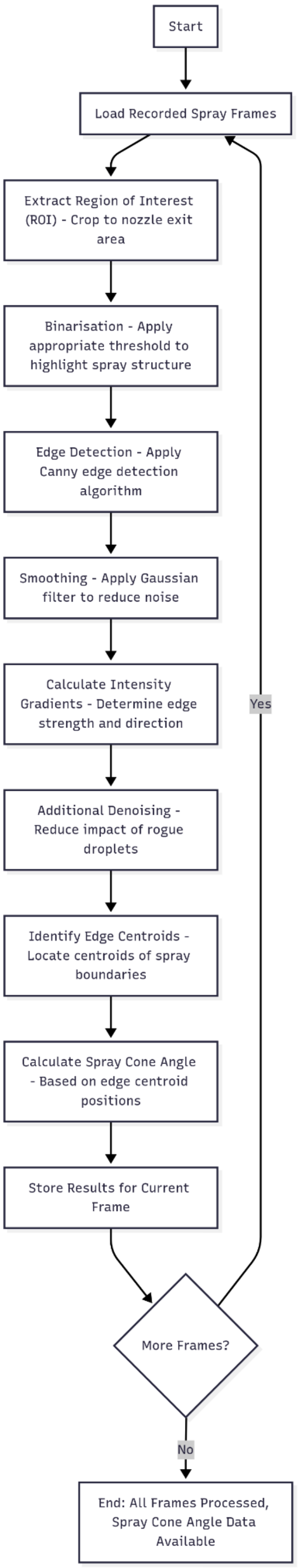

Figure A.2: Flowchart of the spray angle analysis algorithm applied to high-speed recorded frames.

Algorithm materialising the post-processing steps as schematically depicted in Figure A.2:

```
% Spray Cone Angle Analysis Script
% -------------------------------------------------------------
% This script analyses high-speed spray images to determine the spray cone angle
% using image processing steps described in the flowchart included in the thesis.

close all; clear all; clc;

% Load recorded spray frames and set experiment parameters
code_direc = '...';           % Path to processing scripts
fuel_direc = '...';           % Path to experimental image data
condition = '1250_700_1_2';
fuel = 'Bicyclohexyl';
ExperimentName = strcat(fuel, '_', condition);

frame_rate = 100000;          % Frame rate in frames per second

% Create folder for processed binary images
cd(fuel_direc);
mkdir(['BW_images_' fuel '_' condition]);

% Configure text overlay and video writers
position = [60 35; 40 200];   % Positions for overlay text
pos2 = [150 150];             % Position for timestamp

videoRaw = VideoWriter([ExperimentName '_Raw.avi']);
videoAngle = VideoWriter([ExperimentName '_Angle.avi']);
open(videoRaw); open(videoAngle);

% Load image file list
imglist = dir('*.tif');
```

```
% Define frame range
startframe = 55;
finalframe = 250;

% Initialize storage for results
Angle_full = zeros((finalframe - startframe) + 1, 3);
cone_angle = zeros((finalframe - startframe) + 1, 2);

% Main processing loop for each frame
for i = startframe:finalframe
    cd(fuel_direc);

    % Assign timestamp for current frame
    time = i / frame_rate;
    time_in_us = time * 1E6;
    timestring = [num2str(time_in_us, '%0.0f') ' us'];
    cone_angle(i,1) = time;

    % Load and normalize the image
    img = imread(imglist(i).name);
    forvideo = mat2gray(img);
    backup_img = imadjust(img);

    % Extract region of interest (ROI) around the nozzle exit
    xmin = 0; ymin = 374.5; width = 124; height = 274;
    img = imcrop(img, [xmin ymin width height]);
    img = mat2gray(img);

    % Apply Gaussian smoothing and binarization to highlight the spray
    edge_img = imgaussfilt(img, 3);              % Reduce noise
    threshold = 0.4;
    BW = imbinarize(edge_img, threshold);        % Binarize image
```

```
% Perform edge detection using the Canny algorithm
BWedge = bwareaopen(BW, 750);                % Remove small particles
BWlabel = edge(bwlabel(BWedge), 'canny');    % Edge detection

% Identify centroids of the detected spray edges
props = regionprops(BWlabel, 'Centroid', 'Orientation');
propsCell = struct2cell(props);
OrientationCell = propsCell(2,:,:);          % Store orientation data
propsCell(2,:,:) = [];
propsCell = propsCell';

% Filter centroids within the ROI boundary
for z = 1:length(propsCell)
    if propsCell{z,1}(1) < 125
        centroids(z,1) = propsCell{z,1}(1);
        centroids(z,2) = propsCell{z,1}(2);
    end
end

% Save binary-labeled image and mark centroids
cd([fuel_direc '/BW_images_' fuel '_' condition]);
f1 = figure; f1.Visible = 'Off';
imshow(BWlabel); box off;
set(gca, 'DataAspectRatio', [1 1 1], 'xdir', 'reverse');
hold on;
plot(centroids(:,1), centroids(:,2), 'r*');
saveas(f1, sprintf('spray_%d.tif', i));

% Overlay timestamp on image for video output
f1_video = mat2gray(imread(sprintf('spray_%d.tif', i)));
f1_text = insertText(f1_video, pos2, timestring, ...
    'FontSize', 20, 'TextColor', 'white', 'BoxOpacity', 0.0);
writeVideo(videoAngle, f1_text);
```

```
    % Calculate spray cone angle based on edge orientations
    allAngles = [props.Orientation];
    Angle_full(i,1) = allAngles(1);
    if numel(allAngles) > 1
        Angle_full(i,2) = allAngles(2);
    else
        Angle_full(i,2) = Angle_full(i,1);
    end

    if numel(allAngles) >= 2
        Angle = 180 - (abs(Angle_full(i,1)) + abs(Angle_full(i,2)));
    else
        Angle = 180 - (abs(Angle_full(i,1)) + abs(Angle_full(i,2)));
    end
    cone_angle(i,2) = Angle;

    % Save angle overlay to raw video output
    coneanglestring = [num2str(2 * cone_angle(i,2), '%2.1f') ' deg[°]'];
    textstr = {timestring, coneanglestring};
    for j = 1:2
        writeVideo(videoRaw, insertText(forvideo, position, textstr, ...
            'FontSize', 20, 'TextColor', 'black', 'BoxOpacity', 0.0));
    end
end

% Save angle data for post-processing and analysis
savename1 = strcat(ExperimentName, '_Angle_full');
savename2 = strcat(ExperimentName, '_cone_angle');
save(savename1, 'Angle_full');
save(savename2, 'cone_angle');

% Plot time-normalized cone angle trend
```

```
figure(10000);
hold on;
xlabel('t*'); ylabel('Cone angle [°]');
t = cone_angle(:,1);
tstar = t / t(end);
scatter(tstar(startframe:finalframe), cone_angle(startframe:finalframe,2),
'b');
plot(tstar(startframe:finalframe), cone_angle(startframe:finalframe,2),
'b');
saveas(figure(10000), sprintf('angle_%s.bmp', ExperimentName));

% Plot histogram of spray cone angle distribution
figure(9999);
histogram(cone_angle(startframe:finalframe,2));
xlabel('Spray Cone Angle (Degree)');
ylabel('Count');
title('Histogram of Spray Cone Angle');
saveas(figure(9999), sprintf('histogram_%s.bmp', ExperimentName));

% Display key statistics in console
mean_angle = mean(cone_angle(startframe:finalframe,2));
maxsca = max(cone_angle(startframe:finalframe,2));
minsca = min(cone_angle(startframe:finalframe,2));
fprintf('%s%f%s\n', 'Mean Spray Cone Angle is ', mean_angle, ' degree');
```

A.3 Multi-hole Cavitation Code

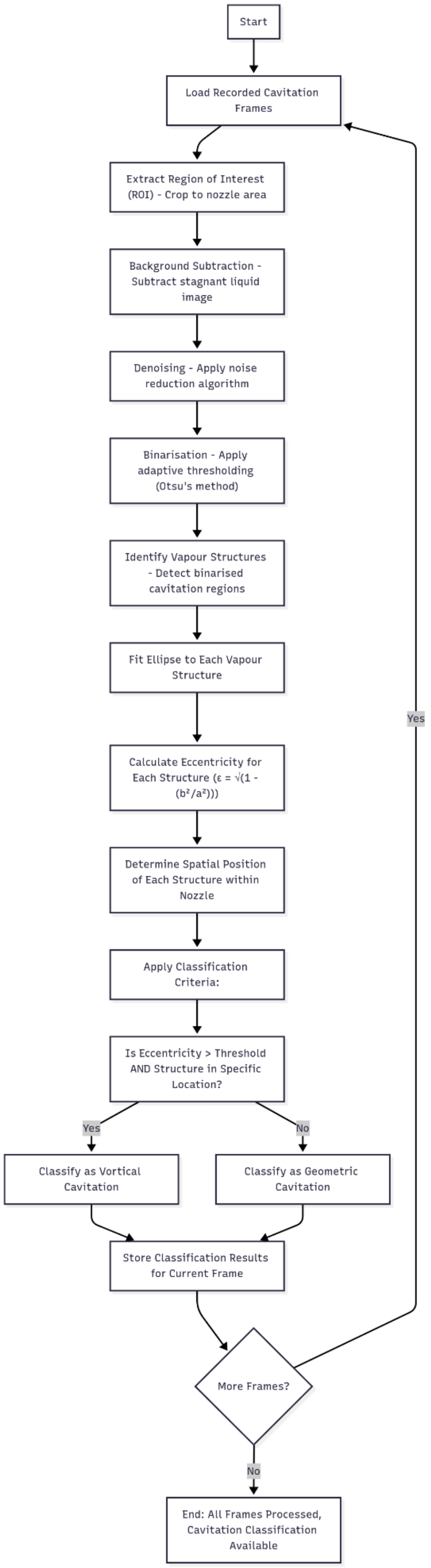

Figure A.3: Algorithmic workflow for classification of vortical and geometric cavitation in multi-hole injectors using eccentricity and spatial criteria.

Algorithm materialising the post-processing steps as schematically depicted in Figure A.3:

```
% Cavitation Area Calculation for Multihole Injector (Spray M)
%% Load and Initialising
clear; close all; clc;
fuel_direc = '[path_to_raw_images]';
results_direc = '[path_to_output_directory]';
mask_dir = '[path_to_mask_directory]';
condition = 'Base_500_1_1';

cd(mask_dir); load mask_M.mat;

cd(fuel_direc);
bck1 = imread(dir('*backgroundframe1.tif').name);
bck2 = imread(dir('*backgroundframe2.tif').name);
bk = (bck1 + bck2) / 2;
bk = imcrop(mat2gray(bk), [58.5 161.5 144 250]);

frame_rate = 100000;
Thresh = 0.30;
Thresh2 = 0.35;

%% Set Up Output and Image List

cd(results_direc);
videoRaw = VideoWriter([condition '_Raw.avi']); open(videoRaw);
videoBW = VideoWriter([condition '_BW.avi']); open(videoBW);
videoBW2 = VideoWriter([condition '_BW2.avi']); open(videoBW2);
videoMerge = VideoWriter([condition '_Merged.avi']); open(videoMerge);

mkdir(['BW_images_' condition]);
mkdir(['BW2_images_' condition]);

cd(fuel_direc);
```

```
imglist = dir('*.tif');

imglist(end-1:end) = []; % Remove background frames

imglist = natsort({imglist.name});


st = 1; ft = length(imglist) - 2;

cavity1_area = zeros(length(imglist), 3);

miyn = 0; miyn2 = 0;


%% First Pass: Geometric Cavitation Detection


for i = st:ft

    time = i / frame_rate;

    dbi_img = imread(imglist{i});

    dbi_img = mat2gray(imcrop(dbi_img, [58.5 161.5 144 250]));


    Process_Image = abs(dbi_img - bk) .* mask;

    Low_in = min(Process_Image(Process_Image > 0), [], 'all');

    High_in = max(Process_Image(Process_Image < 1), [], 'all');

    if Low_in < High_in

        Process_Image = imadjust(Process_Image, [Low_in; High_in], [0 1]);

    end


    BW = bwareaopen(imbinarize(Process_Image .* mask, Thresh), 20, 4);

    cavity1_area(i,1) = time;

    cavity1_area(i,2) = nnz(BW);


    imwrite(BW, sprintf('%s/BW_images_%s/BW_%d.tif', results_direc,
condition, i));

    writeVideo(videoBW, insertText(mat2gray(BW), [2 2], ...

        [num2str(time * 1e6) 'us'], 'FontSize', 20, 'TextColor', 'white',
'BoxOpacity', 0.0));

    writeVideo(videoRaw, insertText(dbi_img, [2 2], ...

        [num2str(time * 1e6) 'us'], 'FontSize', 28, 'TextColor', 'white',
'BoxOpacity', 0.0));
```

```
    miyn = miyn + BW;
end

%% Second Pass: String (Vortical) Cavitation Detection

for z = st:ft
    time = z / frame_rate;
    dbi_img = imread(imglist{z});
    dbi_img = mat2gray(imcrop(dbi_img, [58.5 161.5 144 250]));

    Process_Image2 = abs(dbi_img - bk) .* mask;
    Low_in = min(Process_Image2(Process_Image2 > 0), [], 'all');
    High_in = max(Process_Image2(Process_Image2 < 1), [], 'all');
    if Low_in < High_in
        Process_Image2 = imadjust(Process_Image2, [Low_in; High_in], [0
1]);
    end

    BW2 = bwareaopen(imbinarize(Process_Image2 .* mask, Thresh2), 20, 4);
    cavity1_area(z,2) = nnz(BW2);

    imwrite(BW2, sprintf('%s/BW2_images_%s/BW2_%d.tif', results_direc,
condition, z));
    writeVideo(videoBW2, insertText(mat2gray(BW2), [2 2], ...
        [num2str(time * 1e6) 'us'], 'FontSize', 20, 'TextColor', 'white',
'BoxOpacity', 0.0));

    rp = regionprops(BW2, 'Eccentricity');
    if isempty(rp)
        cavity1_area(z,3) = 0;
    else
        cavity1_area(z,3) = rp.Eccentricity;
    end
```

```
    writeVideo(videoMerge, imshowpair(dbi_img, mat2gray(BW2),
'montage').CData);

    miyn2 = miyn2 + BW2;
end

%% Statistical Analysis and Saving Results

close(videoRaw); close(videoBW); close(videoBW2); close(videoMerge);
mean_image2 = miyn2 / ((ft - st) + 1);

sumstdev2 = 0;
for l = st:ft
    BW2 = mat2gray(imread(sprintf('%s/BW2_images_%s/BW2_%d.tif', ...
        results_direc, condition, l)));
    sumstdev2 = sumstdev2 + (BW2 - mean_image2).^2;
end
stdv_image2 = sqrt(sumstdev2 / ((ft - st) - 1));

save(['Mean_img_prob_' condition '.mat'], "mean_image2");
save(['cavitation_' condition '.mat'], "cavity1_area");
save(['StDev_' condition '.mat'], "stdv_image2");

%% Cavitation Classification Based on Eccentricity and Position

clear all; clc;
cd('[path_to_final_mat_files]');
load('X.mat');
for i = 1:length(A5)
    if A5{i,1} == 0
        A5(i,:) = {0};
    else
```

```
        for j = 1:length(A5{i,2})

            EC(i,j) = A5{i,2}(j).Eccentricity;

            CEY(i,j) = A5{i,4}(j).Centroid(2);

            AR(i,j) = A5{i,6}(j).Area;


            if CEY(i,j) < 195 || (CEY(i,j) >= 195 && EC(i,j) > 0.99)

                SC(i,j) = AR(i,j);

                StringCavarea(i,1) = sum(SC(i,:));

            else

                SC(i,j) = 0;

                StringCavarea(i,1) = 0;

            end

        end

    end

end


%% Grouping by Eccentricity Bands and Validation


for k = 1:length(AR)

    for l = 1:width(AR)

        if EC(k,l) > 0.98

            Group1(k,l) = AR(k,l);

        elseif EC(k,l) > 0.90

            Group2(k,l) = AR(k,l);

        elseif EC(k,l) > 0.80

            Group3(k,l) = AR(k,l);

        else

            Group4(k,l) = AR(k,l);

        end

    end

end


CC = sum(Group1(:)) + sum(Group2(:)) + sum(Group3(:)) + sum(Group4(:));
```

```
DD = sum(cell2mat(A5(:,1)));

if CC == DD

    fprintf('Sum Check is OK\n');

end

fprintf('Group1 pixel area: %5f\n', sum(Group1(:)));

fprintf('Group2 pixel area: %5f\n', sum(Group2(:)));

fprintf('Group3 pixel area: %5f\n', sum(Group3(:)));

fprintf('Group4 pixel area: %5f\n', sum(Group4(:)));

fprintf('Total String Cavitation Area: %5f\n', sum(StringCavarea));
```

A.4 Soot Quantification

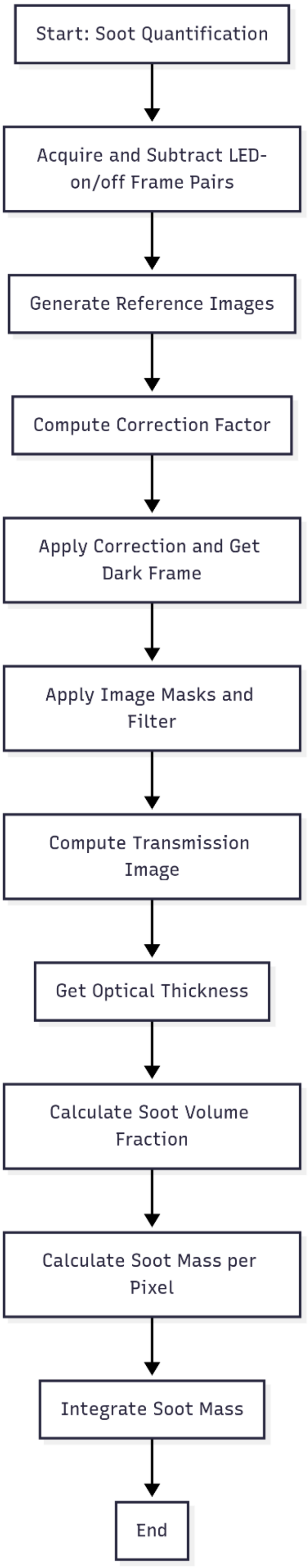

Figure A.4: Soot quantification post-processing workflow.